Calhoun: The NPS Institutional Archive

DSpace Repository

Theses and Dissertations | Thesis and Dissertation Collection

1994-06

Magnetic field generation in shock waves

Carter, John P.

Monterey, California. Naval Postgraduate School

http://hdl.handle.net/10945/30551

Downloaded from NPS Archive: Calhoun

Calhoun is a project of the Dudley Knox Library at NPS, furthering the precepts and goals of open government and government transparency. All information contained herein has been approved for release by the NPS Public Affairs Officer.

Dudley Knox Library / Naval Postgraduate School
411 Dyer Road / 1 University Circle
Monterey, California USA 93943

http://www.nps.edu/library

NAVAL POSTGRADUATE SCHOOL
Monterey, California

THESIS

MAGNETIC FIELD GENERATION IN SHOCK WAVES

by

LT John P. Carter

June 1994

Thesis Advisor: F.R. Schwirzke

Approved for public release; distribution is unlimited.

THESIS
C273726

REPORT DOCUMENTATION PAGE

Form Approved OMB No. 0704

Public reporting burden for this collection of information is estimated to average 1 hour per response, including the time for reviewing instruction, searching existing data sources, gathering and maintaining the data needed, and completing and reviewing the collection of information. Send comments regarding this burden estimate or any other aspect of this collection of information, including suggestions for reducing this burden, to Washington Headquarters Services, Directorate for Information Operations and Reports, 1215 Jefferson Davis Highway, Suite 1204, Arlington, VA 22202-4302, and to the Office of Management and Budget, Paperwork Reduction Project (0704-0188) Washington DC 20503.

1. AGENCY USE ONLY *(Leave blank)*	2. REPORT DATE JUNE 1994	3. REPORT TYPE AND DATES COVERED Master's Thesis

4. TITLE AND SUBTITLE MAGNETIC FIELD GENERATION IN SHOCK WAVES	5. FUNDING NUMBERS
6. AUTHOR(S) Carter, John, P.	
7. PERFORMING ORGANIZATION NAME(S) AND ADDRESS(ES) Naval Postgraduate School Monterey CA 93943-5000	8. PERFORMING ORGANIZATION REPORT NUMBER
9. SPONSORING/MONITORING AGENCY NAME(S) AND ADDRESS(ES)	10. SPONSORING/MONITORING AGENCY REPORT NUMBER

11. SUPPLEMENTARY NOTES The views expressed in this thesis are those of the author and do not reflect the official policy or position of the Department of Defense or the U.S. Government.

12a. DISTRIBUTION/AVAILABILITY STATEMENT Approved for public release; distribution is unlimited.	12b. DISTRIBUTION CODE *A

13. ABSTRACT *(maximum 200 words)*

Laser produced plasma jets interacting with a background plasma have been used to study magnetic field generation in shock waves. Shock heating produces axial electron temperature and density gradients which are perpendicular to the radial temperature and density gradients. Electron heat transport and ion diffusion, in the radial direction, occur at different rates. This combination of non-parallel temperature and density gradients generate a magnetic field in the azimuthal direction. Simulations corroborate the experimental observation that magnetic fields are generated when a supersonic plasma jet interacts with a background plasma. Magnetic flux generated by this mechanism requires no initial field, which is in contrast to the dynamo mechanism which does require an initial seed field. Specific applications analyzed in this thesis include interplanetary shocks and nuclear EMP effects in the MHD domain. It may be assumed that shock generated magnetic fields are also of importance under astrophysical conditions.

14. SUBJECT TERMS *Magnetic Field Generation; Shocks; Plasma Jets; Interplanetary Shocks; Non-parallel temperature and density gradients; Simulations; Nuclear Electromagnetic Pulse	15. NUMBER OF PAGES * 121 16. PRICE CODE

17. SECURITY CLASSIFICATION OF REPORT Unclassified	18. SECURITY CLASSIFICATION OF THIS PAGE Unclassified	19. SECURITY CLASSIFICATION OF ABSTRACT Unclassified	20. LIMITATION OF ABSTRACT UL

NSN 7540-01-280-5500

Standard Form 298 (Rev. 2-89)

Prescribed by ANSI Std. 239-18

Approved for public release: distribution is unlimited.

Magnetic Field Generation in Shock Waves

by

John P. Carter
Lieutenant, United States Navy
B. S., Carnegie Mellon University, 1986

Submitted in partial fulfillment of the
requirements for the degree of

MASTER OF SCIENCE IN PHYSICS
from the
NAVAL POSTGRADUATE SCHOOL
June 1994

Author: [redacted]
John P. Carter

Approved by: [redacted]
Fred R. Schwirzke, Thesis Advisor

[redacted]
Alfred W. Cooper, Second Reader

[redacted]
William B. Colson, Chairman,
Department of Physics

ABSTRACT

Laser produced plasma jets interacting with a background plasma have been used to study magnetic field generation in shock waves. Shock heating provides axial electron temperature and density gradients which are perpendicular to the radial temperature and density gradients. Electron heat transport and ion diffusion, in the radial direction, occur at different rates. This combination of non-parallel temperature and density gradients generates a magnetic field in the azimuthal direction. Simulations corroborate the experimental observation that magnetic fields are generated when a supersonic plasma jet interacts with a background plasma. Magnetic flux generated by this mechanism requires no initial field, which is in contrast to the dynamo mechanism which requires an initial seed field. Specific applications analyzed in this thesis include interplanetary shocks and nuclear EMP effects in the MHD domain. It may be assumed that shock generated magnetic fields are also of importance under astrophysical conditions.

Thesis
C273726
c.2

Table of Contents

I. INTRODUCTION 1

A. THESIS STATEMENT 5

II. THEORY 6

A. SELF-GENERATED MAGNETIC FIELDS 6

B. SHOCK-GENERATED MAGNETIC FIELDS 9

C. SHOCK THEORY 12

D. ELECTRON HEAT TRANSPORT 18

E. ION DIFFUSION 29

III. PREVIOUS EXPERIMENTAL WORK 31

A. INTRODUCTION 31

B. MCKEE'S "SHELL" MODEL 32

C. BIRD'S WORK 34

D. BROOKS' WORK 37

E. BARRIER SHOCK 38

IV. NUMERICAL SIMULATIONS 42

A. PL2.C 42

B. DENSITY / TEMPERATURE PROFILES 44

C. FINITE DIFFERENCE EQUATIONS 51

D. PL7.C 58

V. SIMULATION RESULTS 60

A. INTRODUCTION 60

DUDLEY KNOX LIBRARY
NAVAL POSTGRADUATE SCHOOL
MONTEREY CA 93943-5101

B. δ_{rT} / δ_{rn} BEHAVIOR 62

C. T_e max BEHAVIOR 66

D. TEMPORAL BEHAVIOR 69

E. FIELD GEOMETRIES 73

F. ELECTRON PRE-HEATING (δ_{zT}/δ_{zn}) 81

VI. APPLICATIONS 85

A. INTERPLANETARY SHOCKS 85

B. NUCLEAR EMP EFFECTS IN THE MHD DOMAIN 89

VII. CONCLUSION 101

APPENDIX 105

A. PL2.C 105

B. PL7.C 108

REFERENCES 112

INITIAL DISTRIBUTION LIST 114

ACKNOWLEDGEMENT

The author is indebted to the many insightful discussions with Dr. Fred Schwirzke during the preparation of this thesis. The author is also grateful to Dr. Colson and Joe Blau for their availability to answer any programming or computer specific questions, to Dr. Olsen for his notes on interplanetary shocks, and to Dr. Maruyama for his reference material on nuclear EMP phenomena.

Most of all, the author is forever grateful to his supportive and patient wife, Cheryl, for her proofreading skills and to his two beautiful daughters, Jessica and Emily, for making the universe a more wonderful place.

I. INTRODUCTION

Since the early 1960's, extensive research has been done on laser produced plasmas. The motivation for this stemmed from the fact that laser produced plasmas provide an efficient and cost effective way of studying collisional plasma phenomena. Fusion research has drawn greatly from the knowledge obtained from laser plasma research. Inertial and magnetic confinement fusion techniques are prime examples of this. Particularly in the field of inertial confinement fusion, a thorough understanding of how intense coherent laser light interacts with the surface of a deuterium pellet is critical in achieving the enormous temperatures and densities required to obtain an appreciable fusion yield. Laser plasma surface interactions have been extensively studied at the Naval Postgraduate School.

High density plasma jets are produced when the incident laser radiation strikes an aluminum target. When the laser light initially hits the target, electrons within the aluminum absorb the incident radiation. Since the collision frequency of electrons in the target is on the order of 10^{13} sec^{-1}, within the laser pulse length of 22 nanoseconds, the electrons have more than ample time to distribute their energy to other electrons as well as lattice phonons, hence allowing the optical laser energy to be converted to thermal energy. The highly ionized target material forms a dense plasma jet which expands in the direction that is normal to the target surface. During heating and ionization of target material, radial temperature gradients associated with the laser radiation and axial density gradients, which are associated with the expanding dense target material, generate magnetic fields which have the structure shown in Figure 1. If the plasma jet is viewed head on, the laser produced magnetic field direction is

clockwise. These fields decay relatively slowly when compared to the time scale of jet expansion into the background plasma. Jet expansion occurs in ≤ 1 μsec over a distance of 3 cm. During this expansion the magnetic fields are "frozen in" the expanding plasma jet. The magnetic fields have azimuthal symmetry with respect to the axis of the jet. In this geometry the magnetic field lines closely represent concentric rings around the axis of the expanding plasma jet.

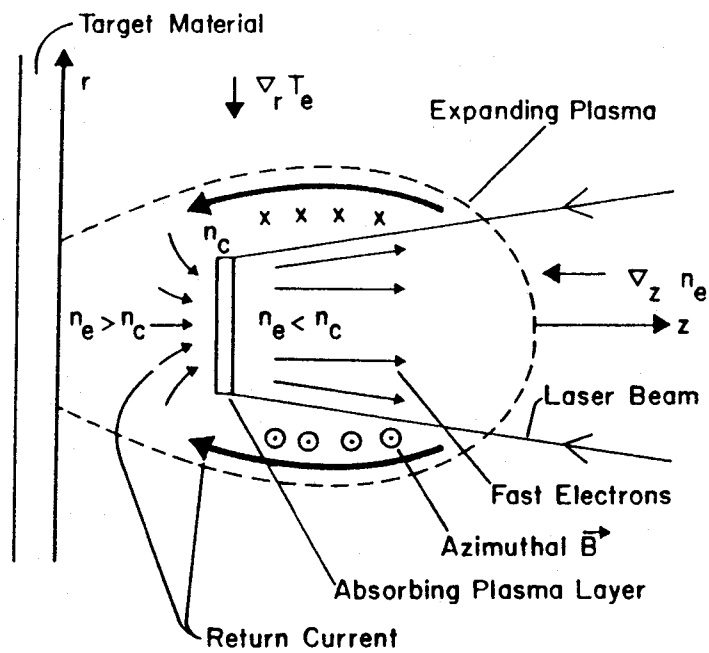

Figure 1: Geometry of Laser Produced Plasma Jet and Associated Magnetic Field.

The fields and the motion of ions, in direction normal to the target surface, tend to prevent expansion in the radial direction; hence the ionized target material closely represents a plasma jet expanding outward at approximately 10^5 m/sec. Comparison of this velocity with that of the ion acoustic velocity of the background plasma immediately indicates that the

jet is supersonic. Calculations will be shown in this thesis.

Once the laser pulse has ceased, additional magnetic fields are generated by nonparallel temperature and density gradients created by a shock transition at the leading edge of the jet. If the background plasma density is sufficiently high, a shock front is created at the leading edge of the plasma jet which causes a discontinuity in the electron and ion temperatures in accordance with classical shock theory. Moreover, since the jet is highly supersonic, temperature is increased by an order of magnitude higher than density. This is because at higher densities the plasma (as with any gas) tends to become more difficult to compress (see Figure 2). These shock-generated magnetic fields have the geometry as shown in Figure 3. Notice that the field direction is counterclockwise when viewed head on.

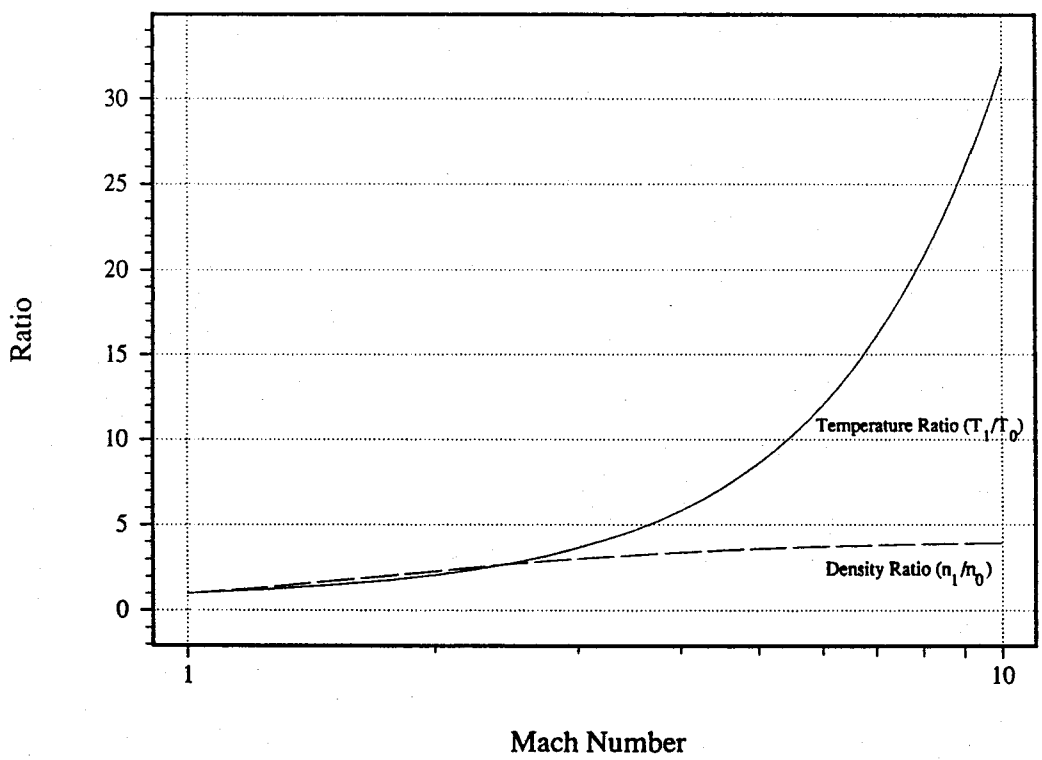

Figure 2: Temperature and Pressure Characteristics Versus Mach Number assuming no ionization losses.

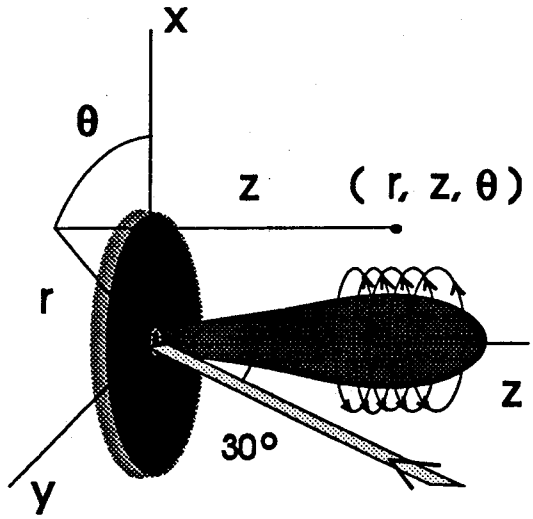

Figure 3: Geometry of Shock Produced Magnetic Fields.

Once the plasma has been shock heated, the hot magnetized electrons (due to their small Larmor radius) rapidly disperse their thermal energy through electron-electron collisions. The ions have a relatively large Larmor radius and mean free path ($\lambda_i \gg \delta_{rn}$, $r_{L,i} \gg \delta_{rn}$, δ_{rn} is the characteristic radial size of the jet). The hot ions, therefore, expand out radially at their respective thermal (sound) velocity. Diffusion of electron thermal energy via electron-electron interactions (while in their gyromagnetic orbits) occurs faster than the radial expansion of the ions. Therefore, at later times the radial electron temperature gradient has a characteristic width (half width at half maximum) which is greater than the radial electron density gradient. The electron density gradients both in the axial and radial directions are inherently dictated by the ion density. Hence the radial electron density gradient can not relax as fast as the radial electron temperature gradient.

That is, the radial electron density distribution in the laser plasma does not change as rapidly as the electron temperature. Electrons colliding with other electrons while undergoing gyromagnetic motion in the laser generated magnetic field, can transmit energy much more quickly than ions can provide particle transport. This is mentioned here as point of fact, calculations will however be shown later in this thesis.

The study of these dense plasma jets and their surrounding magnetic fields is important not only in perfecting inertial confinement fusion, but also in understanding the magnetic field structure of plasma jets which are directly related to phenomena such as: electromagnetic pulse effects associated with nuclear detonations, magnetic fields associated with the earth's bow shock, matter jets associated with some galaxies and quasars, and other occasions where plasma jets exist in astrophysical phenomena. Chapter VI of this thesis will provide some additional study in plasma jet related phenomena.

A. THESIS STATEMENT

Shock heating at the front of a plasma jet creates temperature and density gradients which generate unique magnetic fields. They are unique in that their direction is reversed when compared to the self-generated magnetic fields which are associated with laser-surface interactions. Numerical simulations have been used to show that shock heating, combined with fast thermal transport in the radial direction, generates the experimentally observed shock magnetic fields. Analytical work with applications to interplanetary shocks and nuclear EMP in the MHD domain is also presented.

II. THEORY

A. SELF-GENERATED MAGNETIC FIELDS

The magnetic fields previously discussed are inherently self-generated. That is, they require no initial seed magnetic field. For example, the terrestrial magnetic field exists today due to a process called "the dynamo mechanism". This mechanism requires an initial seed magnetic field. Nonuniform rotations within the earth's molten core (driven by irregular convection of conducting fluid) greatly slow the decay of the initially present magnetic fields, while continuing to generate additional magnetic field flux by $\vec{v}\times\vec{B}$ induced currents. The theory of magnetic field generation, which will be described here, is strikingly different in this respect. The important point about the theory presented here, is that a source term exists in the magnetic field generation equation which allows spontaneous growth of magnetic flux in a plasma.

In order to generate a magnetic field it is immediately apparent that there must exist an electric field which satisfies Maxwell's equation:

$$\frac{\partial \vec{B}}{\partial t} = -\nabla \times \vec{E} \,. \tag{1}$$

Generalized Ohm's law provides an equation of motion for the electrons which respond to the influence of an electric field. Generalized Ohm's law is given by:

$$\rho_e \left[\frac{\partial \vec{v}_e}{\partial t} + (\vec{v}_e \cdot \nabla) \vec{v}_e \right] = - e n_e (\vec{E} + \vec{v}_e \times \vec{B}) - \nabla P_e + \frac{n_e e}{\sigma} \vec{j} \,. \tag{2}$$

The subscript e denotes electron parameters. ρ_e indicates mass density, j

indicates current density, σ indicates electrical conductivity, and $\vec{v}$ indicates fluid velocity. The electron plasma frequency:

$$\omega_p = \left[\frac{n_e e^2}{\varepsilon_o m}\right]^{1/2}$$

or $\nu_p = 8.99\, n_e^{1/2}$ where ν_p is given in $\sec^{-1}$ and n_e is in m^{-3}, is about $1.1\times10^{14}\ \sec^{-1}$. Therefore, it is justifiable to neglect the inertial and convective terms on the left hand side of equation (2). Thus equation (2) becomes,

$$\vec{E} = \frac{1}{\sigma}\vec{j} - (\vec{v}_e \times \vec{B}) - \frac{1}{n_e e}\nabla P_e\ . \tag{3}$$

Taking the curl of equation (3) and using Maxwell's equation given in equation (1) gives,

$$\frac{\partial \vec{B}}{\partial t} = -\frac{1}{\sigma}\nabla\times\vec{j} + \nabla\times(\vec{v}_e \times \vec{B}) + \nabla\times\frac{1}{n_e e}\nabla P_e\ . \tag{4}$$

Now by using,

$$\mu_o\vec{j} = \nabla\times\vec{B} \quad \text{and} \quad \nabla\cdot\vec{B} = 0 \tag{5}$$

the first term on the right hand side of equation (4) becomes,

$$-\frac{1}{\sigma}\nabla\times\vec{j} = \frac{1}{\mu_o\sigma}\nabla^2\vec{B}\ . \tag{6}$$

The equation of state, assuming an ideal gas, $P_e = n_e k T_e$ gives,

$$\nabla\times\frac{1}{n_e e}\nabla P_e = \nabla\times\frac{1}{n_e e}\nabla(n_e k T_e) = \nabla\times\left[\frac{k}{e}\nabla T_e + \frac{kT_e}{n_e e}\nabla n_e\right]. \tag{7}$$

Since $\nabla\times\nabla T_e = 0$, equation (7) may be rewritten as,

$$\nabla\times\frac{1}{n_e e}\nabla P_e = \nabla\times\left[\frac{kT_e}{n_e e}\nabla n_e\right]. \tag{8}$$

Now using the vector identity,

$$\nabla\times(\phi\vec{A}) = \phi\nabla\times\vec{A} + \nabla\phi\times\vec{A},$$

with the scalar function $\phi = kT_e/n_e e$, the vector $\vec{A} = \nabla n_e$, and $\nabla \times \nabla n_e = 0$, the right hand side of equation (8) becomes,

$$\nabla \times \left[\frac{kT_e}{en_e} \nabla n_e \right] = \frac{k}{e} \nabla T_e \times \frac{1}{n_e} \nabla n_e. \tag{9}$$

Finally equation (4) becomes,

$$\frac{\partial \vec{B}}{\partial t} = \frac{1}{\mu_o \sigma} \nabla^2 \vec{B} + \nabla \times (\vec{v}_e \times \vec{B}) + \frac{k}{e} \nabla T_e \times \frac{1}{n_e} \nabla n_e. \tag{10}$$

The first term on the right side of equation (10) represents diffusion of the magnetic field through the plasma. The rate of field diffusion or field decay in the plasma will be determined by the electrical conductivity, or Spitzer resistivity, of the plasma. Based on dimensional analysis it is obvious that the characteristic time required for magnetic field decay is, $\tau_m = \mu_o \sigma l^2$ (l represents the characteristic size of the magnetic field region). If Ohmic heating losses are negligible, then the current (i.e. the magnetic field) will not decay, and the diffusion term can be neglected. The second term represents the convective element of changes of $\vec{B}$ within the plasma. Equation (10) without the third term is the called "the dynamo equation" which when coupled with the equations which describe the convective behavior ($\vec{v}$) of fluids within a rotating body, can be solved (often numerically) to provide an idea of how dipoles and higher multipoles are generated within the earth and other celestial bodies. The ratio of the convection term to the diffusion term is often called the magnetic Reynolds number, given by,

$$R = \mu_o \sigma v l \approx \frac{\tau v}{l},$$

where l is the characteristic size of the field or convective cell. For experiments analyzed in this thesis, the magnetic Reynolds number is large, implying that the field is "frozen" in the plasma.

The third term represents a source term which allows for spontaneous magnetic field generation when non-parallel temperature and density gradients are present. It is this term which allows for the growth of a magnetic field in the absence of an initial seed field. The initial laser induced self-generated magnetic fields are produced in this way. Laser irradiation of the target surface rapidly raises the material temperature at the surface. A radial temperature gradient is established due to the energy density cross section of the laser beam. The expanding, ionized target material forms a dominant axial density gradient, which propagates at the jet velocity away from the target surface. The dominant radial temperature and axial density gradients generate the initially observed magnetic fields as shown in Figure 1. Subsequent expansion of the jet at substantial background pressures allows shock formation to occur, which itself is a mechanism which generates temperature and density gradients, and allows for magnetic field production. Shock formation provides heating and compression behind the shock front.

B. SHOCK-GENERATED MAGNETIC FIELDS

In the case of shock generated fields, differences in the radial temperature and density gradients exist because the radial electron density gradients are maintained by the relatively slower moving ions. This must be true in order to maintain quasineutrality of the plasma. Electrons maintain a force balance between the attractive coulomb interaction with the ions and the pressure gradient force. Equilibrium between these two opponents ensures that quasineutrality on scales larger than a Debye length is obeyed. The Debye length is given by,

$$\lambda_D = \left[\frac{\varepsilon_0 k T_e}{n_e e^2}\right]^{1/2}$$

or,

$$\lambda_D = 740 \left[\frac{T_e}{n_e}\right]^{1/2},$$

where T_e is in eV, n_e is in cm^{-3}, and λ_D is in cm. For the plasmas considered here $n_e \approx 10^{14}$ cm^{-3}, $kT_e \approx 42$ eV, and hence $\lambda_D \approx 4.8\times10^{-4}$ cm. This is much smaller than the dimensions of the plasma jet. Therefore, charge neutrality on scales of the jet size are maintained.

While the electron density gradients are largely dictated by the slower ions, electron temperature gradients are not only dictated by electron diffusion but also by the heat conductivity of the magnetized electrons. Conduction of heat by the electrons in and around the plasma jet occurs relatively quickly compared to the ion motion.

Two distinct cases exist when studying plasma jets. First, the plasma jet may simply propagate into a vacuum. In this case, free expansion occurs and from the onset of plasma production the relevant gradients monotonically decay, hence field generation due to non-parallel gradients is limited and quickly becomes negligible. Second, if the plasma jet expands into a relatively dense background plasma, interaction with the background plasma produces higher laser produced and shock generated magnetic field strengths at the front of the plasma jet. Shock generated magnetic fields are identified experimentally by reversal of the azimuthal field component at the jet front (see Figure 4).

Larger magnetic fields might be expected since an ionized background provides a highly conductive medium so that larger currents are produced by the existing gradients. Shock generated fields occur when the jet interacts with the background. As the plasma jet propagates into the background plasma at a velocity greater than the local ion acoustic velocity,

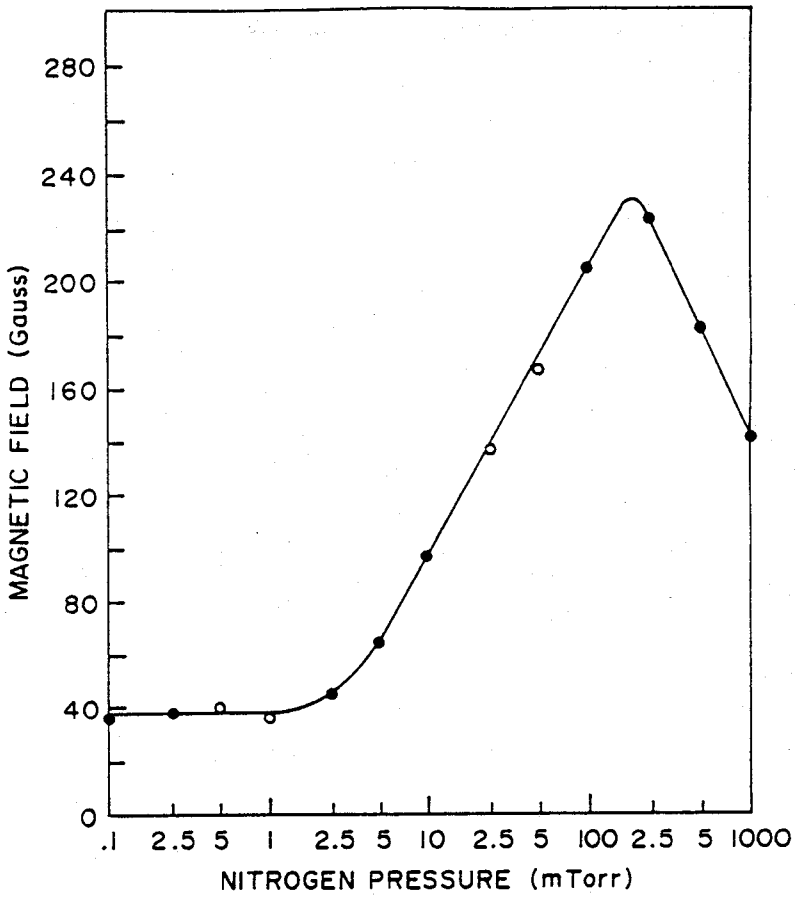

Figure 4: Magnetic Field Strength Versus Background Plasma Pressure. Maximum azimuthal magnetic field at z=0.4 cm, r=0.3 cm, $\theta=0^o$, as a function of N_2 background pressure for an incident laser power of 300 MW. [Ref. 1]

a supersonic shock front is created at the leading edge of the jet. The shock front is a thin (thickness ≈ 3 mm), nearly discontinuous, transition in plasma properties.

C. SHOCK THEORY

The ion acoustic speed in a plasma is easily derived by linearizing the ion equation of motion and continuity equation. These are given by,

$$\rho\left[\frac{\partial \vec{v}}{\partial t} + (\vec{v}\cdot\nabla)\vec{v}\right] = -\nabla P \tag{11}$$

and

$$\frac{\partial \rho}{\partial t} + \nabla\cdot(\rho\vec{v}) = 0\,, \tag{12}$$

respectively. In order to linearize these equations, consider a uniform fluid with density ρ_o, pressure P_o, and velocity $\vec{v}_o$ with small perturbations ρ_1, P_1, and $\vec{v}_1$, so that $\rho_o + \rho_1$, $P_o + P_1$, and $\vec{v}_o + \vec{v}_1$, describe the full dynamic behavior. Using $\rho = \rho_o + \rho_1$, $P = P_0 + P_1$, and $\vec{v} = \vec{v}_o + \vec{v}_1$ in the above equations and taking $\nabla\rho_o = \nabla P_o = \nabla\cdot\vec{v}_0 = 0$ gives,

$$(\rho_0 + \rho_1)\frac{\partial \vec{v}_1}{\partial t} + (\rho_0 + \rho_1)(\vec{v}_1\cdot\nabla)\vec{v}_1 = -\nabla P_1$$

and

$$\frac{\partial \rho_1}{\partial t} + \vec{v}_1\cdot\nabla\rho_1 + (\rho_0 + \rho_1)\nabla\cdot\vec{v}_1 = 0.$$

Neglecting second order approximations, i.e. terms such as $\rho_1\vec{v}_1$, provides the linearized, first order approximations to the dynamical equations:

$$\rho_o\frac{\partial \vec{v}_1}{\partial t} = -\nabla P_1 = -\left[\frac{\partial P}{\partial \rho}\right]_s \nabla\rho_1 \quad \text{and} \quad \frac{\partial \rho_1}{\partial t} + \rho_o\nabla\cdot\vec{v}_1 = 0.$$

Taking the divergence of the first equation and subtracting it from the time derivative of the second equation gives,

$$\frac{\partial^2 \rho_1}{\partial t^2} = \left[\frac{\partial P}{\partial \rho}\right]_s \nabla^2\rho_1. \tag{13}$$

Equation (11) clearly represents the wave equation for ρ_1, hence the ion

acoustic sound speed is given by,

$$c_s^2 = \left[\frac{\partial P}{\partial \rho}\right]_s .$$

The subscript s indicates the partial derivative is taken at constant entropy, and hence represents the adiabatic ion sound speed for small disturbances. The important concept to take from this presentation is that if the disturbances are no longer small, then second order perturbations can no longer be neglected. Linear analysis (as given above) is no longer valid, because the nonlinear terms such as $\rho_1 \nabla \cdot \vec{v}_1$ can not be neglected. Hence, shock wave formation is inherently a nonlinear process.

Without exactly solving the nonlinear fluid equations, important characteristics concerning shock fronts can still be derived. Shock fronts in fluids constitute near discontinuities in T, ρ, and P. When viewed from the shock front frame of reference the conditions which relate parameters such as ρ, P, T across the shock front can be more easily understood. In this frame, the shock front is stationary and the unshocked fluid (denoted by region 1) is moving at velocity v_1 while the shocked fluid (denoted by region 2) is moving at velocity v_2. Therefore, unshocked and shocked quantities will be denoted with subscripts of 1 and 2, respectively. Figure 5 shows this arrangement.

Three quantities must be conserved when passing through the shock front: (1) mass flux, (2) momentum flux, and (3) energy flux. This assumes that the shock triggers no local energy release (such as by ionization). As it turns out, this assumption is not valid for the strong shocks considered in this thesis. The presence of ionizations will be discussed in subsequent sections in order to explain discrepancies between observed and simulated magnetic field magnitudes. First, mass conservation across the shock front follows directly from the continuity equation. If the continuity equation is

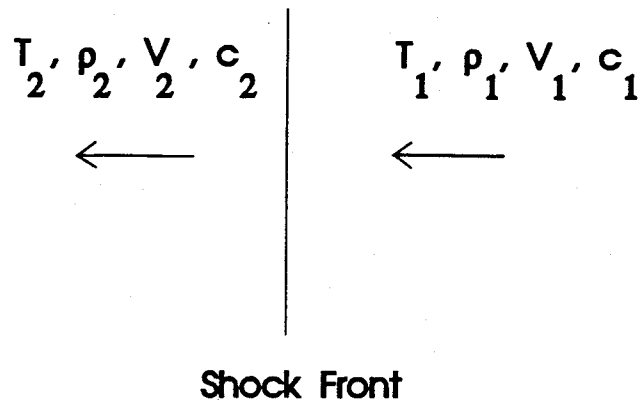

Figure 5: Shock Front Reference Frame.

integrated over the shock front then,

$$v_1\rho_1 = v_2\rho_2 = J \ , \tag{14}$$

where $v_i \rho_i$ represent the velocity and density in the region i, respectively. J is the mass flow per unit area per unit time across the shock front. This equation states simply that mass can neither be created nor destroyed at the shock front. Second, if the continuity equation and equation of motion are combined and integrated over the shock front, then the momentum flux density for the flow normal the shock is conserved, that is:

$$P_1 + \rho_1 v_1^2 = P_2 + \rho_2 v_2^2 \ , \tag{15}$$

where the term ρv^2 is the momentum flux density due to a fluid element, and the pressure term represents the momentum flux associated with ion and electron thermal motion. Third, the energy flux into the shock must be the same as the energy flux flowing out of the shock. Mathematically, this is equivalent to Bernoulli's principle which states that for compressible fluids:

$$\frac{1}{2}v_1^2 + \frac{P_1}{\rho_1} + \frac{u_1}{\rho_1} = \frac{1}{2}v_2^2 + \frac{P_2}{\rho_2} + \frac{u_2}{\rho_2}, \tag{16}$$

where u_i represents the specific internal energy of the fluid in region i (i=1,2). Only those fluid elements with components of velocity normal to the shock front undergo a discontinuous jump in density, temperature, and pressure. It is assumed at this stage that any magnetic fields which permeate the plasma jet do not affect the velocity components which are tangential to the jet or shock front. Hence, the tangential velocity components remain continuous across the shock front. By introducing the enthalpy $H = U + PV$, it is possible to solve for an expression which only depends on the initial and final thermodynamic state of the plasma and is independent of the jet velocity, v_1. Using equation (16) and $h = u + P$, where $h = \frac{H}{V}$ gives,

$$\frac{1}{2}v_1^2 + \frac{h_1}{\rho_1} = \frac{1}{2}v_2^2 + \frac{h_2}{\rho_2}.$$

Next using mass, momentum, and energy conservation to find an expression independent of v_1 and v_2 gives,

$$\frac{h_1}{\rho_1} - \frac{h_2}{\rho_2} + \frac{1}{2}\frac{\rho_1 + \rho_2}{\rho_1\rho_2}(P_2 - P_1) = 0.$$

Or using the explicit quantities gives,

$$H_1 - H_2 = \frac{1}{2}(P_1 - P_2)(V_1 + V_2). \tag{17}$$

Equation (17) defines the shock adiabat, or the so called "Hugoniot". Notice that this expression is independent of all dynamic variables, and hence defines a static relationship between the shocked and unshocked properties of the plasma. From examination of equation (17), it is seen that since $P_2 > P_1$, the shocked plasma enthalpy must be greater than the unshocked

enthalpy. The shock front of a plasma jet with cylindrical symmetry acts to create temperature, density, and pressure gradients in the $-\hat{z}$ and $-\hat{r}$ directions. If $M_1 \gg 2.4$, then the shock front raises temperature much more efficiently than density, as seen in Figure 2. Therefore, the generated temperature gradient will become larger than the density gradient in the $\hat{z}$ direction.

Equations (14), (15), (16) and the perfect gas law,

$$h = c_p T = \frac{\gamma}{\gamma - 1}\frac{P}{\rho} \quad \text{where} \quad \gamma = \frac{c_p}{c_v},$$

can now be used to derive all the classical relationships between the upstream and downstream properties of the plasma. For example:

$$\frac{\rho_2}{\rho_1} = \frac{(\gamma + 1)M_1^2}{(\gamma - 1)M_1^2 + 2}, \tag{18}$$

$$\frac{P_2}{P_1} = \frac{1 + \gamma M_1^2}{1 + \gamma M_2^2}, \tag{19}$$

$$\frac{T_2}{T_1} = [2 + (\gamma - 1)M_1^2]\,\frac{2\gamma M_1^2 - (\gamma - 1)}{(\gamma + 1)^2 M_1^2}, \tag{20}$$

where $M_1 = v_1/c_{s1}$ and $M_2 = v_2/c_{s2}$ are the upstream and downstream Mach numbers respectively. Equations (18) and (20) are plotted in Figure 2 for $\gamma = 1.66$ which corresponds to a monatomic gas.

Experimentally, the background nitrogen gas becomes ionized by the radiation emitted from the hot laser produced plasma ($\approx$ 100 eV). The electron temperature of the ionized background is assumed to be on the order of 1.0 eV. Ion acoustic velocity is calculated by:

$$c_s = \left[\frac{\gamma Z k T_e}{m_i}\right]^{1/2} = 9.79\times10^5\ \text{eV}^{-1/2}\sqrt{\frac{\gamma Z T_e}{\mu}}, \tag{21}$$

where c_s is the ion acoustic velocity in cm/sec, μ is the ratio of ion to proton

mass, Z is the ionization state of the gas, and T_e is the electron temperature in eV. Bird [Ref.2] experimentally measured the jet velocity to be approximately 2.8×10^6 cm/sec, with experimental error of about ±10%. The plasma jet Mach number is a function of the nitrogen background temperature. Using γ=1.66, Z=1, and μ=28 gives:

$$M_1 = \frac{11.75\ \mathrm{eV}^{1/2}}{\sqrt{T_1}} ,$$

where T_1 is the background temperature in eV. From equation (20) it is also evident that the Mach number is a function of $\frac{T_2}{T_1}$. Hence, T_2 is a function of T_1. This functional dependence is given by:

$$T_2 = -1.35\times10^{-3}\ \mathrm{eV}^{-1}\ T_1^2 + 0.846T_1 + 42.75\ \mathrm{eV} .$$

A background temperature of 1.0 eV then implies that the shock heated temperature is 43.6 eV, and the Mach number (M_1) is 11.75. This is a fairly strong shock, which implies that further excitations and ionizations will occur. N_2 and N_2^+ have dissociation potentials of 9.758 eV and 8.72 eV, respectively. Diatomic nitrogen's first ionization potential is 15.58 eV. Monatomic nitrogen has ionization potentials of 14.534 eV and 29.601 eV [Ref.3]. Likewise, aluminum has ionization potentials of 5.986 eV, 18.826 eV. and 28.448 eV. All these atomic processes are possible mechanisms of energy loss from the shock heated plasma. Energy used for excitations and ionizations will not contribute to raising electron temperatures to the theoretical level. Reduced thermal gradients imply smaller magnetic fields. The initial analysis completed here will neglect these losses and hence will yield magnetic field magnitudes which are too high. Assuming that shock heating of the electrons is on the order of 10% efficient, magnetic field magnitudes do fall in line with experiment.

The measured jet velocity given above was obtained at a background pressure of 700 mtorr, which was sufficiently high to cause shock formation. For pressures below about 200 mtorr, shock formation was not observed. At lower background pressures the plasma jet expanded with greater velocity (up to ≈ 10 times greater); however, dynamic gradients rapidly fall off due to free expansion so that significant self-generated magnetic fields are minimal and shock heating is nonexistent.

D. ELECTRON HEAT TRANSPORT

Cross field electron heat conduction is a much more complicated process which is still being studied today in connection with fusion confinement applications. Electron heat conduction across a magnetic field is a topic of continuing research, and one which is not very well understood. The third moment of the collisional Boltzmann equation describes the behavior of heat flow in a plasma with a 3-dimensional distribution function, $f(\vec{r},\vec{v},t)$, given by:

$$\frac{\partial f}{\partial t} + \vec{v} \cdot \nabla f + \frac{\vec{F}}{m} \cdot \frac{\partial f}{\partial \vec{v}} = \left[\frac{\partial f}{\partial t}\right]_c ,$$

where $\vec{F}$ represents body forces such as gravity or the Lorentz force. Multiplying the above equation by $\frac{1}{2}m\vec{v}$ and integrating over velocity space yields the third moment of the Boltzmann equation. Assuming the body forces are caused by a Lorentz force then the above equation becomes [Ref.5]:

$$\frac{1}{2}m \int v^2 \frac{\partial f}{\partial t} d\vec{v} + \frac{1}{2}m \int v^2 (\vec{v} \cdot \nabla f) d\vec{v} - \frac{e}{2} \int v^2 (\vec{E} + \vec{v} \times \vec{B}) \cdot \frac{\partial f}{\partial \vec{v}} d\vec{v} = \frac{m}{2} \int v^2 \left[\frac{\partial f}{\partial t}\right]_c d\vec{v}.$$

Performing the integration yields:

$$\frac{\partial}{\partial t}\left[\frac{nmv^2}{2} + \frac{3nkT}{2}\right] - n\vec{F} \cdot \vec{v} + \nabla \cdot \vec{H} = \frac{\partial}{\partial t}\left[\frac{nmv^2}{2}\right]_c ,$$

where $\vec{H}$ is energy flux and is given by,

$$\vec{H} = \frac{1}{2}\hat{n}m \int \vec{v}(\vec{v} \cdot \vec{v}) f(\vec{r},\vec{v},t)\, d\vec{v},$$

and n is the density given by,

$$n = \int \hat{n} f(\vec{r},\vec{v},t)\, d\vec{v},$$

where $\hat{n}$ is the average particle density given by $\frac{N}{V}$. The heat flux depends on the 3-dimensional distribution function of the electrons, which itself is not exactly known and must also be solved. Kinetic theory in this case does not provide a very eloquent solution to the electron heat transport problem. The problem, however, becomes more tractable if the specific nature of the electron and ion motion is analyzed. The electrons will be examined in this section. Ions will be examined in the next section. For this analysis it is assumed that experimentally measured density values are accurate and that the plasma is 100% ionized. Therefore, no neutrals are present. It is also assumed that ion density is equal to electron density and electron temperature is larger or equal to ion temperature in any given region. Although the second assumption may not be strictly valid, deviations within one order of magnitude do not change the physics of the mechanism. Important electron parameters such as mean free path (λ_e), Larmor radius ($r_{L,e}$), and the ratio of gyrofrequency to collision frequency ($\omega_c \tau|_e$) are calculated as a function of range from the plasma jet axis. All variables are in cgs units. Temperature is in eV. The electron mean free path (λ_e) is given by [Ref.4]:

$$\lambda_e = 3.4\times10^{13}\frac{(kT_e)^2}{n \ln\Lambda} \text{ cm} . \tag{22}$$

$\ln\Lambda$ is called the Coulomb logarithm and is included to account for the cumulative effect of small angle collisions, since these collisions occur much

more frequently than large angle collisions. Λ is defined as the average ratio of Debye length, λ_D, to the impact parameter radius, r_o:

$$\Lambda = \frac{\lambda_D}{r_o} = 12\pi n\, \lambda_D^3.$$

In laboratory plasmas, for example, if $n \approx 10^{11}\ \mathrm{cm}^{-3}$, and $kT_e = 2$ eV, then $\ln\Lambda = 10.2$. The logarithm of Λ is relatively insensitive to changes in plasma parameters. Assuming a gaussian temperature and density profile and $\ln\Lambda \approx 10$ gives:

$$\lambda_e = 1.07 \frac{((T_{\max} - T_{bg})e^{-r^2/\delta_{rT}^2} + T_{bg})^2}{((n_{\max} - n_{bg})e^{-r^2/\delta_{rn}^2} + n_{bg})}\ \mathrm{cm}\ .$$

$T_{\max}$ and T_{bg} are the maximum electron temperature and background electron temperature in eV, respectively. $n_{\max}$ and n_{bg} are the maximum electron density and background electron density in relative units, respectively. δ_{rn} is the radial electron density width and δ_{rT} is the radial electron temperature width. Now letting $T_{\max}$=43.597 eV, T_{bg}=1.0 eV, $n_{\max}$=14.9 r.u., δ_{rT}^2=0.3 cm^2, and δ_{rn}^2=0.3 cm^2 provides the curve in Figure 6. This analysis is one dimensional and assumes no axial (z) dependence.

Notice that λ_e reaches a minimum at about r=1.15 cm (λ_e=8 cm). Therefore, in the absence of the magnetic field, the electrons are essentially collisionless. It is the presence of the magnetic field which causes the electrons to gyrate about the field lines in relatively small gyromagnetic orbits ($r_{L,e} \approx \delta_{rn}$). This promotes electron-electron interactions which will rapidly provide a mechanism for heat transport. Notice that like-particles which collide (while executing gyro-motion) very efficiently transfer momentum and energy. The Larmor radius ($r_{L,e}$) is given by:

$$r_{L,e} = \frac{v_{the}}{\omega_c} = 2.38\ \frac{\mathrm{Gauss\,cm}}{\mathrm{eV}^{1/2}}\ \frac{T^{1/2}}{B}\ ,$$

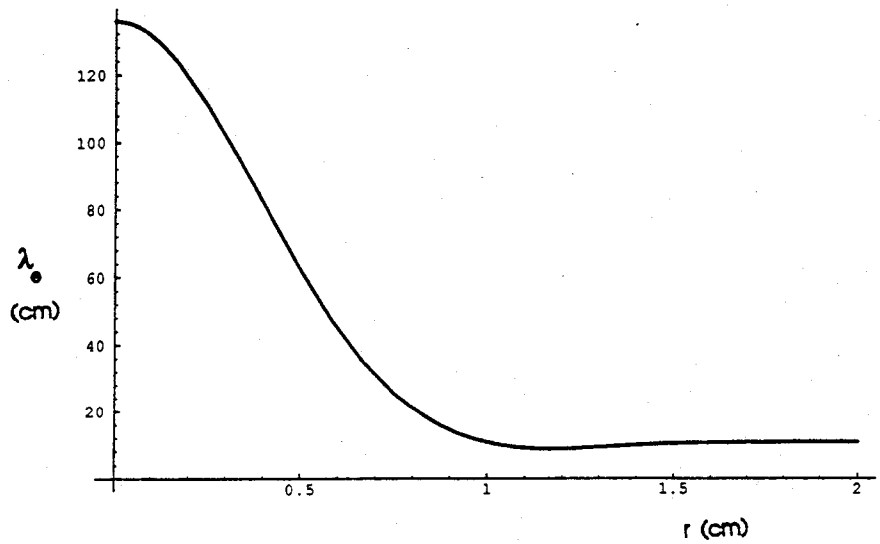

Figure 6: Electron Mean Free Path versus Distance from Plasma Jet Axis.

where v_{the} is the electron thermal velocity, ω_c is the electron gyrofrequency. The magnetic field, B, for the purposes of these examinations is assumed to be approximated by:

$$B(r) = 2309.1 \text{ Gauss cm}^{-2}\, r^2 e^{-r/0.2\text{cm}} ,$$

as is shown in Figure 7a.

This profile ensures that the maximum magnetic field is 50 Gauss at r=0.4 cm and 0 Gauss on the axis, r=0 cm. Using this, the Larmor radius (as a function of radius) becomes:

$$r_{L,e} = 2.38 \text{ Gauss cm eV}^{-1/2} \frac{((T_{\max} - T_{bg})e^{-r^2/\delta_{rT}^2} + T_{bg})^{1/2}}{2309.1\, r^2 e^{-r/0.2\text{cm}}} .$$

This is shown in Figure 7b. Notice that between r=0.4 cm and r=1.1 cm the Larmor radius is small enough so that the electron will complete a full gyration within the size typical of the plasma jet. The ratio of gyrofrequency

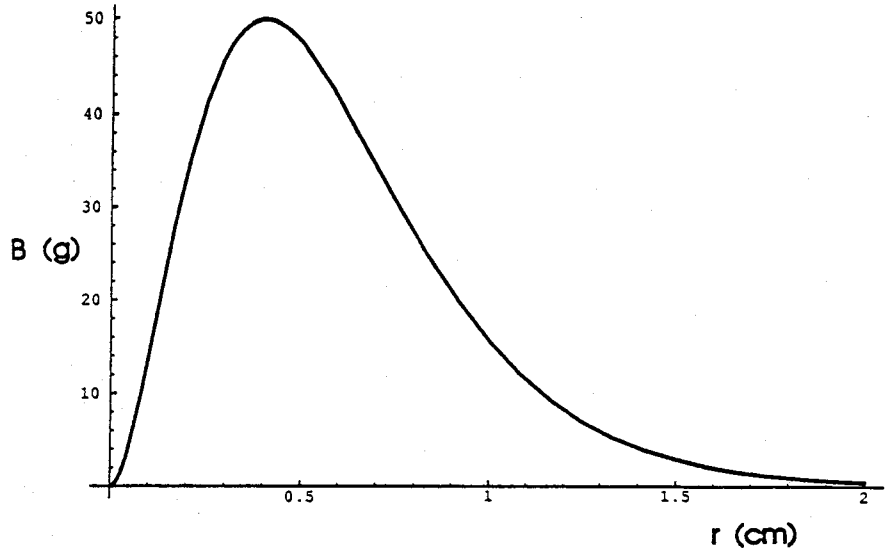

Figure 7a: Assumed magnetic field as a function of range from jet axis. This ensures B=0 Gauss at r=0 cm and B=50 Gauss at r=0.4 cm.

to collision frequency for the electron is given by:

$$\omega_c \tau|_e = 0.0152 \text{ Gauss}^{-1} \text{ eV}^{-3/2} \text{ r.u. } \frac{((T_{\max} - T_{bg})e^{-r^2/\delta_{rT}^2} + T_{bg})^{3/2}}{((n_{\max} - n_{bg})e^{-r^2/\delta_{rn}^2} + n_{bg})} B \ .$$

This is shown in Figure 8.

Inside r=1.1 cm, the electrons are magnetized and execute gyro-motion about the magnetic field lines. Although electron-electron collisions in this region do not produce particle diffusion, they do efficiently produce thermal diffusion. Beyond r=1.1 cm, the electrons are unmagnetized and move freely with the electron thermal velocity. As shown in Figure 6, the electrons essentially exist in a collisionless plasma (due to their high temperature) and are only constrained due to the presence of a magnetic field. Thermal diffusion of heat can be described by Bohm diffusion. An approximate transport rate or diffusion velocity can be calculated, and is given by:

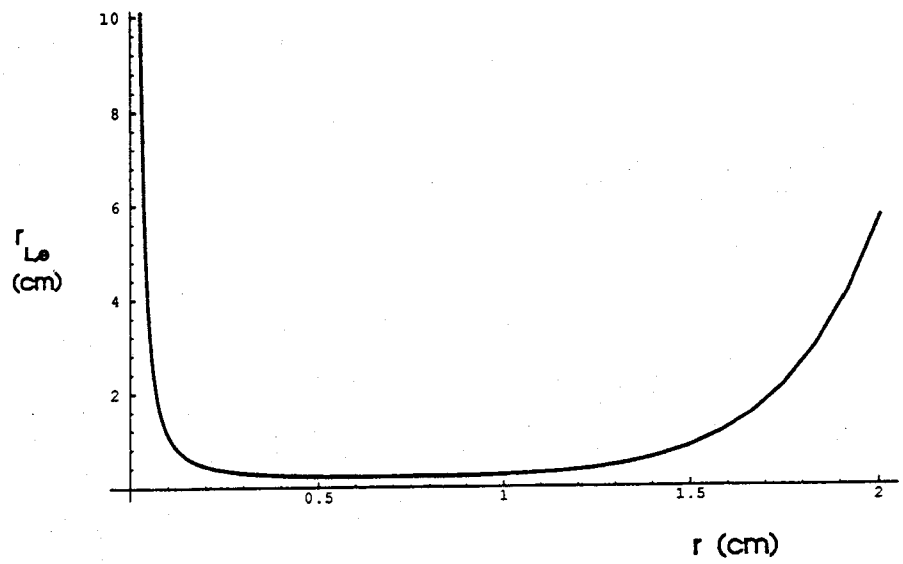

Figure 7b: Electron Larmor Radius versus Distance from Plasma Jet Axis.

$$v_B = \frac{D_B}{\delta_{rn}}, \tag{23}$$

where D_B is the Bohm diffusion coefficient and δ_{rn} is the radial size of the plasma jet. The Bohm diffusion coefficient is given by:

$$D_B = \frac{1}{16}\frac{kT_e}{eB} = D_{\perp}. \tag{24}$$

Assuming kT_e=10 eV, B=50 Gauss, and δ_{rn}=0.5 cm; implies $v_B = 4.2\times10^6$ cm/sec. Comparing v_B with v_{thi} ($v_{thi} = 1.2\times10^6$ cm/sec) shows that heat transport occurs faster than density (or particle) transport. This is supported by the program pl7.c which simulates the two-dimensional diffusion of a plasma column. Specific results of pl7.c will be discussed in detail.

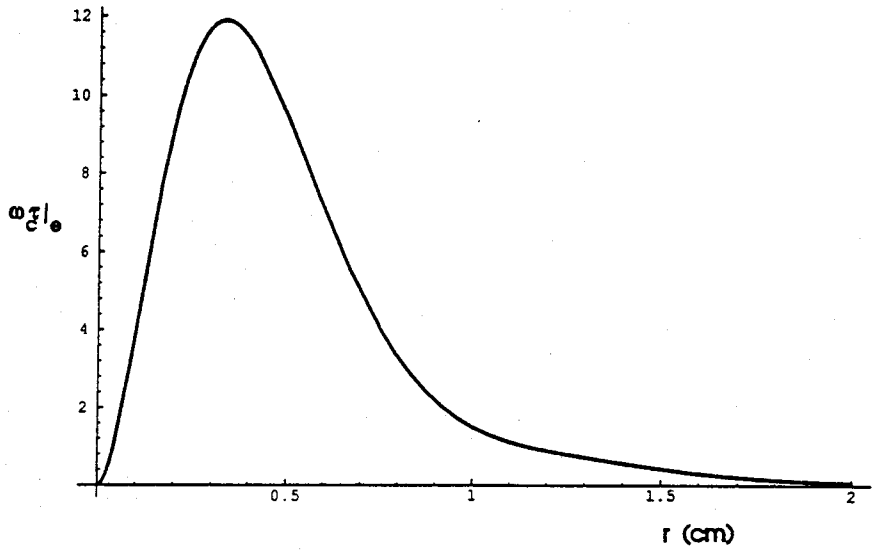

Figure 8: Ratio of Electron Gyrofrequency to Collision Frequency versus Distance from the Plasma Jet Axis.

Bohm diffusion describes particle diffusion of a fully ionized plasma in the presence of a magnetic field. Bohm diffusion has historically provided reasonable agreement with experiments. The Bohm diffusion coefficient is based on a semiempirical formula. Notice that the diffusion coefficient depends on the inverse magnetic field and is proportional to the temperature. This is contrary to "classical" cross field diffusion theory, where the diffusion coefficient is proportional to the inverse square of the magnetic field. Now assuming electron temperature diffusion is determined by Bohm diffusion within the electron fluid, the temperature diffusion equation is:

$$\frac{\partial T_e}{\partial t} = \nabla \cdot (D_B \nabla T_e) \,, \tag{25}$$

where the electron temperature is the property being diffused across the

magnetic field. The characteristic temporal decay in Bohm diffusion is exponential. The time constant for this decay in a cylindrical plasma column of radius (R), length (L), and temperature (T) can be estimated to be [Ref.4],

$$\tau \approx \frac{T}{dT/dt} = \frac{\rho_E \pi R^2 L}{\Gamma_r 2\pi R L} = \rho_E \frac{R}{2\Gamma_r},$$

where $\Gamma_r = D_B \partial\rho_E/\partial r$, is the energy flux and ρ_E is the energy density. Using this in the above equation gives:

$$\tau \approx \frac{R^2}{2D_B} = \tau_B. \tag{26}$$

where τ_B is the Bohm time. For the plasma jet experiments examined here: $kT_e \approx 10.0$ eV, B=50 Gauss, and R=0.5 cm; which implies τ_B = 100 nsec. Since τ_{exp} (the characteristic time scale of the experiment) is the same order of magnitude as the Bohm time, τ_B, detectable heat transport and radial particle migration will occur. In agreement with experimental results, the plasma jet expands about 1 cm in the radial direction in the time scale of the experiment. This was supported by numerical simulations performed by pl7.c, which simulated the radial two-dimensional diffusion of a gaussian plasma column under conditions similar to those encountered experimentally. It should be emphasized that the simulations shown in Figures 9a and 9b show radial electron density and temperature diffusion across the magnetic field assuming no axial flow. That is, the plasma is assumed to be two dimensional (r, θ) and hence does not expand in the axial direction. The plasma is assumed to have azimuthal symmetry and is expanding radially into a magnetic field which is constant in both space and time. See Figures 9a and 9b. The vertical lines depicted in the figures indicate that the electron temperature and density are assumed to be maintained constant by the shock front. Electron temperature and density

are assumed to be constant out to an incident angle of 60 degrees, which corresponds to the ½ downpoint.

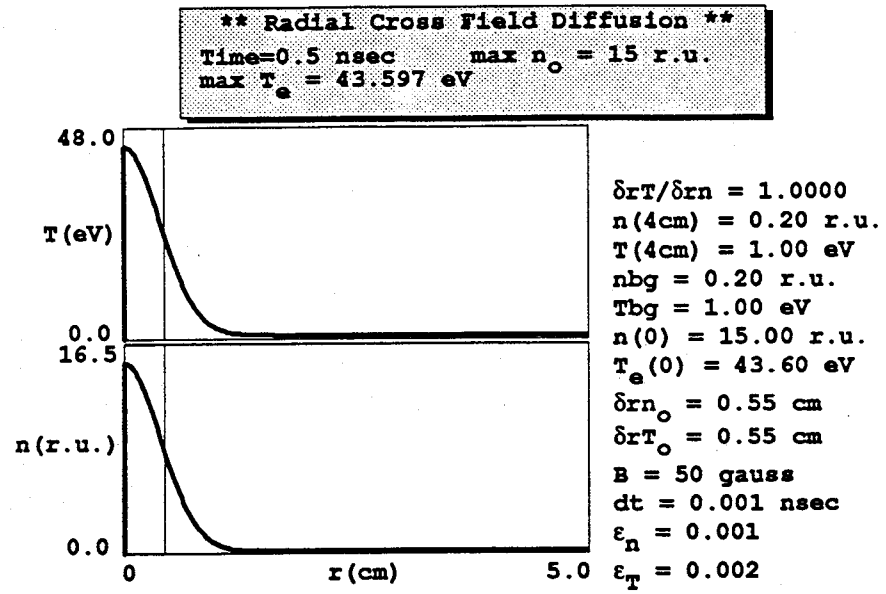

Figure 9a: Numerical Simulation of Thermal and Density Diffusion using pl7.c at 0.5 nsec. This figure is enclosed as an example of the initial profile present. Shock heating maintains electron temperature and density constant out to the vertical line (≈ 0.4 cm).

A copy of pl7.c is enclosed in the appendix. Further discussion about simulated parameters will follow in subsequent sections of this thesis. It is physically expected that the radial density diffusion will be slow compared to the time scales of jet axial expansion (10^{-7} sec). This is because plasma density diffusion is dominated by ion motion which occurs more slowly, due to the slower ion sound velocity. Figures 9a and 9b show ion diffusion and thermal Bohm diffusion. Ion diffusion will be discussed in the next section. The following typical values were used in the simulation: B=50 Gauss, kT_e=43.6 eV, and a maximum plasma density of 15.0 relative units. The relative units denote actual density measurements by electric double probes.

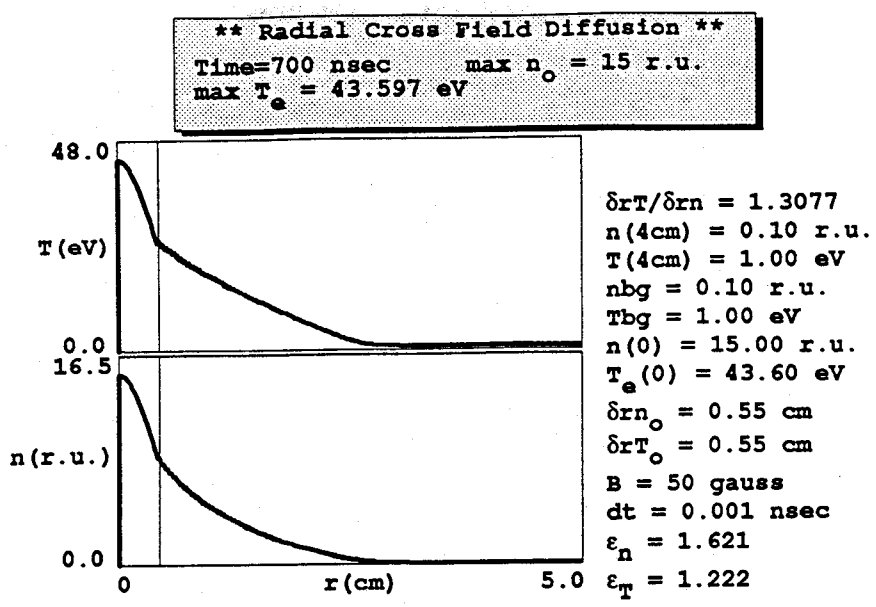

Figure 9b: Numerical Simulation of Thermal and Density Diffusion using pl7.c at 700 nsec. Shock heating maintains electron temperature and density constant out to the vertical line (≈ 0.4 cm).

The relationship between the relative units of density and density in particles/cm^3 is given by:

$$\frac{\text{particles}}{\text{cm}^3} = 3.18\times10^{12} \times V_{mp},$$

where V_{mp} is the measured potential drop in volts, as obtained by the current to an electric dipole density probe. This conversion factor can be used to convert to conventional density units; however, this will prove to be unnecessary for the work presented here. It should be mentioned again that axial expansion was intentionally omitted (in pl7.c) because the specific effects due to radial cross field diffusion wanted to be simulated. This objective was accomplished.

Given that the plasma jet is supersonic with $M_1 = 11.75$, it is now possible to calculate (using equations (18), (19), and (20)) the increases in temperature, pressure, and density across the shock. For example, the temperature increases by a factor of 43.6 across the shock front assuming no ionization or radiation losses. The plasma is shock heated to approximately 43 eV. Numerical simulations (pl7.c) show that when shock heating occurs, magnetic field reversal occurs because the radial temperature gradient relaxes radially at a faster rate than does the density gradient. It should be noted that this phenomenon also occurs in the axial direction. Electrons rapidly conduct some of their thermal energy outward in front of the shock and "pre-heat" the incoming electrons. This can be seen when comparing the shock velocity, $v_{sh} = 3\times10^6$ cm/sec, to the Bohm diffusion velocity. Electron temperature propagates ahead of the shock and pre-heats the incoming electrons. This will be analyzed and discussed further in Chapter V section F. Density diffusion of the plasma jet in the radial direction across $\vec{B}$ can be analyzed using classical particle diffusion theory. This is possible because the ions are not magnetized ($\omega_c\tau|_i < 1$) and have a large mean free path ($\lambda_i \gg 0.5$ cm). The ions essentially disperse radially at their respective thermal velocity. Ion diffusion will be discussed further in the next section. If there is no initial magnetic field present when shock heating begins then it is worth noting that the electrons will not be constrained by a magnetic field. Therefore, the electrons will also be collisionless due to their high temperature and propagate away from the plasma jet (within the limits imposed by quasineutrality) and form a bi-layer. Chapter IV will show that this freedom will generate even larger shock generated fields (because δ_{rT}/δ_{rn} is larger).

Before going on to the next section it should be mentioned that the Tokamak fusion reactor has produced similar "anomalous" behavior where

the cross field electron heat transport rate greatly exceeds the particle diffusion rate. These large electron heat transport rates are still under study and are not fully understood in the fusion application.

E. ION DIFFUSION

Particle diffusion in the radial direction is dictated by ion motion. In the axial direction the ions undergo directed motion due to the energy received during the laser blast. The mean free path for the ions is much larger than the characteristic size of the plasma jet (λ_i = 28 cm at r=0 cm; λ_i = 2 cm at r=1.1 cm). The decrease in the mean free path along r is due to the ion temperature gradient. The Larmor radius for the ions has a minimum of about 50 cm at approximately r=0.6 cm. Therefore, it is evident that the ions are essentially collisionless and travel straight paths since their Larmor radius is so large ($r_{L,i} \gg \delta_{rn}$). That is, the ions are not magnetized ($\omega_c \tau|_i < 1$). This implies that the ions expand out radially at the ion sound velocity given by (assuming $T_i \approx T_e$):

$$v_{thi} = \left[\frac{kT_e}{m_i}\right]^{1/2} = 9.79\times10^5 \text{ cm sec}^{-1} \text{ eV}^{-1/2} \frac{T_e^{1/2}}{\mu^{1/2}}, \tag{27}$$

where T_e is in eV, and μ is the ion to proton mass ratio, and v_{thi} is in cm/sec. Using T_e=43 eV and μ=28 for the shock heated plasma implies v_{thi} = 1.2×10^6 cm/sec. The shock velocity is 3×10^6 cm/sec. Comparing these two velocities (v_{thi}/v_{sh} = 0.4) shows why the plasma jet expands faster in the axial direction than in the radial direction. The jet experiences directed motion in the axial direction while expanding at the ion sound velocity in the radial direction. Given that v_{thi} = 1.2×10^6 cm/sec, implies that in 200 nsec the plasma jet radially expands about 0.24 cm which is in agreement with experiment.

Although electron heat transport occurs more rapidly than ion particle transport, electron particle transport occurs at the same rate as ion particle transport. Due to the coulombic interaction between ions and electrons, any charge separation results in an electric field which accelerates electrons back to the ions and visa versa. Therefore, the radial electron density gradients relax at the ion sound velocity. Classical particle diffusion is mathematically described by:

$$\frac{\partial n}{\partial t} = D \nabla^2 n \ , \tag{28}$$

where D is the particle diffusion coefficient. The relationship between the particle diffusion coefficient and other fundamental constants is given by [Ref.6]:

$$D = \frac{\lambda_i^2}{\tau_i}, \tag{29}$$

where λ_i is the mean free path between collisions (which may also be considered to be the average displacement in a collision); τ_i is the characteristic collision time, or time between collisions.

Using the "bi-diffusive" density-temperature model described in this chapter, in conjunction with axial shock heating, the following chapters will provide experimental results and numerical simulations as evidence for this model.

Shock generated magnetic fields are produced by the bi-diffusive nature of the plasma, i.e. electron temperature diffuses more quickly than electron density. The shock front provides a source of heating while the bi-diffusivity provides the proper arrangement of gradients. Previous studies completed on plasma jets provided several models to specifically explain field reversal phenomena. The "bi-diffusive" density-temperature diffusion model is the only model consistent with source term simulations.

III. PREVIOUS EXPERIMENTAL WORK

A. INTRODUCTION

Self-generated magnetic fields produced by laser plasmas were first studied and detected by Stamper [Ref.7] in 1971. Stamper used a neodymium doped glass laser with an output of 60 joules in 30 nanoseconds to target a 250 micron fiber of Lucite. The Lucite fiber was suspended in an inert nitrogen background. Magnetic fields were detected that expanded with the same velocity as the expanding plasma jet. The fields were essentially azimuthal with respect to the jet. Magnetic fields up to 1000 Gauss were measured in a nitrogen background of 200 mtorr. Later in 1971, Dean [Ref.8], studied the interaction between two counterstreaming plasmas produced by laser irradiation of fiber targets in a background nitrogen gas. Dean essentially used the same experimental apparatus and found the following: (1) a well defined front exists at the leading edge of the jet, (2) interactions which occur at the front are strongly dependent on background gas pressure, (3) the front thickness was approximately 1-2 mm, (4) the front was modeled as a shell of increased density.

Reversal of the azimuthal magnetic field direction at the leading tip of the plasma jet at sufficiently high background pressures (>200 mtorr) was first observed by McKee [Ref.1] at the Naval Postgraduate School in 1971. McKee used a Korad-k-1500 Q switched neodymium doped glass laser which delivers approximately 6.6 Joules in a pulse of 22 nanosecond duration. This equates to approximately 300 megawatts of power. These intense pulses of laser light then irradiate aluminum targets which have been placed in an

evacuated chamber typically between 5×10^{-5} and 0.7 torr of inert gas pressure. The laser strikes the target at 30 degrees off normal to prevent laser-target plasma interference. Since that discovery, several graduate students at the Naval Postgraduate School have attempted to explain this reversal phenomenon. This is the first thesis known to the author which proposes that this reversal is the fingerprint of shock generated magnetic fields. Previous experimental works will be discussed in this chapter.

B. MCKEE'S "SHELL" MODEL

McKee [Ref.1] later adopted the "shell" model in his Ph.D. thesis to account for the phenomenon of magnetic field reversal at the jet front at later times (300 nsec) in background pressures greater than 200 mtorr. In the "shell" model the expanding plasma jet is thought to cause a "pile up" of background gas at the leading edge of the jet. This "pile up" forms a region of high density directly in front of the plasma jet. The expanding laser plasma acts to compress and heat the background in a "shell" which surrounds the expanding front of the jet. See Figure 10.

This "shell" travels with the jet and also causes additional temperature and density gradients to be formed. In this way, the background gas interacts with the expanding laser plasma. McKee additionally attributed field reversal at background pressures higher than 200 mtorr to these secondary gradients formed by the "shell". That is, as the expanding jet formed a frontal "shell", the region between the shell and the laser plasma would develop temperature and density gradients in the $+\hat{z}$ direction (see Figure 10). The source term in equation (10) shows that if the direction of the axial gradients reverses, then the cross product changes sign and magnetic field reversal begins. This is seen more explicitly if the source term is written as:

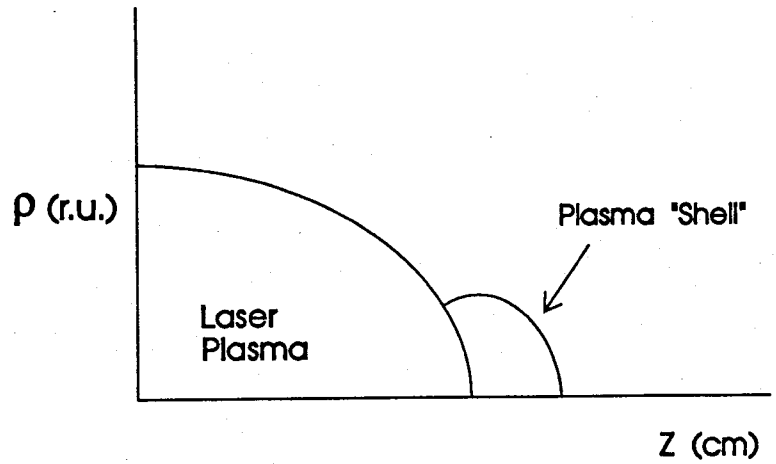

Figure 10: Shell Model proposed by McKee. [Ref.2]

$$S = \frac{k}{e}\nabla T_e \times \frac{1}{n_e}\nabla n_e = \frac{k}{en_e}\left[\frac{\partial T_e}{\partial z}\frac{\partial n_e}{\partial r} - \frac{\partial T_e}{\partial r}\frac{\partial n_e}{\partial z}\right]\hat{\theta},$$

where now the axial gradients are in the $+\hat{z}$ direction. In the shell model, the shell never actually transverses the plasma jet front, and therefore differs greatly from the model proposed in this thesis. McKee's work provided extensive spatial and temporal two-dimensional mappings of the magnetic fields at three principle background pressures: 0.1 mtorr, 5 mtorr, and 250 mtorr. McKee's data provided very little contour data concerning reversal phenomena since this phenomenon is not discernible until about 200 mtorr. However, some reversal effects are seen at 250 mtorr. McKee provided the following conclusions: (1) the self-generated magnetic fields were indeed generated by conduction currents producted by non-parallel gradients, (2) fields were initially clockwise as viewed in Figure 1, then as field reversal occurs the fields are counterclockwise (Figure 3), (3) the fields are azimuthally symmetric, and (4) the magnitudes of the generated

magnetic fields are amplified by the existence of a background gas. According to McKee's conclusions, the initial field direction implies that:

$$\left| \frac{\partial T_e}{\partial r} \frac{\partial n_e}{\partial z} \right| > \left| \frac{\partial T_e}{\partial z} \frac{\partial n_e}{\partial r} \right| ,$$

where when shock heating and hence field reversal occurs:

$$\left| \frac{\partial T_e}{\partial z} \frac{\partial n_e}{\partial r} \right| > \left| \frac{\partial T_e}{\partial r} \frac{\partial n_e}{\partial z} \right| .$$

C. BIRD'S WORK

Bird [Ref.2] continued McKee's investigation of self-generated magnetic fields produced by laser plasmas. McKee's study was mainly limited to magnetic contour mapping and characteristics of the fields in various background pressures of nitrogen up to 250 mtorr. Bird completed a thorough plasma density mapping using electric double probes. The additional data provided by Bird made it possible to associate particular magnetic phenomena (such as field reversal) with specific density structures of the laser plasma. Bird also analyzed the behavior of plasma jets in various background gases (such as H_2, He, N_2, and Ar) up to 700 mtorr. This provided good field reversal data. Bird also conducted some relatively high pressure experiments at 5 torr H_2. The results are shown in Figure 11 which shows the measured density profiles n_i and the magnetic field B as functions of time at locations r=0.4 cm from the axis, $\theta = 0^o$, and z=0.4 cm, 0.8 cm, 1.0 cm, and 2.0 cm from the target surface. Field reversal is dominant at the jet front. In fact, the reverse field magnitude grows very rapidly until it is the dominant field present. This high pressure example shows that the shock mechanism produces significant reversed fields.

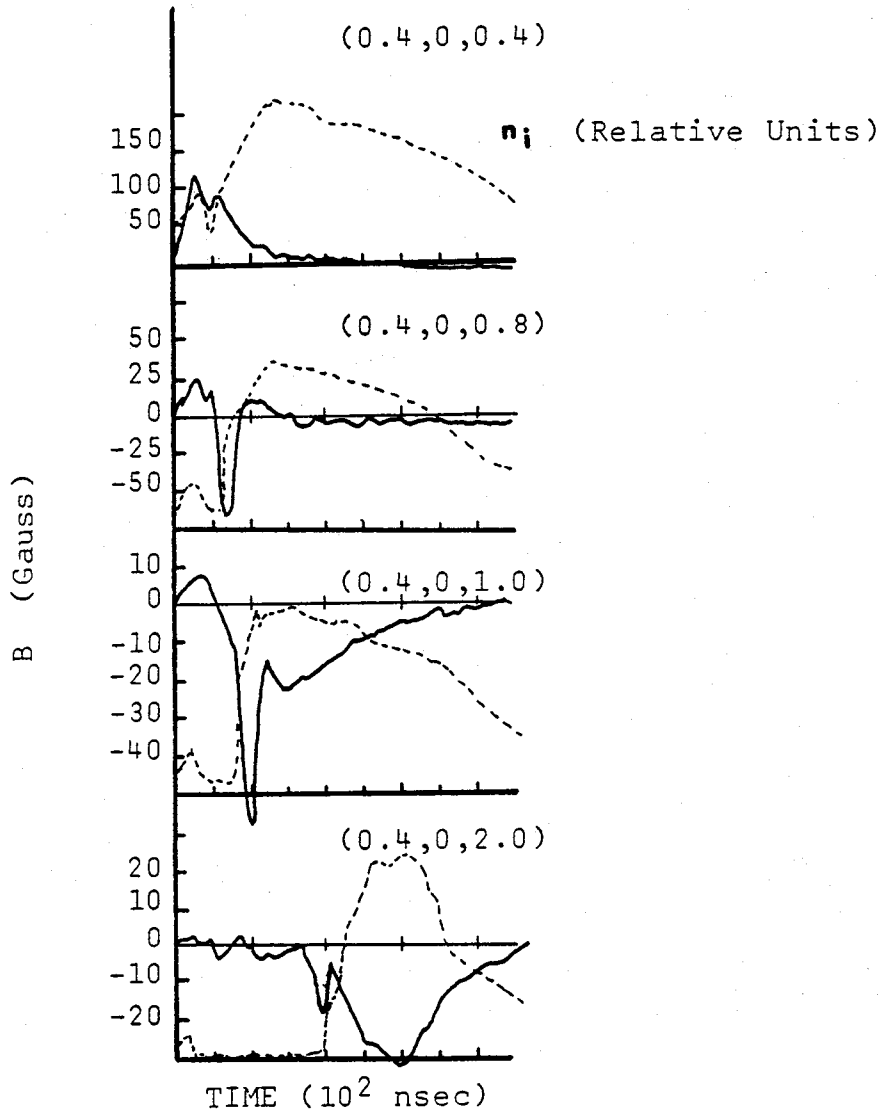

Figure 11: Field Reversal in a Plasma Jet in 5 torr of H_2. Negative field values represent Shock Generated Field. [Ref.2]

Bird was also able to draw definite conclusions about the spatial relationships between the generated magnetic fields and measured plasma jet density distribution. Some of Bird's major conclusions follow. First, the "shell" model proposed by McKee to explain the background pressure dependence of the magnetic field was flawed. Density mappings completed by Bird were unable to detect a density "shell". Work performed by Dean [Ref.8] showed, using three independent techniques, that a "shell" type structure did exist; therefore Bird concluded that an analogous structure must actually exist at the front of the expanding plasma jet. The density "shell" found by Dean, however, is different than the "shell" conceived by McKee in Figure 10. It is contended in this thesis that the "shell" structure found by Dean is instead the shock front at the leading edge of the plasma jet. Second, Bird proposed a model which attributes the increase in the magnetic field with background pressure to interactions between the photoionized background plasma and laser plasma during laser irradiation. Third, because Bird performed his investigation at background pressures above 200 mtorr, he observed extensive reverse field phenomena. Bird observed that field reversal appeared to be due to a "pile up or (re-thermalization)" of the laser plasma as it propagated through the background plasma. This "pile up" produces axial electron temperature gradients at the laser plasma front and reverses the generated magnetic field in accordance with the source term in equation (10). Bird, however, explains the heating mechanism at the "pile up" to be convective in nature (again, this thesis contends that the heating mechanism is instead completely attributable to shock heating). Fourth, reverse fields are generated long after the cessation of the laser pulse (1 μsec). Fifth, the onset of field reversal is delayed at lower background pressures because "pile up" of the background plasma requires more time. This effect can be explained

using the shock model. Since shock heating is the mechanism for field reversal, at lower background pressures weaker shock fronts are formed. A weaker shock front provides less shock heating and a smaller discontinuity in density and temperature, hence density and temperature gradients are smaller. Reduced gradients lengthen the onset of field reversal and also decreases the overall magnitude of the fields produced. Bird's density data was used to produce a mathematical model of the density mappings. These mathematically modeled density profiles were then used in a computer simulation to predict generated magnetic fields produced by shock heating.

D. BROOKS' WORK

Brooks [Ref.9] in late 1973 conducted laser plasma experiments, similar to McKee and Bird, in a vacuum of 2.5×10^{-5} torr (air). Brooks provided detailed analysis of plasma jet free expansion and target damage due to irradiation. Two dimensional contour mappings of plasma density were created which confirmed the fact that density gradients begin to decay from the onset of jet expansion. Relaxation times for radial gradients were actually much longer than relaxation times associated with axial gradients. Brooks explained this to be due to the fact that a radial "pinching" ($\vec{J}\times\vec{B}$) force prevented expansion in the radial direction. A maximum field of 200 Gauss corresponded to a current density of about 400 amps/cm^2. This indicated the presence of a $\vec{J}\times\vec{B}$ force density of approximately 7×10^4 N/m^3. The ratio of the $\vec{J}\times\vec{B}$ force to the radial pressure gradient force density is less than one. The radial pressure gradient force is given by:

$$\frac{nkT}{l} = 6.6\times10^6 \text{ N/m}^3$$

where l is the characteristic length of the density gradient (≈ 0.5 cm), $n = 4.8\times10^{13}$ cm^{-3}, and assuming a conservative $kT = 43$ eV. That is, the

"pinching" alone does not prevent expansion in the radial direction. The relatively slow ion thermal velocity provides "containment" in the radial direction (see Figure 12). Notice the free expansion in the axial direction.

A plot of $\vec{J}\times\vec{B}$ force density measured by McKee at 120 nsec in a background of N_2 gas (250 mtorr) is shown in Figure 13. Arrow length is proportional to force density. The largest force density at this time was 1.4×10^4 N/m^3. Brooks concluded that the $\vec{J}\times\vec{B}$ force provided at least "partial containment" of the laser plasma; however, he never hypothesized what other confinement mechanisms may be responsible. An additional contributor to the slow radial expansion is the directed motion of the ions in the axial direction due to the laser blast effects.

E. BARRIER SHOCK

Schwirzke [Ref.10,11] published results in the summer of 1973 which showed that if a glass plate is placed in the path of the expanding jet, then the rapid deceleration of the jet at the plate causes a shock to form. This shock also causes field reversal, but at pressures far below the pressures required to achieve shock heating without an impinging glass plate barrier. Figure 14 shows the results of an experiment performed at 5 mtorr N_2 with and without an obstructing glass plate. The glass plate was placed at z = 1.15 cm, and data was recorded along r = 0.3 cm. Data for the no plate case was recorded at z = 1.0 cm, r = 0.3 cm. Notice that up to 100 nsec the generated magnetic field for the two cases is the same. After 100 nsec however, the reversed field component is clearly distinguishable. Propagating 1.15 cm in 100 nsec corresponds to a velocity of 1.15×10^7 cm/sec, which agrees well with the measured jet velocity at this background pressure. After 700 nsec the two cases again approach the same field value. This shows that field reversal can be achieved at low background pressures

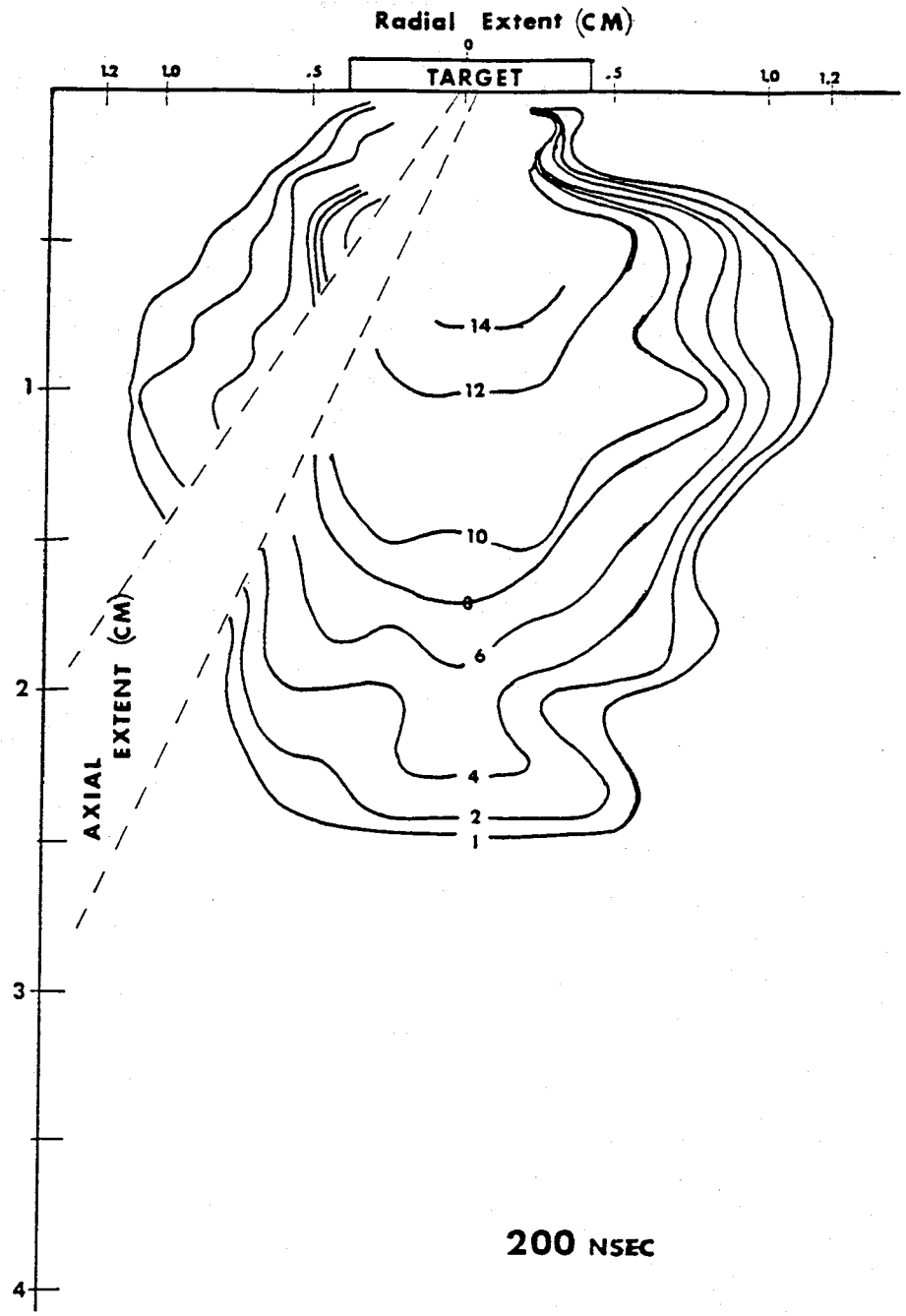

Figure 12: Density Contours of the Free Expansion of the Plasma Jet at Time 200 nsec.[Ref.9]

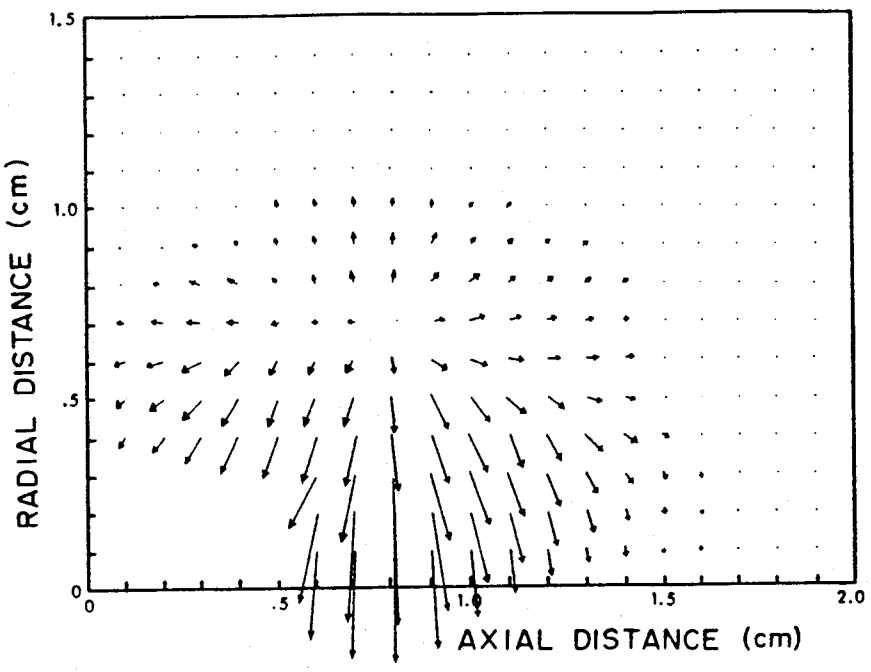

Figure 13: $\vec{J}\times\vec{B}$ Force Exerted of a Plasma Jet. $\vec{J}\times\vec{B}$ force density at 120 nsec for 250 mtorr of N_2 background gas. The magnitude of the force at this time is 1.4×10^4 N/m^3. [Ref.1]

if the plasma jet is rapidly decelerated by a barrier. The rapid deceleration causes shock formation and hence generation of a shock magnetic field whose azimuthal component is reversed in direction near the shock location. The bottom curve in Figure 14 shows the magnitude of the reversed (shock generated) field alone. This was derived by subtracting the no plate curve from the plate curve. Notice the maximum reversed (shock generated) field approaches 200 Gauss at about 340 nsec.

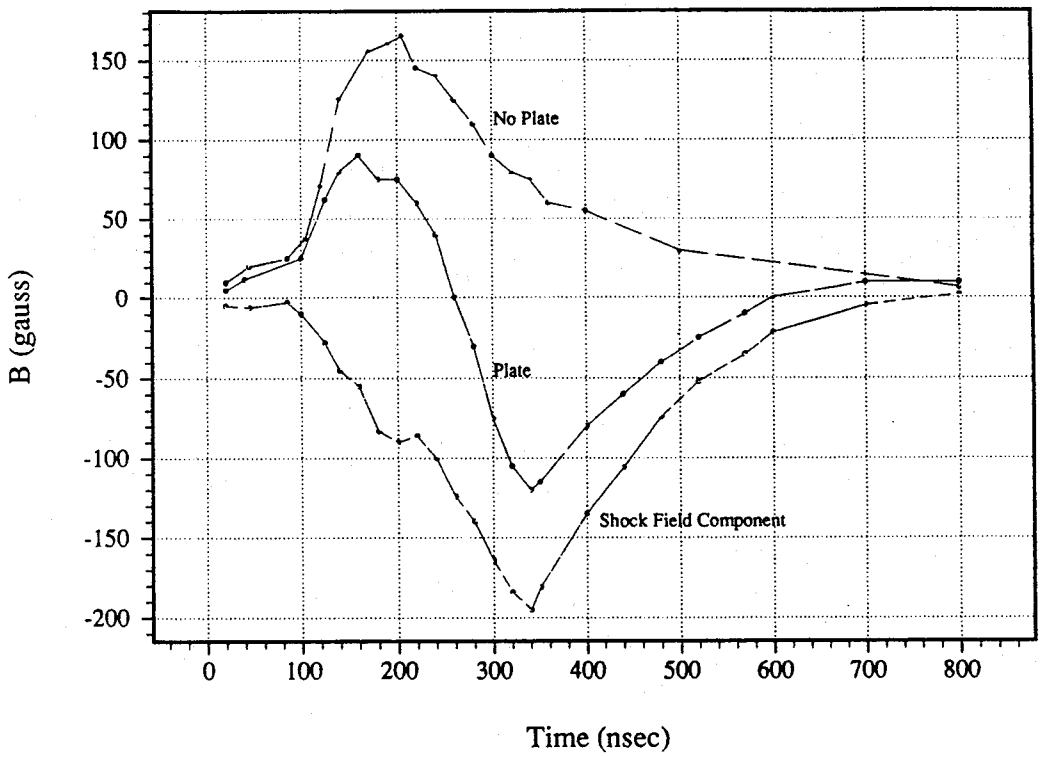

Figure 14: Jet Propagation into a Glass Barrier at z=1.15 cm in a 5 mtorr N_2 background. [Ref.10,11]

IV. NUMERICAL SIMULATION

A. PL2.C

As mentioned earlier, a numerical computer simulation was written to aid in understanding which arrangement of density and temperature gradients yielded the observed phenomena. In this way it became possible to indirectly obtain estimates of the required electron temperature gradients which were, before this thesis, unknown and unmeasured. Bird's work [Ref.2] provided excellent data to create a mathematical description of the density gradients present at high background pressures. Once mathematical expressions for density and temperature gradients were obtained, a simulation calculated $\nabla T_e \times \nabla n_e$, the field production rate. Section C discusses the actual structure of the program. This section will motivate the purpose of the program. A surprising result showed that magnetic field reversal occurred under only one combination of the temperature and density gradients. Let δ_{zT} denote the characteristic axial gradient width of the temperature, and δ_{rn} denote the characteristic radial gradient width of the density. Reverse (shock generated) magnetic field production at the front of plasma jet requires that:

$$\frac{|\nabla_z T_e||\nabla_r n_e|}{|\nabla_r T_e||\nabla_z n_e|} > 1.$$

Approximating the gradients by:

$$\nabla_z T_e \approx \frac{T_e}{\delta_{zT}}, \quad \nabla_z n_e \approx \frac{n_e}{\delta_{zn}}, \quad \nabla_r T_e \approx \frac{T_e}{\delta_{rT}}, \quad \nabla_r n_e \approx \frac{n_e}{\delta_{rn}},$$

gives:

$$\frac{(\delta_{zn})(\delta_{rT})}{(\delta_{zT})(\delta_{rn})} > 1.$$

Shock compression in the axial direction implies that the shock width is:

$$\delta_{zT} \approx \delta_{zn} \quad \text{while} \quad \delta_{zT} \ll \delta_{rT}.$$

Rapid electron heat conduction in the radial direction ensures that:

$$\delta_{rT} > \delta_{rn}.$$

Therefore, the ratio of the characteristic widths given above is indeed greater than one, and reversed fields are produced. Reverse fields will hereafter be referred to as shock generated fields. As mentioned earlier, in actuality electron pre-heating occurs in the axial direction. However, the pre-heating effect does not lengthen δ_{zT} to the extent that it causes the above ratio to be less than one. The radial temperature diffusion is the dominant mechanism.

Although density gradients were relatively well known by measured results, temperature gradients were adjusted to yield the observed phenomena. It quickly became apparent that maximum electron temperatures on the order of 40 eV were sufficient to produce the observed magnetic fields. It should be noted that the simulation does not calculate the magnetic fields generated very early on (<30 nsec) by the incident laser radiation. At these early times, magnetic field production is dominated by radial temperature gradients created by the laser and axial density gradients created by the expanding, ionized, dense target material. As discussed earlier, these fields diffuse slowly and tend to be carried out with the plasma jet. After cessation of the laser, the "frozen in" magnetic field is modified by the shock-generated magnetic fields created by the gradients present. The numerical simulation, pl2.c, simulates the post-laser self-

generated magnetic fields only. pl2.c is a computer code written in the C programming language. A copy of pl2.c is attached as an appendix at the end of this thesis. The density profiles modeled by pl2.c were obtained from experimental data taken by Bird. To ensure shock formation and hence field reversal, pl2.c uses data obtained from measurements taken at a background pressure of 700 mtorr. Other pressures could have easily been used, however, 700 mtorr provides the most interesting example. Figures 15a through 15h show Bird's data for this case. All these measurements were made at r=0.4 cm and $\theta = 0^o$. This implies that the data does not accurately represent the plasma density present for times less than 200 nsec because the plasma front does not arrive until that time. This can be seen when comparing Figures 15b and 15c. The shock generated magnetic field shows up at 300 nsec at the steepest part of the axial density profile. For a given set of gradients, the magnetic field increases with time:

$$\int_{t_1}^{t_2} \frac{\partial B}{\partial t}\, dt = B(t_2) - B(t_1) = \frac{k}{en_e}\int (\nabla T_e \times \nabla n_e)\, dt \ .$$

B. DENSITY/TEMPERATURE PROFILES

The mathematical density profiles used in pl2.c assume an initial gaussian radial distribution and an exponential axial distribution. Representation of the radial plasma density profile by a gaussian provided an easy and fairly accurate model. Axial density behavior was modeled by an exponential which provided a rather accurate representation of the shock front. Within 0.3 cm (the approximate shock thickness) the density rises from background density values (n_{bg}) of about 0.2 relative units to the measured results of about 15 relative units. A typical density profile fit to experimental data has the form:

$$n(r,z,t) = (n_{\max}(t) - n_{bg})(1 - e^{(z - z_o(t))/\delta_{zn}})\, e^{-r^2/\delta_{rn}^2} + n_{bg} \ , \qquad (30)$$

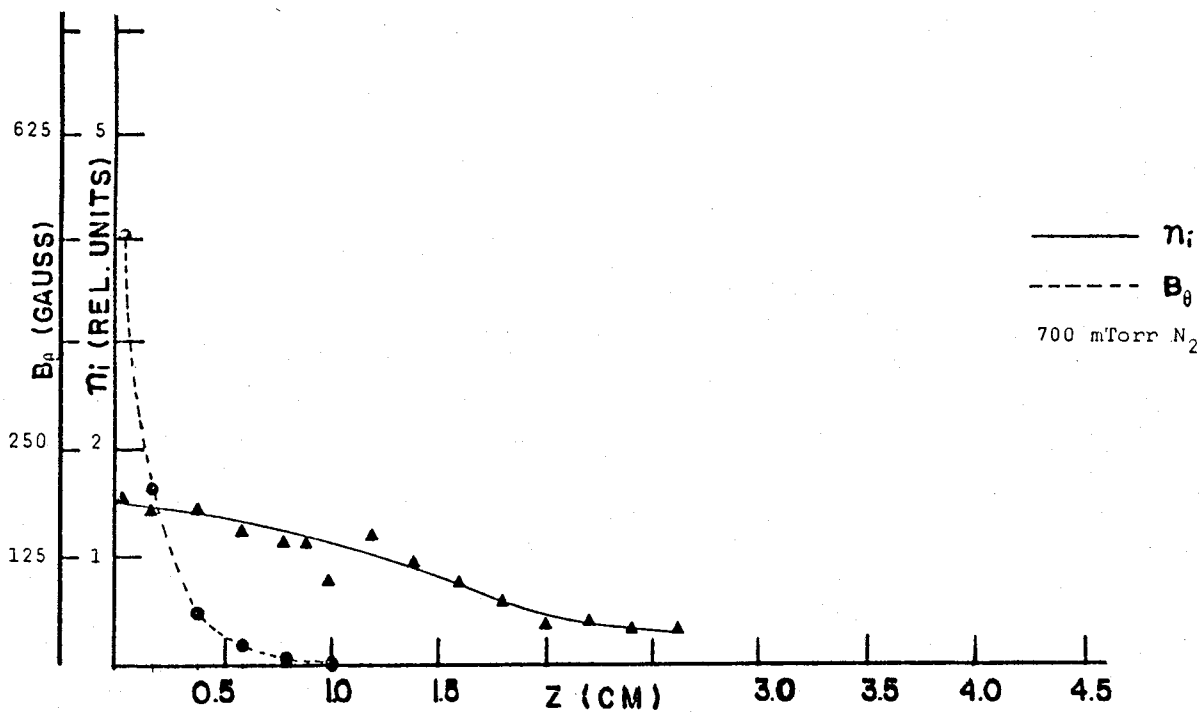

Figure 15a: B-Field and Density Data at 20 nsec in 700 mtorr N_2 along a line r=0.4 cm and $\theta = 0^o$. Solid line indicates plasma density. Dashed line indicates magnetic field magnitude. [Ref.2]

where $n_{max}(t)$ is a time dependent function that describes the maximum plasma density. $z_o(t)$ is also a time dependent function which describes the location of the plasma jet front. In pl2.c it is assumed that $z_o(t)$ is a linear function of time. That is, no accelerations of the jet front occur. The factor δ_{zn} in the exponent ensures that the shock front has a thickness of about 3 mm. Comparison with Bird's data in Figures 15a through 15h shows that the front thickness is such that the density increases to 90% of its maximum value within 5 mm. This observation was then used to determine the exponential axial constant of δ_{zn} = 0.25 cm. The gaussian factor describes

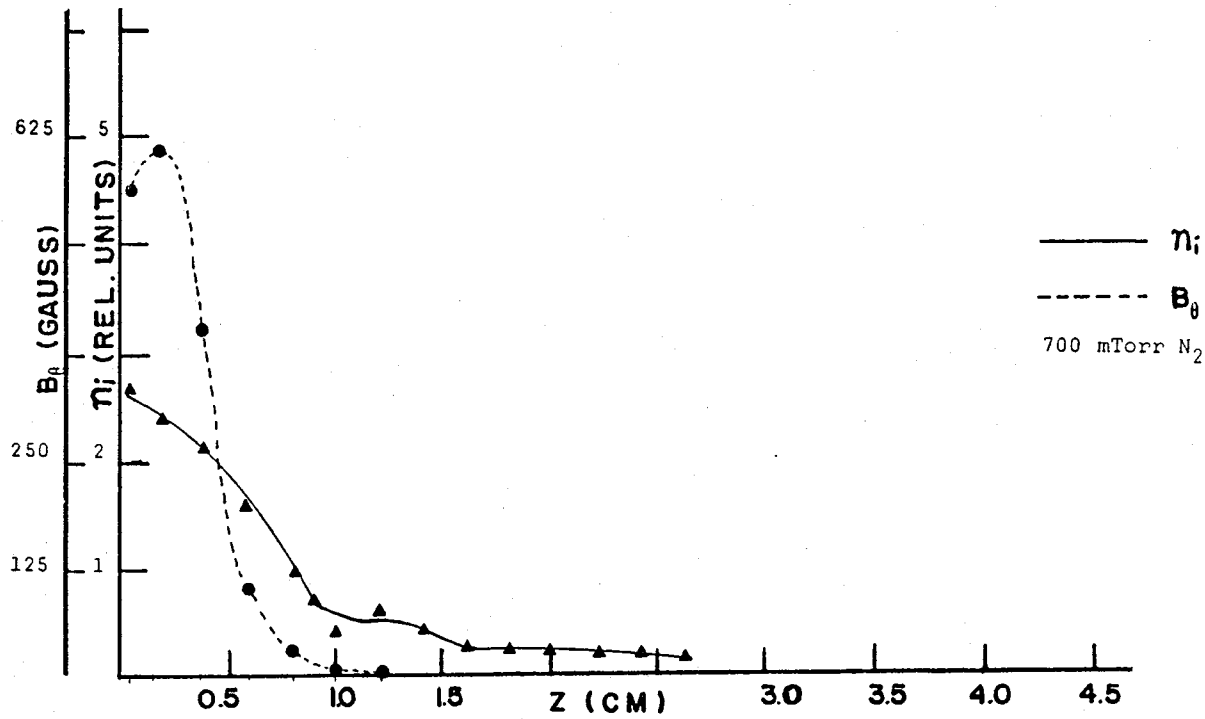

Figure 15b: B-Field and Density Data at 60 nsec in 700 mtorr N_2 along a line r=0.4 cm and $\theta = 0^o$. Solid line indicates plasma density. Dashed line indicates magnetic field magnitude. [Ref.2]

the radial behavior of the plasma. The factor δ_{rn} in the exponent indicates that at $r = \delta_{rn}$ cm, the density has fallen off by a factor of e^{-1} or 63%. It was assumed that the characteristic radial width of the density gradient δ_{rn} remained constant. This assumption is supported by Figures 9a and 9b. It is evident from these figures that the radial growth is minimal. The second term of equation (30) (n_{bg}= 0.2 r.u.) represents the background plasma density. A value of 0.2 relative units corresponds to about 6.4×10^{11} cm^{-3}. Figure 16 shows the experimentally measured relationship between the maximum jet density versus time. Notice that n_{max} versus time is fairly

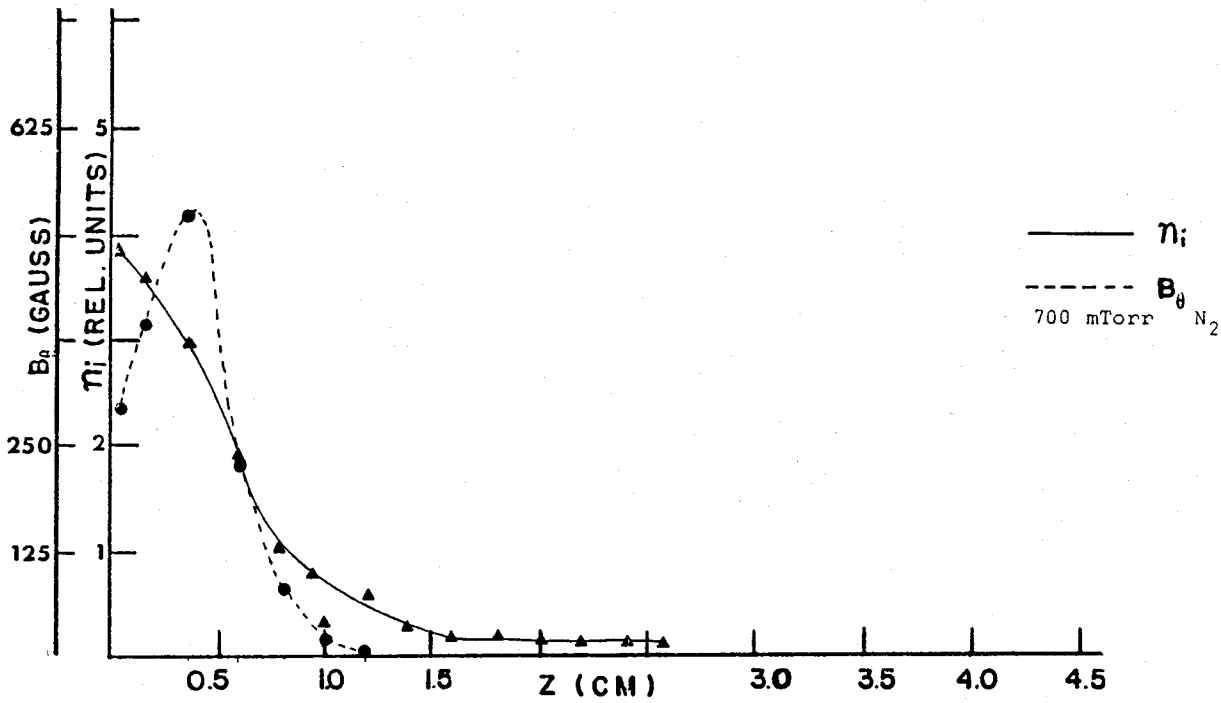

Figure 15c: B-Field and Density Data at 100 nsec in 700 mtorr N_2 along a line r=0.4 cm and $\theta = 0^o$. Solid line indicates plasma density. Dashed line indicates magnetic field magnitude. [Ref.2]

independent of background pressure. It is again important to notice that this data was taken at r=0.4 cm, $\theta = 0^o$. The plasma jet does not arrive at the measuring probe until some time between 200 nsec and 300 nsec. This is easily seen in Figure 16. Data for background pressures of 0.5 mtorr and 5 mtorr were only recorded until 300 nsec. This is because all relevant magnetic field activity had already decayed away at these lower pressures.

The functional dependence of n_{max} at r=0 was extrapolated. The mathematical form of $n_{max}(t)$ ensures that $n_{max}(300) = 15$ and $n_{max}(700) = 5$ which matches the extrapolated experimental data. $z_o(t)$ is assumed to be a

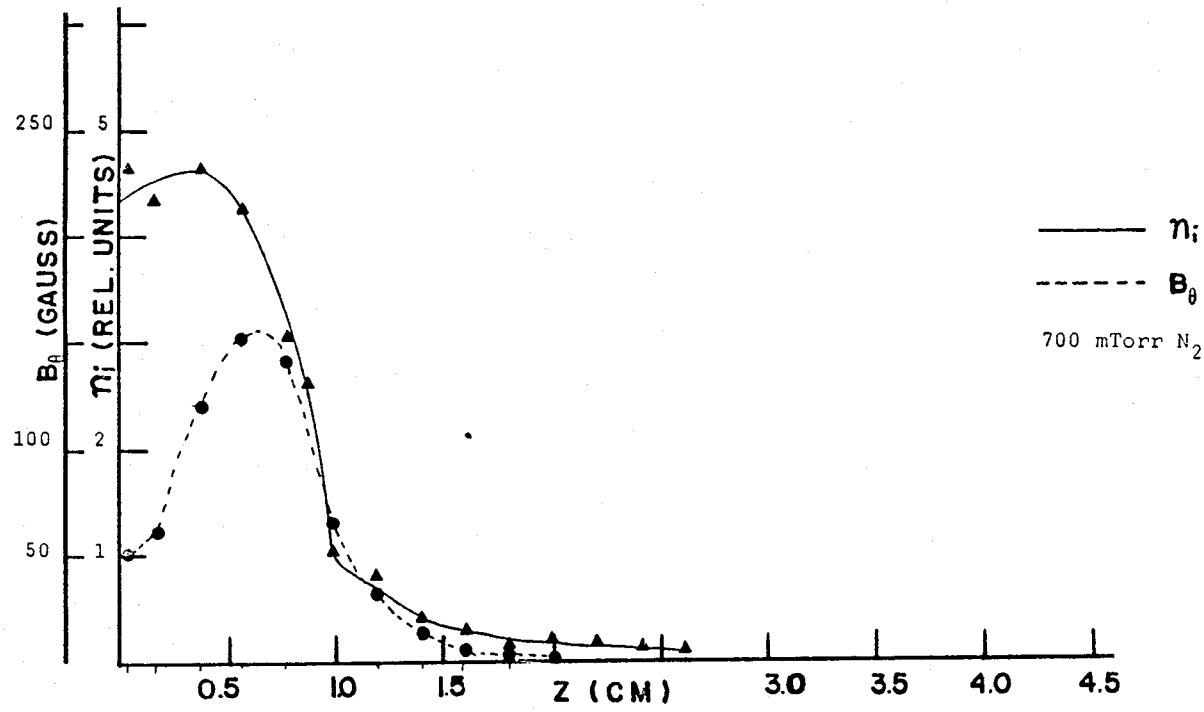

Figure 15d: B-Field and Density Data at 200 nsec in 700 mtorr N_2 along a line r=0.4 cm and $\theta = 0^o$. Solid line indicates plasma density. Dashed line indicates magnetic field magnitude. [Ref.2]

linear function of time. This is supported by Brooks' data shown in Figure 17. Plasma front velocity is a constant. At 700 mtorr N_2 background pressure, the jet velocity was about 3.1×10^6 cm/sec, hence $z_o(t)$ is given by:

$$z_o(t) = 3.1\times10^{-3} \text{ cm/nsec } t \ ,$$

where t is in nsec and z_o is in cm. In 1000 nsec the jet will propagate about 3.1 cm. The graphical representation of $n(r,z,t)$ is shown in Figure 18a.

The electron temperature is modeled by an equation very similar to equation (30). No experimental results exist which provide data on temperature distributions within the vicinity of the plasma jet, therefore it

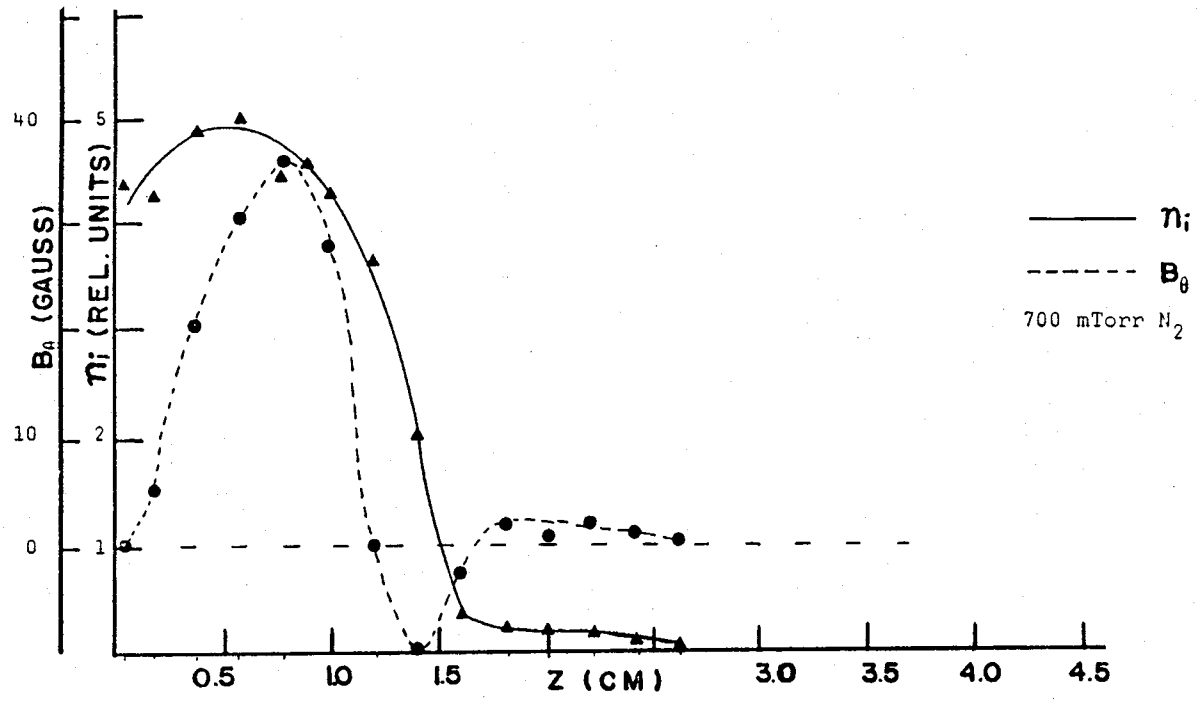

Figure 15e: B-Field and Density Data at 300 nsec in 700 mtorr N_2 along a line r=0.4 cm and $\theta = 0^o$. Solid line indicates plasma density. Dashed line indicates magnetic field magnitude. [Ref.2]

was assumed that the radial distribution was also a gaussian and that the axial distribution was exponential. Curvature of the plasma jet front implies that the centerline temperature of the jet is greater than the "off axis" temperature. This is due to the fact that shock heating occurs only to the fluid elements whose velocity components are normal to the shock front. An exponential axial distribution implies that the jet front not only provides a rapid rise in plasma density, but also in plasma temperature. Shock heating at the jet front generates this rise in electron temperature. A typical mathematical temperature profile (fit to numerical results) is given by:

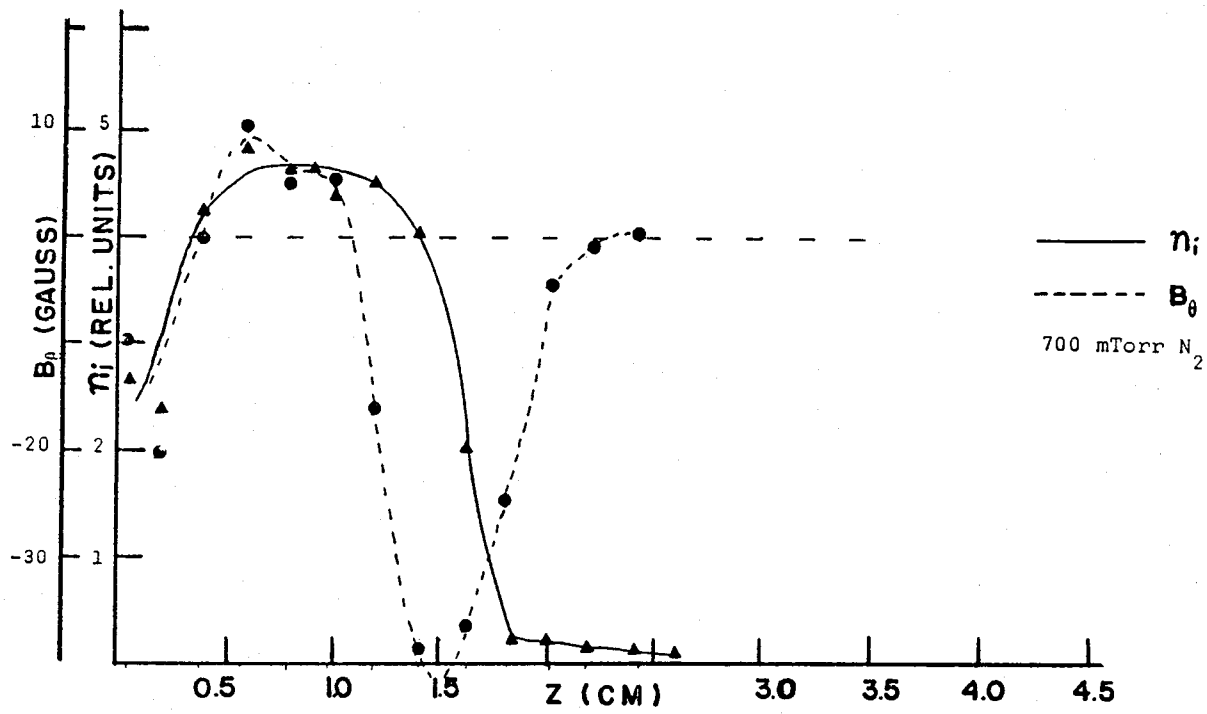

Figure 15f: B-Field and Density Data at 400 nsec in 700 mtorr N_2 along a line r=0.4 cm and $\theta = 0^o$. Solid line indicates plasma density. Dashed line indicates magnetic field magnitude. [Ref.2]

$$T(r,z,t) = (T_{\max} - T_{bg})(1 - e^{(z - z_o(t))/\delta_{zT}})\, e^{-r^2/\delta_{rT}^2(t)} + T_{bg}\ , \qquad (31)$$

where $T(r,z,t)$ and $T_{\max}$ are in eV, δ_{zT} = 1/3.99 cm, δ_{rT} is the characteristic radial width of the temperature gradient, and T_{bg} is the electron background temperature. The exponential factor (δ_{rT}) in the above expression for the temperature profile is not exactly equal to 0.25 cm (as in the case of the density profile) due to the effects of axial electron heat diffusion "pre-heating" incoming electrons. Since electron heat conduction occurs very rapidly, $\delta_{rT}(t)$ will not be a constant function of time. The mathematical form of $T(r,z,t)$ is shown in Figure 18b. Using the forms of

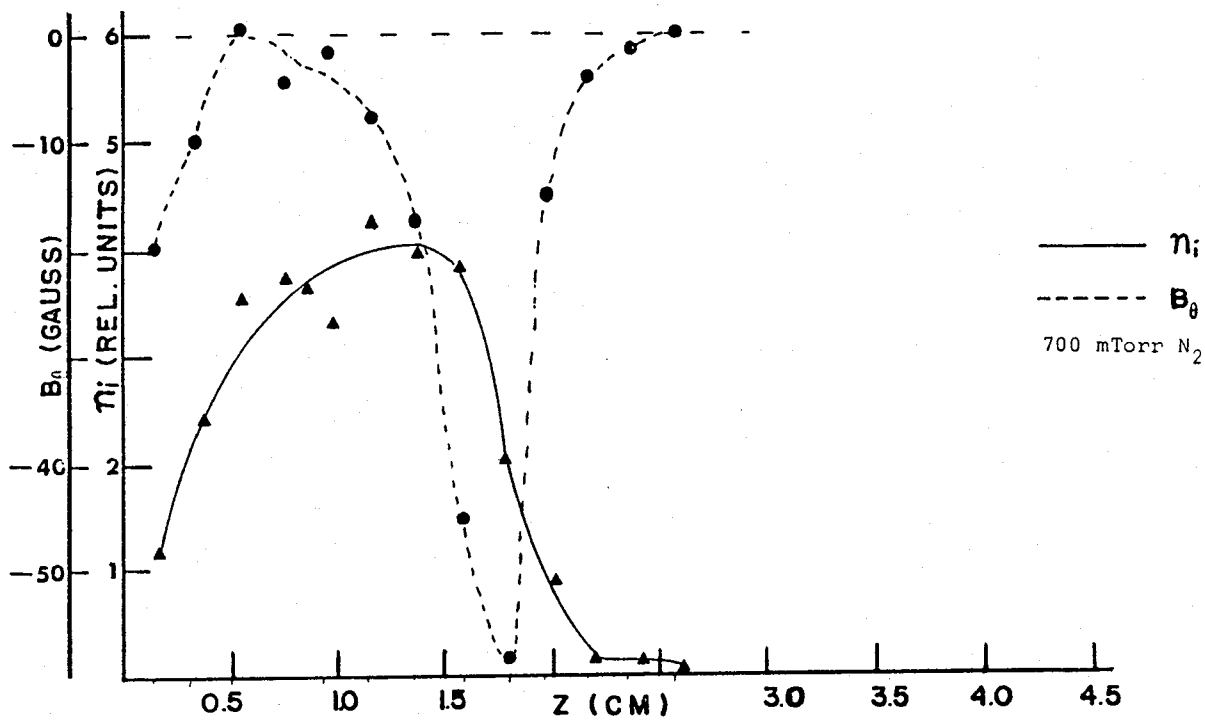

Figure 15g: B-Field and Density Data at 500 nsec in 700 mtorr N_2 along a line r=0.4 cm and $\theta = 0^o$. Solid line indicates plasma density. Dashed line indicates magnetic field magnitude. [Ref.2]

$T(r,z,t)$ and $n(r,z,t)$ given above, pl2.c solves the time integrated source equation (10). Magnetic field diffusion and convection are not calculated by pl2.c.

C. FINITE DIFFERENCE EQUATIONS

The pl2.c program simulates the production of magnetic flux due to the source term in equation (10). The source term is:

$$\frac{\partial \vec{B}}{\partial t} = \frac{k}{e}\nabla T_e \times \frac{1}{n_e}\nabla n_e = \frac{k}{en_e}\left[\frac{\partial T_e}{\partial z}\frac{\partial n_e}{\partial r} - \frac{\partial T_e}{\partial r}\frac{\partial n_e}{\partial z}\right]\hat{\theta}\,. \tag{32}$$

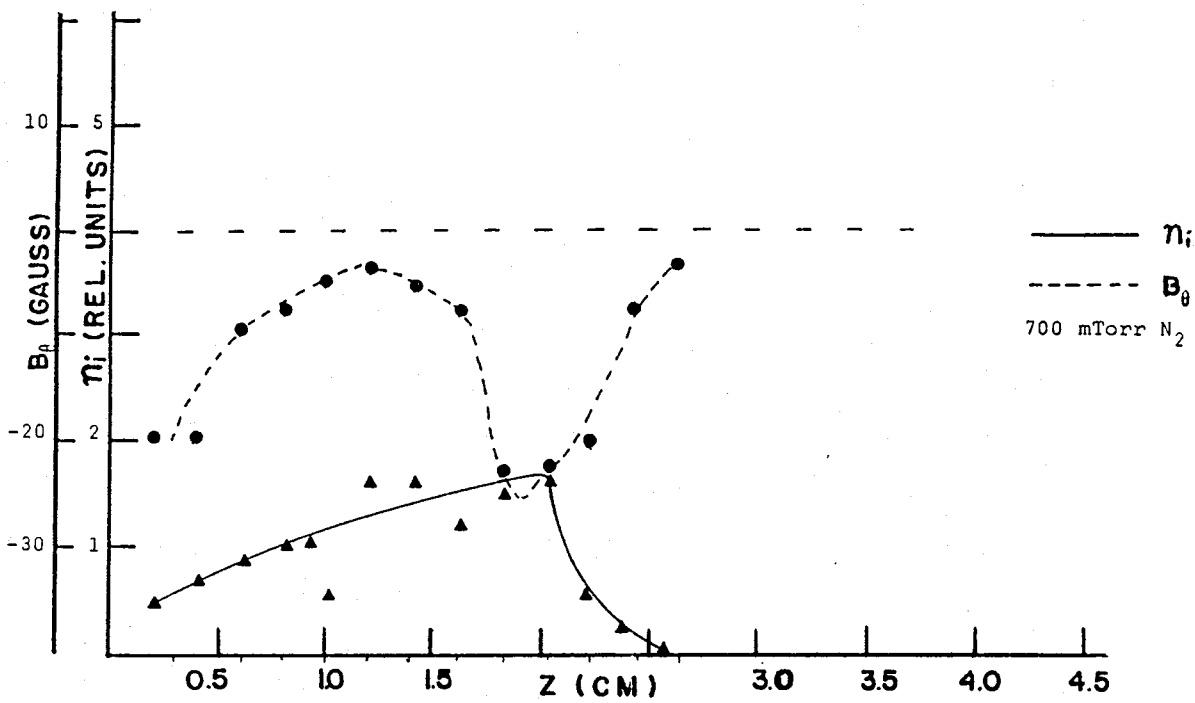

Figure 15h: B-Field and Density Data at 700 nsec in 700 mtorr N_2 along a line r=0.4 cm and $\theta = 0^o$. Solid line indicates plasma density. Dashed line indicates magnetic field magnitude. [Ref.2]

pl2.c performs a point by point time integration to determine the generated magnetic field at every spatial mesh point. Given that the plasma jet typically has dimensions of 1.5 cm in diameter and about 4 cm in length prior to dissipating, this region of space is divided into a 250 by 250 two-dimensional point grid. Each point on the grid is assigned a coordinate (z, r), a temperature $T(z,r)$, a density $n(z,r)$, and a magnetic field $B(z,r)$. The radial coordinate (r) varies from -1.5 cm to 1.5 cm. In grid coordinates, the radial coordinate is denoted by an integer j which varies from 0 to 250. The jet expands along the j=125 axis which corresponds to the r=0 cm axis.

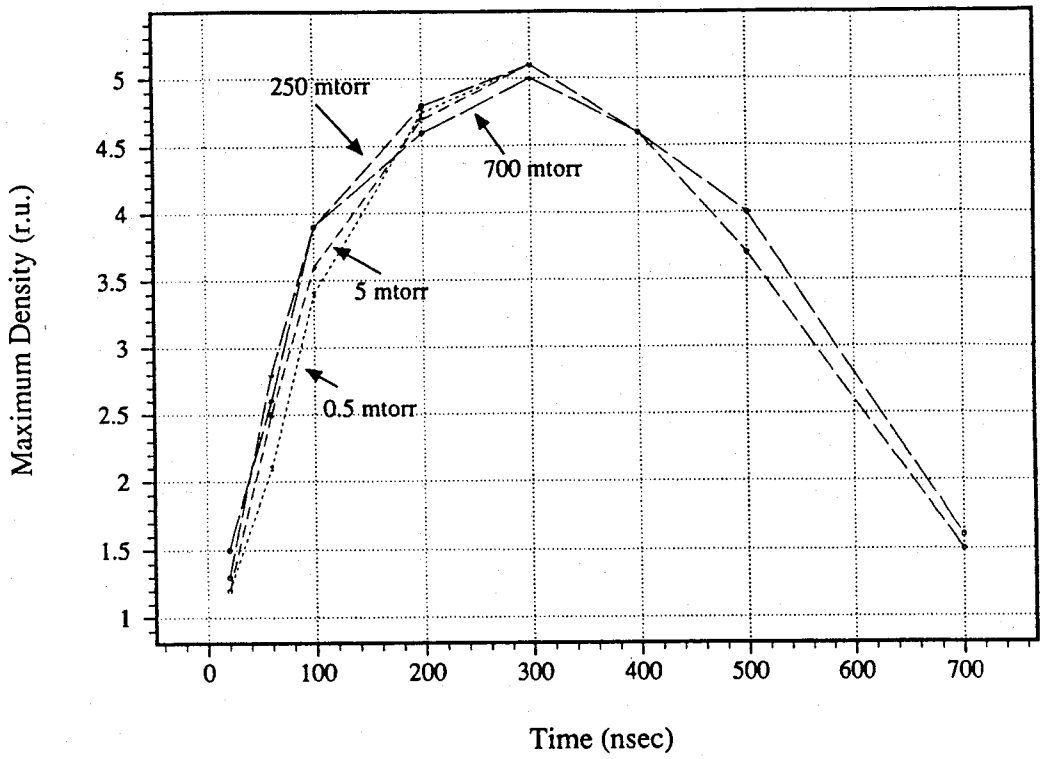

Figure 16: n_{max} versus Time (Experimental) at r=0.4 cm, $\theta = 0^o$. z varies depending on where the maximum density occurs.[Ref.2]

The axial coordinate (z) varies from 0 to twice the jet front expansion distance. That is, if the jet expands to 1.5 cm, then the grid varies from 0 to 3.0 cm. The axial grid coordinate is denoted by the integer i, and (as j) varies from 0 to 250. The grid coordinates then become (i, j) and the temperature and density profiles become point defined at each of these coordinates. Grid profiles are denoted by $T_{i,j}$, $n_{i,j}$, and $B_{i,j}$. In order to numerically calculate magnetic field growth at a point, equation (32) must be converted to a finite difference equation [Ref.12]. That is, it must be cast into a form which can be utilized by the computer. The partial derivatives in equation (32) at point (i, j) can be calculated in terms of the neighboring

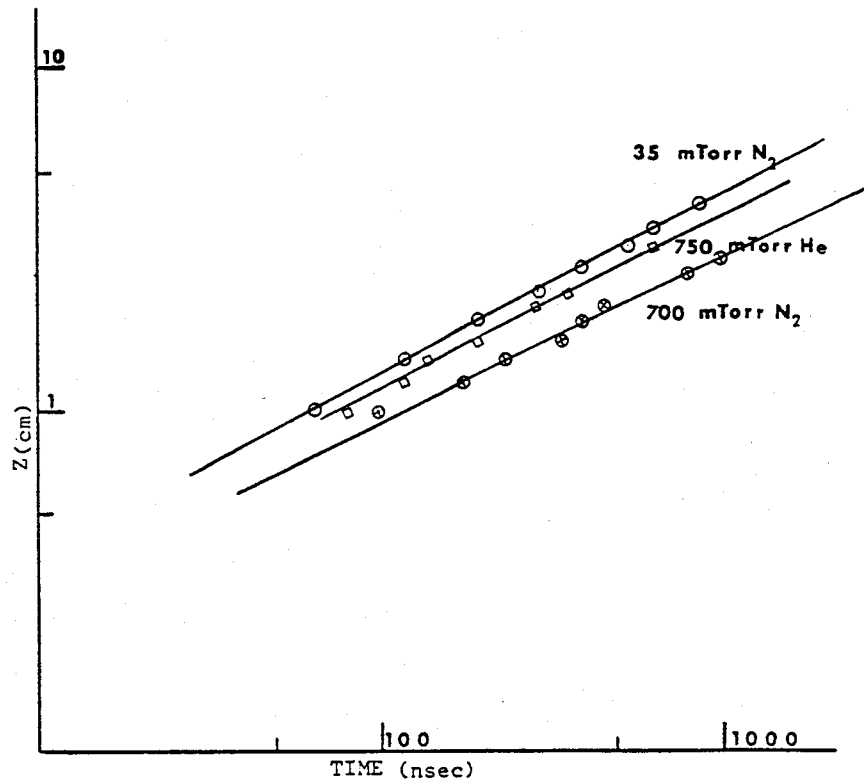

Figure 17: Plasma Jet Velocity. Position of the front of the plasma jet versus time for various background gas pressures. Data was taken along $r = 0$ cm with Langmuir double probe. [Ref.9]

grid points $(i+1, j)$, $(i, j+1)$, $(i-1, j)$, and $(i, j-1)$. The partial derivative of the electron temperature with respect to the axial coordinate $(\partial T_e/\partial z)$, for example, is written in terms of the finite difference equation as:

$$dTdz = \frac{T_{i+1,j} - T_{i-1,j}}{2dz},$$

where $dTdz$ denotes $\partial T_e/\partial z$, and dz is the finite distance between the grid points $(i+1, j)$ and $(i-1, j)$. In pl2.c: $dz = t1 / 250$ cm, where $t1$ is the distance in cm spanned by the 250 point axial grid. Since this distance depends on the integration time of the simulation, $t1 = 6.2\times10^{-3}\, t_{max}$. t_{max} is

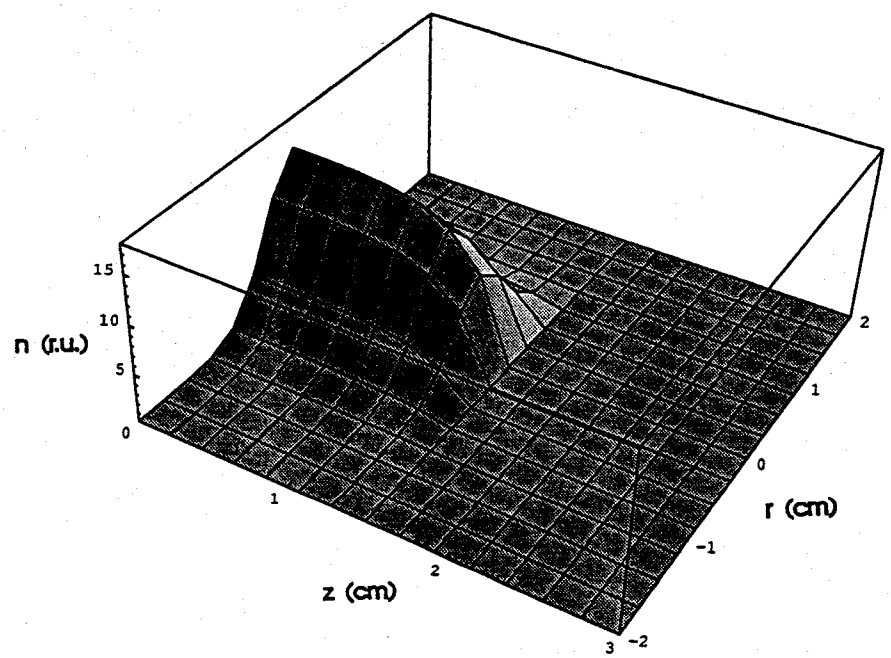

Figure 18a: Mathematical Density Profile, i.e. n(z,r,t). See equation 30.

the total time (in nsec) of the simulation. Notice that $t1$ corresponds to twice the jet expansion distance. The above finite difference equation essentially calculates the slope of the temperature grid in the z direction. Likewise:

$$dndz = \frac{n_{i+1,j} - n_{i-1,j}}{2dz} ,$$

$$dTdr = \frac{T_{i,j+1} - T_{i,j-1}}{2dr} ,$$

and:

$$dndr = \frac{n_{i,j+1} - n_{i,j-1}}{2dr} ,$$

where dr = 3/250 cm, since the total distance spanned in the radial direction is always 3 cm.

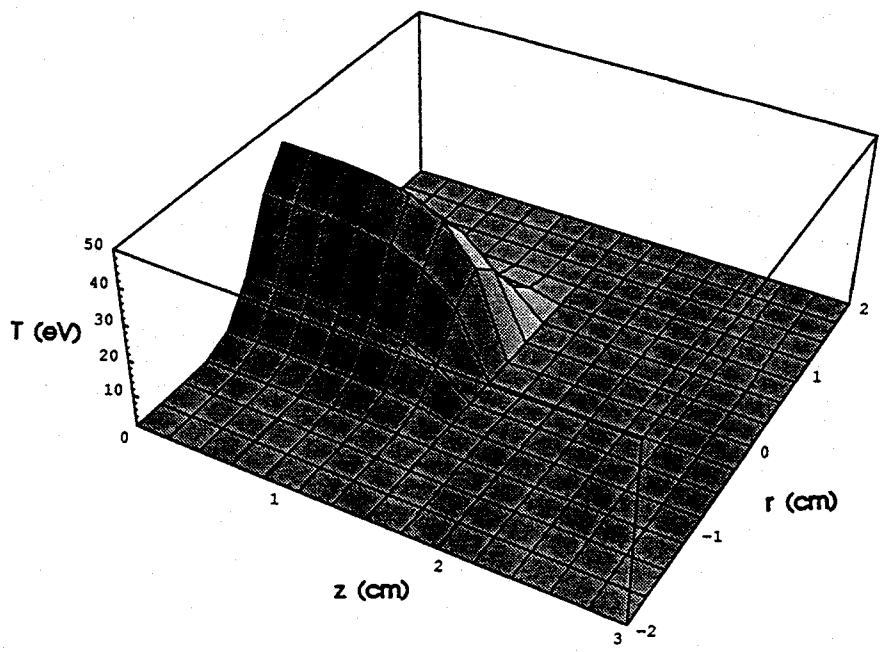

Figure 18b: Mathematical Temperature Profile, i.e. T(z,r,t). See equation 31.

For each time step (dt) the density and temperature gradients are calculated for each grid point with the equations given above. Once the partials are calculated, the magnetic field must be integrated at each grid point. That is, if equation (32) is written in finite difference form:

$$B_{i,j\ new} = B_{i,j\ old} + \frac{k}{en_{i,j}}\Big[(dTdz)(dndr) - (dTdr)(dndz)\Big]dt \ , \qquad (33)$$

then the magnetic field at (i, j) is incremented by the second term in the above equation. $B_{i,j\ old}$ represents the "old" value of the magnetic field at grid point (i, j) at time $t - dt$. The above expression is nested in a time loop, so that the last $B_{i,j\ new}$ becomes the present $B_{i,j\ old}$. The magnetic field throughout the grid is zero at t=0 nsec, and grows as the second term increments the previous time step value of $B_{i,j}$ by an expression related to

the density and temperature gradients. Since the total integration time is typically on the order of about 700 nsec, dt is chosen such that at least 1000 time steps are completed in order to calculate the magnetic field. For the simulations run by pl2.c, dt = 0.02 nsec. The experimental values of B, kT, time, and length are in units of Gauss, eV, nsec, and cm, respectively. In order for the calculated magnetic field to be in units of Gauss, temperature (kT) to be in units of eV, time to be in units of nsec, a conversion factor must be introduced to the second term to ensure the proper outcome of units. The density is expressed in relative units since the density units cancel out in the second term of equation (33). The conversion is:

$$\frac{(1.6\times10^{-19}\ \frac{\mathrm{J}}{\mathrm{eV}})\,(10^{-9}\ \frac{\mathrm{sec}}{\mathrm{nsec}})\,(10^{4}\ \frac{\mathrm{g}}{\mathrm{T}})}{(1.6\times10^{-19}\ \mathrm{C})\,(10^{-2}\ \frac{\mathrm{m}}{\mathrm{cm}})^{2}} = 10^{-1}\,.$$

Now equation (33) is written:

$$B_{i\,j\ new} = B_{i\,j\ old} + \frac{0.1}{n_{i\,j}}\left[(dTdz)(dndr) - (dTdr)(dndz)\right]dt\ .$$

This is the form of the source equation used in pl2.c. In pl2.c, the point functions $n_{i\,j}$, $T_{i\,j}$, and $B_{i\,j}$ are represented as two dimensional arrays denoted by n[nz][nr], T[nz][nr], and B[nz][nr], respectively. nz and nr are also integers ($0 \le nr \le 250$, $0 \le nz \le 250$) which represent the grid coordinates of a point in space.

In order to allow the jet to propagate away from the target surface, pl2.c propagates a "nulling" plane starting at the jet front (at t=0 nsec) and ending at the target surface at t=tmax. That is, the plasma jet is stationary and the "nulling" plane, which can be thought of as the target surface, propagates away from the plasma front. The jet frame of reference provides the same results as the laboratory frame. The jet frame, however, is a more convenient method to propagate the jet. This is simply an artifact of the

simulation and introduces no additional error into the analysis.

D. PL7.C

In order to achieve an understanding of the radial diffusion of the plasma density and temperature, pl7.c was written. pl7.c numerically solves the coupled partial differential equations describing temperature and density diffusion. As mentioned earlier, the radial density diffusion is modeled by classical particle diffusion. The radial temperature diffusion is modeled by a semi-empirically derived Bohm diffusion coefficient which describes diffusion across a magnetic field in a plasma which without a magnetic field would be collisionless. The Bohm diffusion coefficient (D_B) is given by equation (24) and is itself a function of electron temperature and the magnetic field present. Equation (25) represents the diffusion equation incorporating the Bohm coefficient as an upper bound. The classical particle diffusion coefficient, D, is a function of the ion collision frequency and ion mean free path (given by equation (29)). That is, it is also a function of temperature and density. Therefore, pl7.c solves the coupled, partial differential, diffusion equations (25) and (28).

pl7.c assumes axial and azimuthal symmetry and therefore reduces to a one dimensional simulation. Equations (25) and (28) are converted to finite difference form, yielding:

$$T_{new,j} = T_{old,j} + \frac{A\,(r_{j+1}(T_{j+1}\,T_{j+2} - T_{j+1}\,T_j) + r_{j-1}\,(T_{j-1}\,T_{j-2} - T_{j-1}\,T_j))\,dt}{4.0 r_j\,dr^2},$$

and

$$n_{new,j} = n_{old,j} + \frac{C\,(r_{j+1}\,(n_{j+2} - n_j) + r_{j-1}\,(n_{j-2} - n_j))\,dt}{4.0 r_j\,dr^2},$$

respectively. The integration constants A and C are given by,

$$A = \frac{6.25\times10^{-3}}{B} = \frac{1}{16B}\left[\frac{1}{1.6\times10^{-19}\ \mathrm{C}}\right]\left[\frac{10^4\mathrm{g}}{1\mathrm{T}}\right]\left[\frac{1.6\times10^{-19}\mathrm{J}}{1\mathrm{eV}}\right]\left[\frac{10^{-9}\mathrm{sec}}{1\ \mathrm{nsec}}\right]\left[\frac{100\mathrm{cm}}{1\mathrm{m}}\right]^2,$$

and

$$C = \frac{4.253\times10^{-5}\ T_j^{2.5}}{n_j},$$

where B is the magnetic field in Gauss and n_j is the particle density in r.u. The above finite difference equations are then integrated by the Euler-Cromer method. Values of the other constants are: dt=0.001 nsec and dr=3.0/125.0 cm. The initial temperature and density distributions are again assumed to be gaussian with their respective temperature and density widths, δ_{rT} and δ_{rn}, initially assumed to be equal. Initial and final total mass and energy are also calculated. In the early stages of programming, this was done to ensure simulation accuracy; however, at later stages this calculation was used to determine how much energy and mass was being introduced due to shock heating. Shock heating ensures that the internal jet temperature and density remain at shock determined values. Therefore, pl7.c maintains the temperature and density constant for the duration of the simulation out to a radius r=0.8325 δ_{rn} cm, where δ_{rn} in this case is the initial gradient width. This value of r is the ½ downpoint in density. Therefore, mass and energy are not conserved in the jet system due to shock heating. Once the time integration is complete, the simulation then calculates the ratio δ_{rT}/δ_{rn} which then can be compared with results provided by pl2.c.

V. SIMULATION RESULTS

A. INTRODUCTION

Simulations were run using the profiles given by equations (30) and (31), where

$$\delta_{zT} = 1/3.95 \text{ cm} ,$$

$$\delta_{zn} = 1/4.0 \text{ cm} ,$$

and,

$$n_{\max}(t) = 1.2315\times10^{-3} \text{ r.u. nsec}^{-2}\, t^2\, e^{-t/150 \text{ nsec}} . \tag{34}$$

The maximum density function ($n_{\max}(t)$) was obtained by fitting experimental data obtained by Bird. The experimental data of $n_{\max}(t)$ is shown in Figure 16. The modeled mathematical function $n_{\max}(t)$ is shown in Figure 19. The experimental data obtained by Bird was measured at r=0.4 cm. Since this is approximately the e^{-1} downpoint in density the measured values were multiplied by three, in order to extrapolate the density at r=0 cm. The experimental data for times earlier than about 200 nsec does not accurately represent true plasma jet conditions, since the jet has not arrived at the measuring probe. This inaccuracy was neglected in the initial simulations. In the end, modification of $n_{\max}(t)$ in the simulation proved to yield no new information, only faster magnetic field growth rates. All the "useful" physics was obtainable using the mathematical forms given above. The characteristic radial widths, δ_{rn} and δ_{rT}, were varied from 0.55 cm to 0.95 cm in order to observe the change in the simulated behavior. $T_{\max}$ was also investigated to find an estimate of the post-shock electron temperatures

required to obtain the observed magnetic fields. The characteristic widths of the axial gradients are fixed by the shock heating mechanism to be approximately 2-3 mm. The axial temperature gradient width (δ_{zT}) is slightly larger than the axial density gradient width (δ_{zn}) due to the high electron heat conduction rates. In essence, this causes electron pre-heating in front of the shock. Due to this difference, δ_{zn} will be referred to as the shock thickness.

Before going on, it should be noted that the magnitude of the shock generated field is astonishingly high in the simulations. The simulations, of course, assume no losses, when in fact many loss mechanisms exist. This chapter will present the simulated data and then attempt to provide some idea of the loss mechanisms involved. Comparison with experimental data will show that energy losses from the shock heated plasma are indeed significant.

First, the effect of differences in radial temperature and density diffusion will be discussed. It will be shown that as δ_{rT}/δ_{rn} increases, the generated magnetic field increases and the axial size of the generated field approach those observed in experiment. Second, the background temperature is assumed to be 1.0 eV. Since the plasma jet velocity is known from experiment, the maximum electron temperature due to shock heating ($T_{\max}$) is 43.6 eV. This high temperature, however, is above the dissociation and ionization potentials of N_2, N_2^+, N, and Al. This implies that only a small fraction of the energy produced in shock heating will be directed to heating electrons and creating gradients. Therefore, section C will examine how electron heating efficiency affects the shock generated magnetic fields. Third, the temporal behavior is examined. It will be shown that due to low electron heating efficiency and the neglect of field decay due to collisional losses, comparison of simulation and experiment in this respect is not good.

Finally, the field geometries are compared with experiment and the effects of axial electron pre-heating are analyzed.

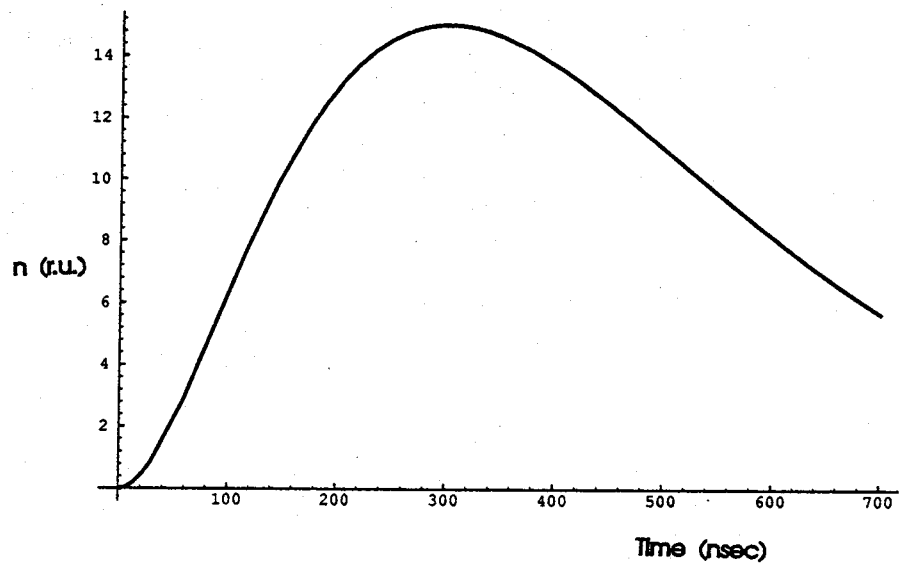

Figure 19: Mathematical Model for n_{max} vs. Time at r=0 cm, $\theta = 0^o$.

B. δ_{rT} / δ_{rn} BEHAVIOR

Figure 20 shows the results of studying the relationship between the maximum generated magnetic field at 400 nsec, and the characteristic radial temperature and density widths. As usual, positive magnetic fields represent shock generated fields.

The abscissa in Figure 20 represents the ratio of radial temperature width to radial density width. There are several features to notice about Figure 20. First, if $\delta_{rT} = \delta_{rn}$, then no shock generated fields are produced. This observation immediately supports the thesis that rapid electron heat conduction in the radial direction, in conjunction with shock heating at the

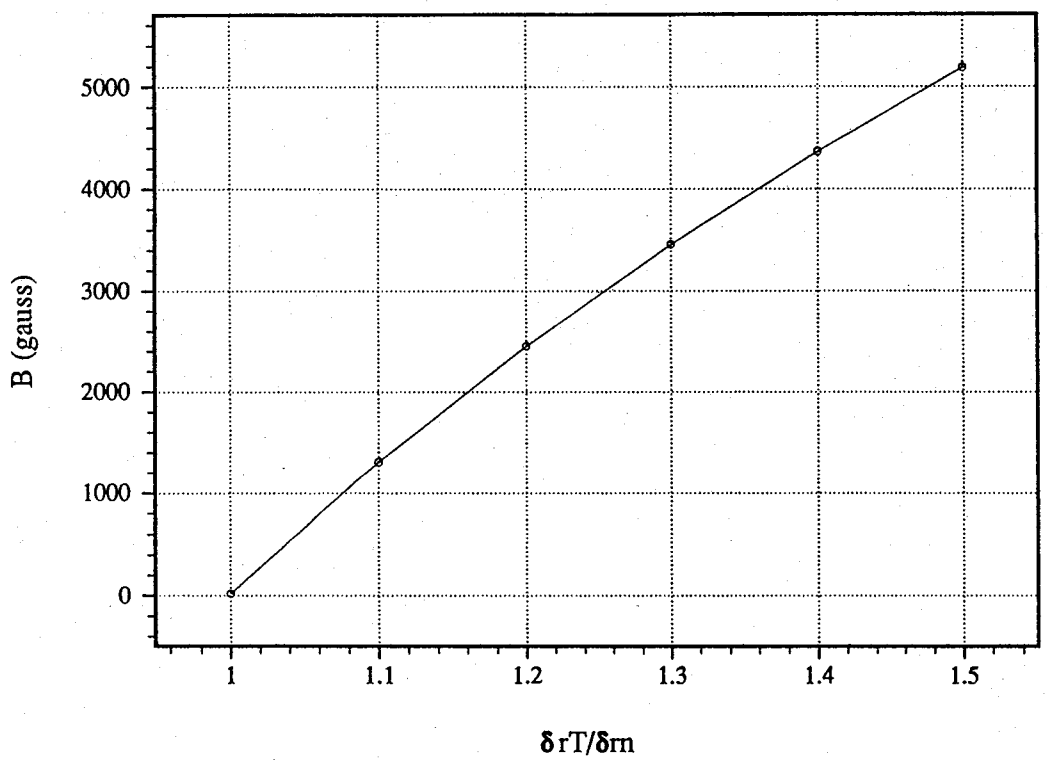

Figure 20: Generated Magnetic Field versus δ_{rT}/δ_{rn}. t=400 nsec, δ_{zn}=0.25 cm, δ_{zT}=1/3.95 cm, T_{bg}=1.0 eV, $T_{\max}$=43.597 eV, $n_{\max}$=15 r.u., and n_{bg}=0.1 r.u.. (δ_{zT}/δ_{zn}=1.01266).

front, produce field reversal. Therefore, $\delta_{rT} > \delta_{rn}$ is a fundamental requirement in achieving field reversal. Clearly, magnetic field generation is driven by radial heat conduction and axial shock heating. The curve in Figure 20 depicts a logarithmic relationship between B and δ_{rT}/δ_{rn} which can be written,

$$B\left[\frac{\delta_{rT}}{\delta_{rn}}\right] = 29345.7 \text{ Gauss } \log_{10}\left[\frac{\delta_{rT}}{\delta_{rn}}\right] + 21.95 \text{ Gauss} .$$

It should also be noted that the magnetic field is not an absolute function of the ratio δ_{rT}/δ_{rn}. As the radial size of the plasma jet (δ_{rn}) increases, for a

given δ_{rT}/δ_{rn}, the generated magnetic field decreases linearly.

As already alluded to in the theory chapter, if the shock forms in a background with no initial field (laser generated field) then the electrons are not magnetized. The collisionless electrons are free to flow away from the plasma jet to form an electric bi-layer in the background plasma. This fieldless mechanism produces an initially higher δ_{rT}/δ_{rn} and hence higher magnetic field.

Examination of the experimental data shows that the axial width of the generated magnetic field is about 0.5 cm. Figure 21 shows that when δ_{rT}/δ_{rn} >1.0, the generated field indeed approaches a constant value of about 0.46 ± 0.05 cm. The uncertainty in the measurement is mainly due to the subjectivity in measuring the field width from the computer output. When δ_{rT}/δ_{rn}=1.0, the field size is about 8.2 cm then as radial heat conduction occurs the field size quickly falls to observed values. This observation supports the existence of differences in the diffusion rates of temperature and density.

Varying maximum electron temperature did not affect the reversal thickness. δ_{rT} and δ_{rn} together with the degree of electron pre-heating, predict the axial dimensions of the reversal! This is remarkable since it is not immediately obvious that the axial dimension of the shock generated reversed field is independent of the maximum electron temperature. As the ratio δ_{rT} / δ_{rn} becomes larger, the reversed field axial width essentially remains constant at the experimentally observed value.

Simulation pl7.c was used to determine the magnitude of the ratio δ_{rT}/δ_{rn}. The following model was used in pl7.c to determine this ratio. As discussed earlier, the electron temperature diffusion is modeled by Bohm diffusion, which is a model that describes the energy transport across a magnetic field. As calculated earlier, the magnetic field is the dominant

mechanism present in determining electron motion. That is, the electron collision frequency and mean free path are are small enough to provide gyro motion of the electrons about the magnetic field lines. The electrons are inhibited from diffusing freely due to the presence of a magnetic field which modifies their motion. It is important to understand that ions are not restricted by the same mechanism. The ions have a much lower gyrofrequency, so that $\omega_c \tau|_i \ll 1$; hence, they are less inhibited by the presence of a magnetic field. Therefore, electrons (due to their lighter mass) diffuse their thermal energy through elastic collisions (in gyromagnetic orbits) with other electrons at a very high rate. Electron heat diffusion is an electron-electron collision dominated mechanism which is heavily dependent on the presence of a magnetic field.

Simulations show that within 50 nanoseconds δ_{rT}/δ_{rn}=1.13, and continues to grow for the remaining duration of the experiment. Figures 9a and 9b show the results of this simulation. One essential feature of pl7.c which must be noted is that between r=0 and the ½ downpoints in density and temperature, the profiles are maintained constant through the simulation. This is indicated in Figures 9a and 9b by vertical lines at approximately r=0.4 cm. This was done because in reality shock heating and compression maintain the temperature ($T_e(r)$) and density ($n_e(r)$) within the plasma jet as long as the jet Mach number remains constant, which is assumed to be the case. Only the normal component of velocity is shock heated, hence maximum heating and compression occurs along the centerline r=0 cm. The temperature and density within the plasma jet are functions of radius due to the curvature of the shock front. If the shock front holds the temperature and density constant to a radius beyond the ½ downpoint, then the ratio δ_{rT}/δ_{rn} will be correspondingly smaller.

The numbers ε_T and ε_n in Figures 9a and 9b give an indication of how much energy and mass must be added to the plasma jet via the shock process in order to maintain constant profiles of temperature and density within the jet. That is, by 50 nsec energy is increased by 15.1% to maintain constant temperature and mass is increased by 13.0% to maintain constant density. These increases must be made to offset losses by diffusion.

Simulations show that the ratio δ_{rT}/δ_{rn} increases when the following parameters increase; maximum electron temperature and maximum electron density. The ratio δ_{rT}/δ_{rn} decreases when the background electron temperature and density increase.

Given that $T_{e,max}$=43.6 eV, T_{bg}=1.0 eV, $n_{e,max}$=15.0 r.u., and n_{bg}=0.1 r.u.; Figure 22 shows the growth of δ_{rT}/δ_{rn} as a function of time. At 0.5 nsec, δ_{rT}/δ_{rn}=1.0. Notice that the slope is fairly steep up to about 100 nsec, and then decreases. This indicates that electron temperature diffusion rate within the first 100 nsec is fast and then slows at later times. This may be explained by the fact that the electrons become de-magnetized outside of r=1.1 cm. Beyond this range the electrons also propagate at their respective thermal velocity. At 700 nsec, δ_{rT}/δ_{rn}=1.31. Again these values depend on the range to which the shock holds the temperature and density constant within the jet.

C. T_e max BEHAVIOR

Maximum electron temperature in the expanding laser plasma is determined by the Mach number of the shock. Figure 2 shows that at large Mach numbers (M_1>2.4) the shock heating mechanism becomes significant. Maximum electron temperatures on the order of 40 eV are not uncommon, depending on the initial background electron temperature. pl2.c was used to analyze the effect of maximum electron temperature on the self-generated

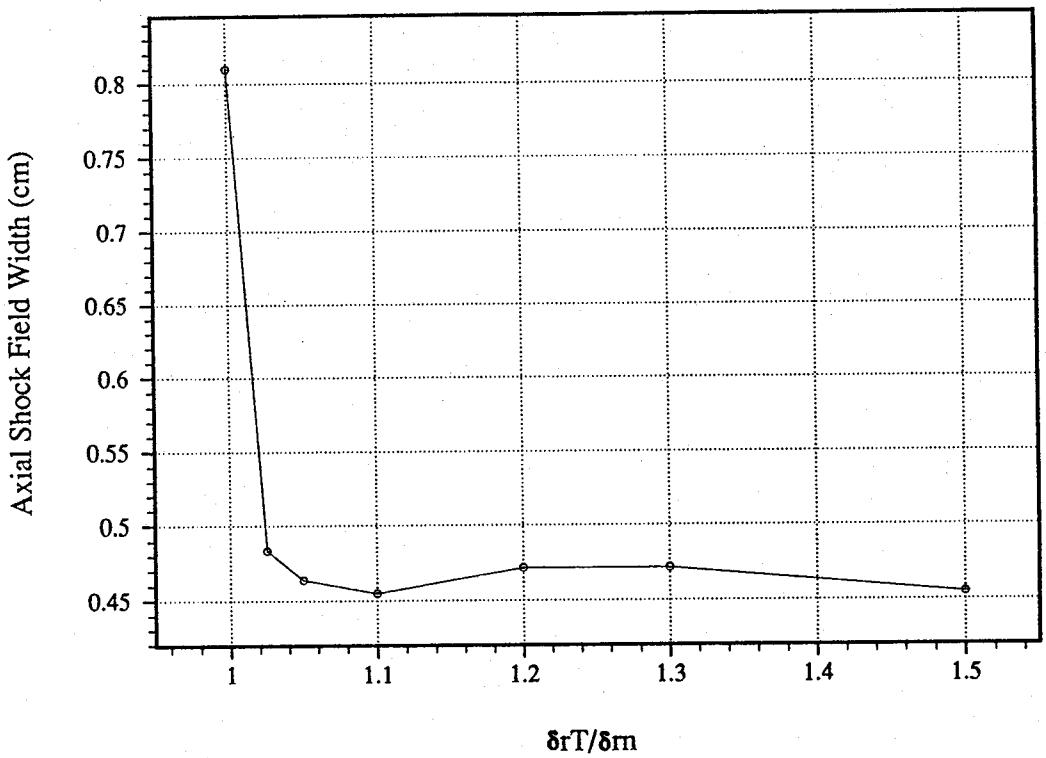

Figure 21: Axial Thickness of Reversed Shock-Generated Magnetic Field versus δ_{rT}/δ_{rn}. For δ_{zT}/δ_{zn}=1.01266, δ_{zn}=0.25 cm, T_{max}=43.6 eV, T_{bg}=1 eV, n_{max}=15 r.u., and n_{bg}=0.1 r.u..

magnetic field. Figure 23 shows the result of investigating the response of the generated magnetic field to changes in electron temperature. The background temperature was assumed to be 1.0 eV, the elapsed integration time was 400 nsec, δ_{rT} = 0.605 cm, and δ_{rn} = 0.55 cm ($\delta_{rT}/\delta_{rn} \approx 1.1$). δ_{rT} was allowed to be greater than δ_{rn}, so that the affect on the reversed field could be studied. As will be discussed in the next section, not all energy in the shock heating process is used to heat electrons. Ideally (for a given Mach number) the temperature behind the shock would be 43.597 eV. However, the laser and background plasmas have several excitation, ionization and

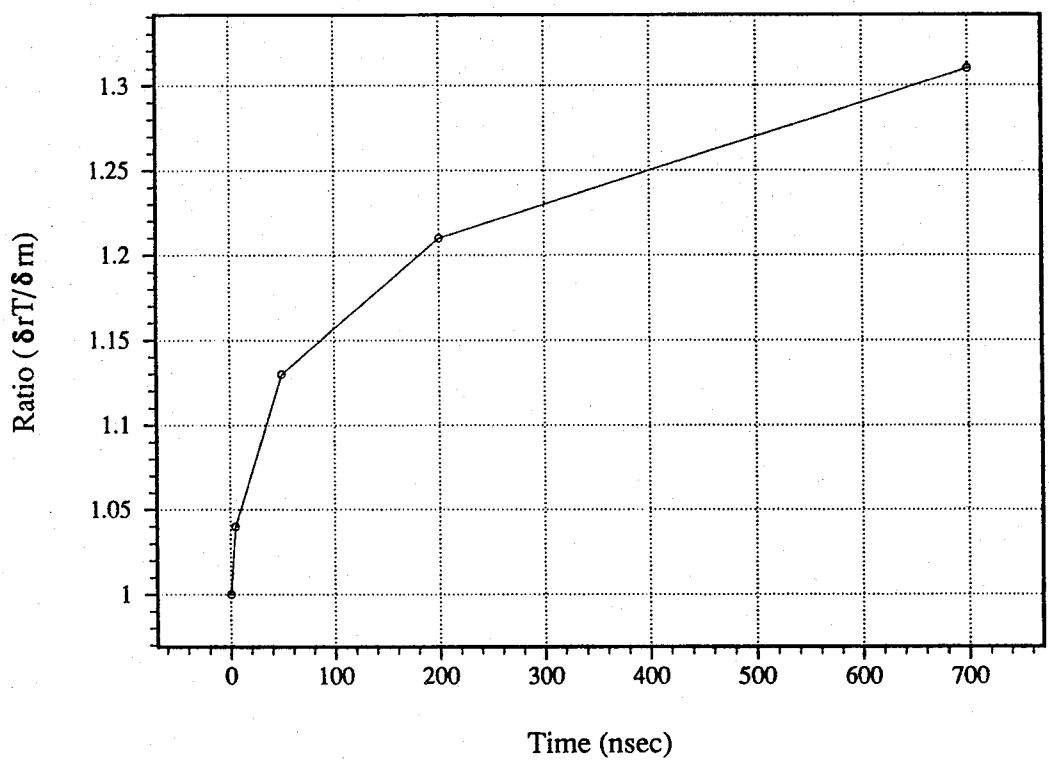

Figure 22: δ_{rT}/δ_{rn} versus Time in nanoseconds. Assuming $T_{e,max}$=43.6 eV, T_{bg}=1.0 eV, $n_{e,max}$=15 r.u., and n_{bg}=0.1 r.u. This simulated data was produced by pl7.c.

dissociation potentials which lie below this maximum theoretical temperature. Therefore, in reality, only a small fraction of the energy released during shock heating shows up as an electron temperature increase. This inefficiency reduces the observed magnetic field. Figure 23 shows the results of simulating various degrees of inefficient electron heating. The abscissa indicates the fraction of the shock heating energy which actually gets used to increase the electron temperature. The ordinate indicates the fraction of the magnetic field produced relative to no energy losses. If it is assumed that about 10% of the energy made available by

shock heating is used to heat electrons, then Figure 23 shows that the magnetic field generated for this case would be about 8% of the total no loss magnetic field. Assuming the background temperature to be 1.0 eV, maximum temperature to be 43.597 eV, background density to be 0.2 r.u., maximum density to be 15 r.u., $\delta_{rT}/\delta_{rn}=1.07$, and $\delta_{zT}/\delta_{zn}=1.01266$; simulations show that the magnetic field produced was 910 Gauss. Accounting for 92% energy losses yields 82 Gauss. It should be noted that this analysis does not account for the ohmic losses in the plasma which are described by the first term in equation (10). The maximum observed shock generated field in experiment at this background pressure (700 mtorr) was about 60 Gauss (see Figures 15). Therefore (with the exception of ohmic losses), 90% ionization, excitation, and dissociation losses do well in reconciling the lossless shock magnetic fields simulated by pl2.c with those seen in experiment.

It should also be noted that shock field generation occurred even when the generated electron temperature corresponded to a jet Mach number below 2.4. This result leads to the conclusion that strong shock fronts (M_1>2.4) are not necessary in creating shock field phenomena. However, large Mach numbers do provide for larger shock field growth rates. In actuality, resistivity losses cause the shock-generated magnetic fields to decay exponentially, as observed by McKee [Ref.1].

D. TEMPORAL BEHAVIOR

The temporal dependence of the self-generated magnetic field was studied yielding Figure 24. Initially, during the time frame when the laser is still irradiating the target ($t \approx 20$ nsec), $\delta_{rT} \approx \delta_{rn}$ and $\delta_{zT} \gg \delta_{zn}$. Shortly after laser heating has begun, however, electron heat conduction causes the temperature gradients to relax faster than the density gradients. Also

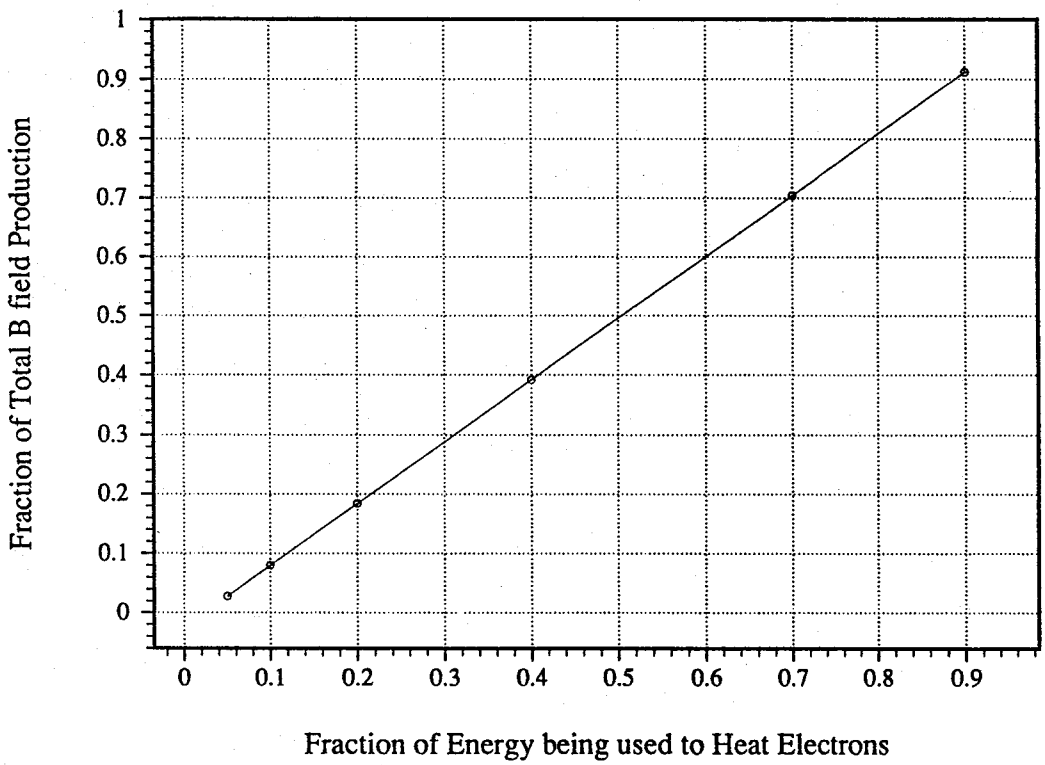

Figure 23: Fraction of Total Magnetic Field Produced versus Fraction of Energy being used for Electron Shock Heating (as opposed to ionizations and dissociations). For δ_{rT}/δ_{rn}=1.1, δ_{zT}/δ_{zn}=1.01266, δ_{rn}=0.5477 cm, δ_{zn}=0.25 cm, $T_{\max}$=43.6 eV, T_{bg}=1.0 eV, $n_{\max}$=15 r.u., n_{bg}=0.1 r.u..

within 50 nsec after cessation of the laser pulse, a shock front forms. When this occurs, $\delta_{rT}>\delta_{rn}$ and $\delta_{zT}>\delta_{zn}$. The former inequality is due to radial heat conduction, while the latter inequality is due to axial electron pre-heating. As this condition occurs, shock fields are generated. Figure 24 shows that the magnetic field increases linearly with time. The following parameters were used to derive Figure 24: δ_{rT}=0.55 cm, δ_{rT}/δ_{rn}=1.1, δ_{zn}=0.25 cm, and δ_{zT}/δ_{zn}=1.01266. A linear fit to simulated data shows:

$$B(t) = 3.6 \text{ Gauss nsec}^{-1}\, t - 123.8 \text{ Gauss},$$

where t is measured in nanoseconds, and B is in Gauss. This fit is valid between 50 nsec and 700 nsec. Of course, the rate of magnetic field production is dependent on δ_{rT}/δ_{rn}, which has already been discussed; it is also dependent on the amount of electron pre-heating and the shock thickness. This dependence will be discussed in section F of this chapter. Comparing this temporal behavior with experiment (Figure 24) does not show a good agreement. This can be attributed to the following reasons. First, the simulation only accounts for field production by temperature and density gradients and neglects any effects due to field diffusion (ohmic losses). Second, not all of the energy converted from kinetic to thermal in the shock process is converted to an increase in plasma electron temperature. Since the shock temperature is about 43 eV, excitation, ionization, and dissociation of the nitrogen background and the plasma jet occurs. The energy used for ionizations and dissociations is not available for increases in electron temperature; thus the effective increase in electron temperature due to shock heating is smaller than that predicted solely by lossless shock theory. Smaller gradients result and, hence, smaller fields are generated. Figure 25 shows the experimental temporal behavior compiled from Bird's data.[Ref.2]

Comparing the 700 mtorr background pressure to 5 mtorr pressure shows that the maximum initial magnetic field for the 700 mtorr case (solid line) decays away much more quickly than does the 5 mtorr case (short dashed line). This is because at 700 mtorr, shock heating causes reversal to occur, which acts to "cancel" the initial field rapidly when compared to other decay mechanisms such as collisional losses. At 5 mtorr, only the conventional loss mechanisms act, so that field decay occurs more slowly. Figure 25 also shows that shock heating begins to occur at a time between

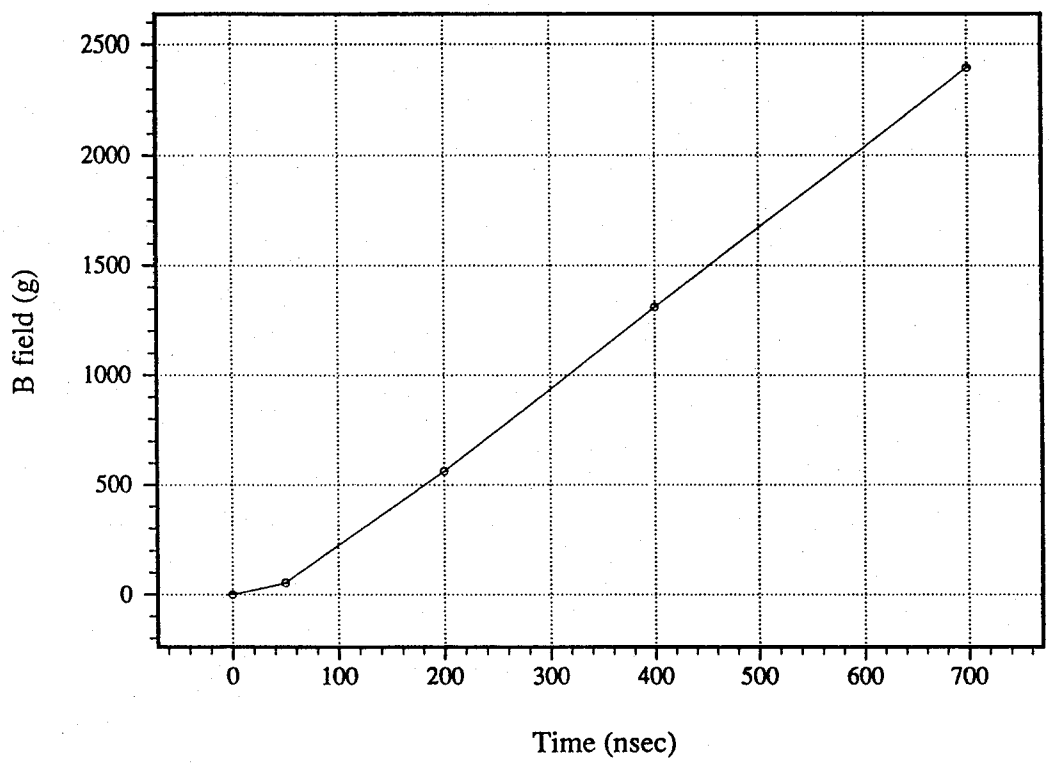

Figure 24: Shock-Generated Magnetic Field versus Time (nsec). (Simulation). For δ_{zT}/δ_{zn}=1.01266, δ_{zn}=0.25 cm, δ_{rT}/δ_{rn}=1.1, δ_{rn}=0.5477 cm, T_{max}=43.6 eV, T_{bg}=1.0 eV, n_{max}=15 r.u., n_{bg}=0.1 r.u..

30 nsec and 100 nsec, since the relative peaks at about 50 nsec are unaffected by this mechanism. Shock generated magnetic fields (in 700 mtorr) are not detected until 300 nsec (broad dashed line B<0 Gauss). Therefore it takes approximately 200 nsec to algebraically "cancel" the laser self-generated magnetic field. Due to the background interactions discussed earlier, the peak magnetic field in 700 mtorr is expected to be higher than the peak field in 5 mtorr.

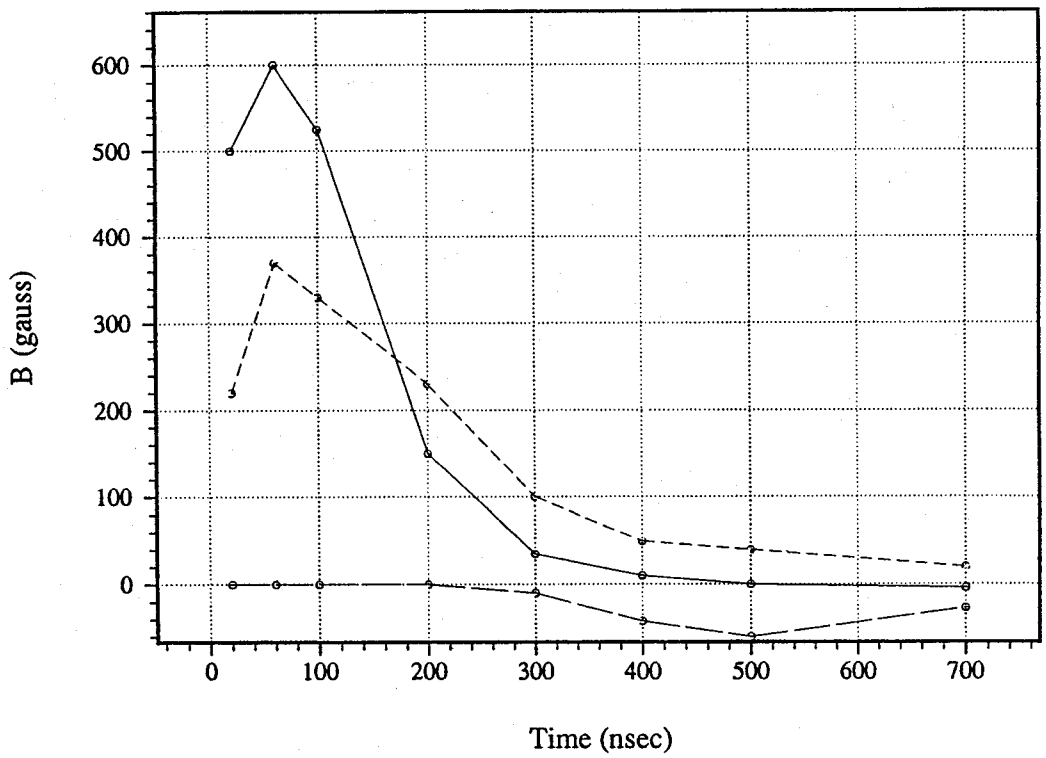

Figure 25: Self-Generated Magnetic Field versus Time (nsec). (Experiment) Solid Line indicates 700 mtorr, Short Dashed Line indicates 5 mtorr, and the Broad Dashed Line indicates the shock generated field at 700 mtorr. Data for 5 mtorr is extrapolated beyond 300 nsec. [Ref.2]

E. FIELD GEOMETRIES

The evolution of the shock generated magnetic field (simulated by pl2.c) is shown in Figures 26a through 26f. These runs were completed at 50 nsec increments. The profiles used are given by equations (30) and (31), which represent a background pressure of 700 mtorr. The characteristic gradient widths, δ_{rT} and δ_{rn}, were assumed to be constant at δ_{rT}/δ_{rn}=1.07, δ_{rn}=0.55 cm. In reality, shock heating and field reversal would not occur until a shock has formed. This occurs at some time between 30 nsec

(cessation of laser) and 100 nsec (first detectable evidence of field reversal in experiment). The times represented in Figures 26 are relative to when the shock formed, not when the laser irradiation began. The laser generated magnetic fields (which by themselves are not of interest in this thesis) have been neglected in the simulation (pl2.c) since diffusion of these fields for times greater than 30 nsec could not be taken into account. Therefore, Figures 26 only show the evolution of the shock generated fields. Once a shock has formed, $\delta_{rT} > \delta_{rm}$, and reversal begins. In Figures 26a through 26f, max T_e denotes maximum electron temperature in the jet, Bmax and Bmin indicate the maximum and minimum magnetic field strengths along a line at r, dt is the numerical time increment to ensure sufficient time steps are taken during the integration process, and Z_o is the location of the jet front. The upper window represents a two-dimensional intensity plot of the magnetic field, while the lower window represents a graph of magnetic field strength versus axial distance along a line at r, where r is given at the right in each figure. As usual, positive field values indicate shock fields. It should also be mentioned that the scales of the abscissa and ordinate for each of the curves in Figures 26 change. Therefore, the apparent steepening of the magnetic field profiles with time is only a manifestation of the scale used. The magnetic field, however, does exhibit the maximum growth rate at the plasma jet tip.

Figures 27a through 27e show experimentally obtained magnetic field contours at 250 mtorr N_2. At 250 mtorr, field reversal begins at about 300 nsec. At 700 nsec the reversed field has completely cancelled the initial field component. It would have been preferable to compare experimental data taken at 700 mtorr N_2, but 250 mtorr was the highest background pressure where B-field contour data was available.

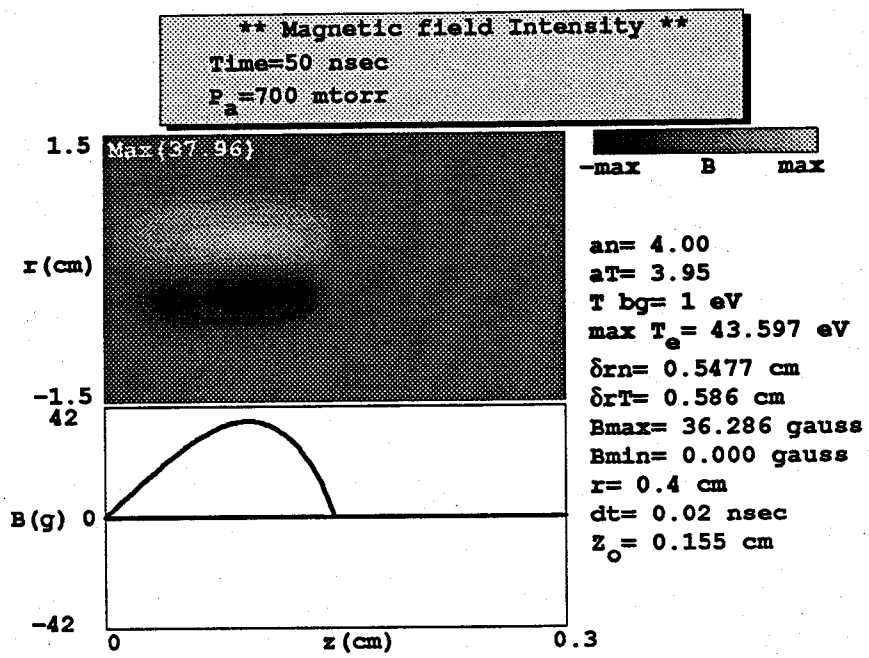

Figure 26a: Simulated Magnetic Field Contours at 50 nsec.

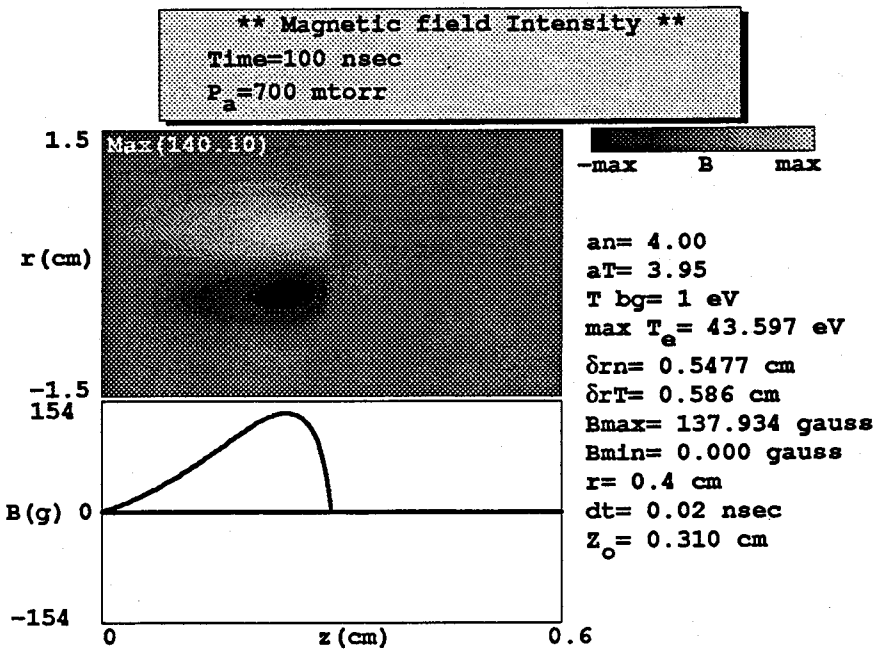

Figure 26b: Simulated Magnetic Field Contours at 100 nsec.

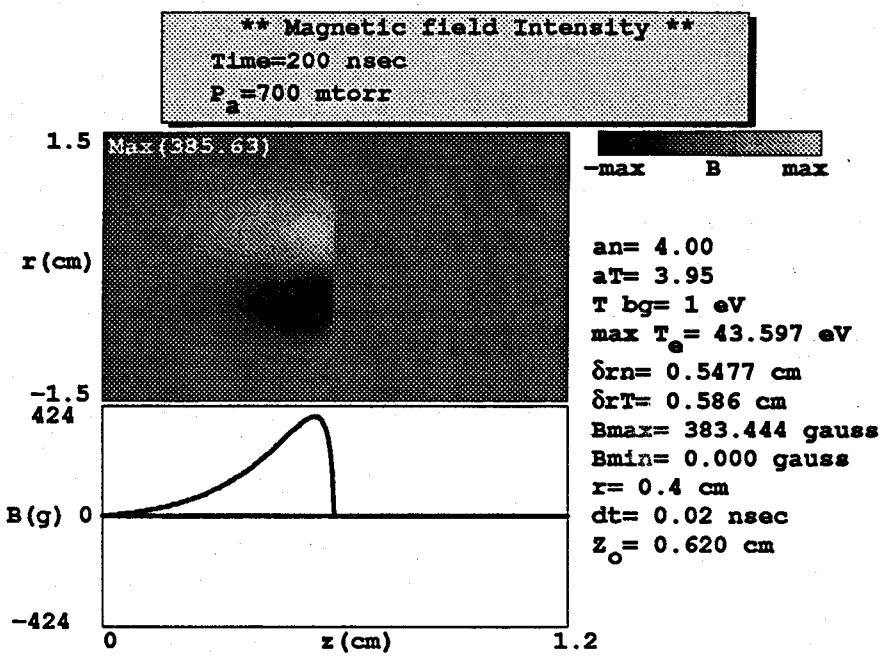

Figure 26c: Simulated Magnetic Field Contours at 200 nsec.

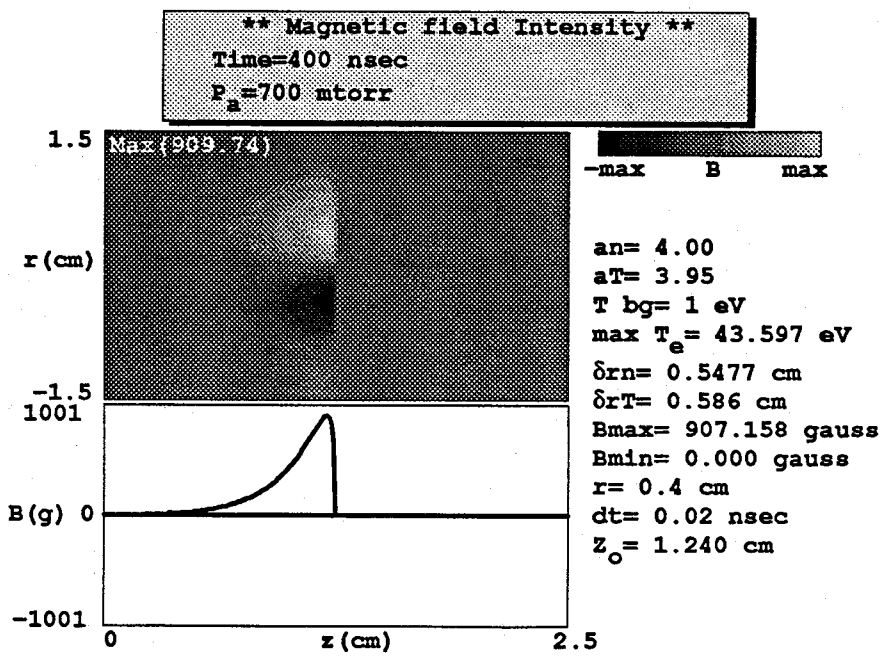

Figure 26d: Simulated Magnetic Field Contours at 400 nsec.

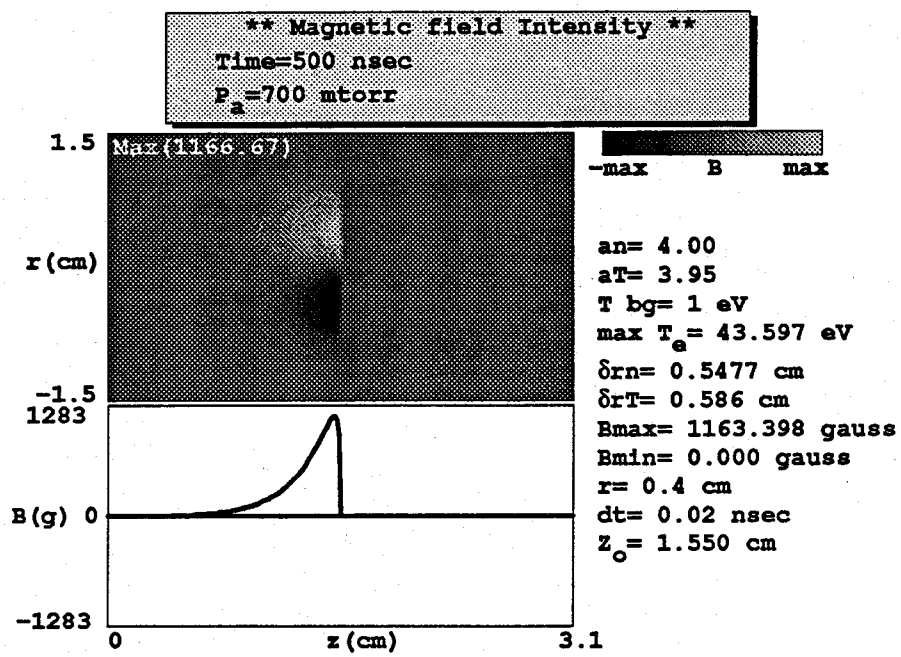

Figure 26e: Simulated Magnetic Field Contours at 500 nsec.

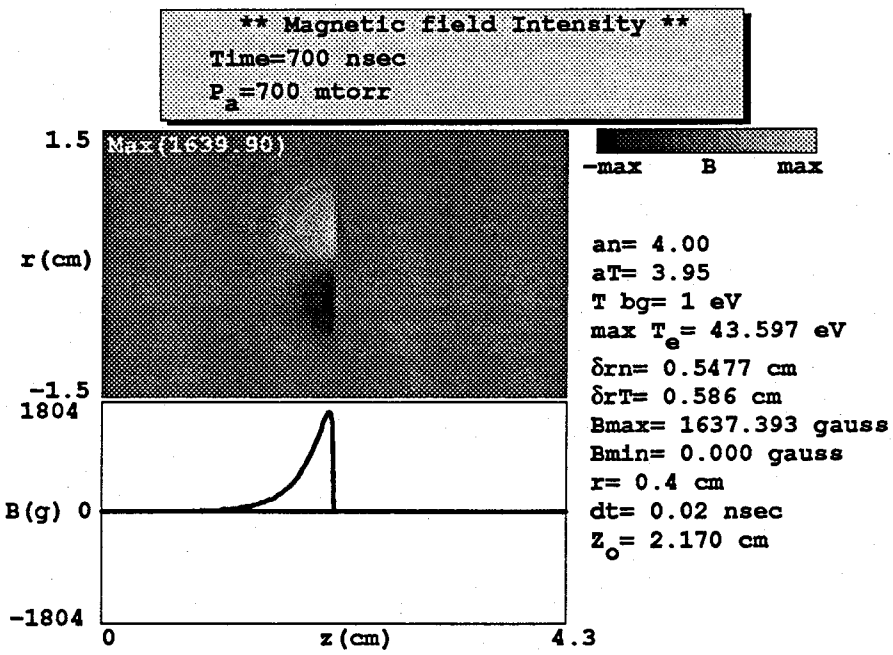

Figure 26f: Simulated Magnetic Field Contours at 700 nsec.

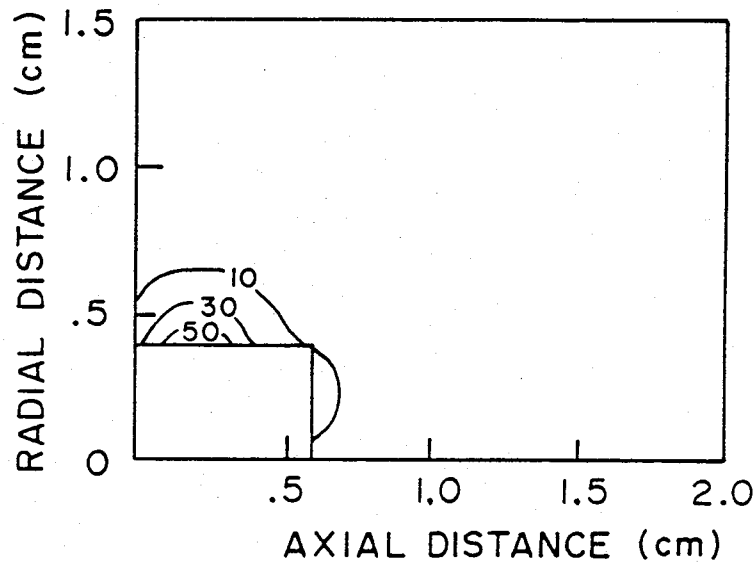

Figure 27a: Experimental Magnetic Field Contours at 0 nsec in 250 mtorr N_2 background.[Ref.1]

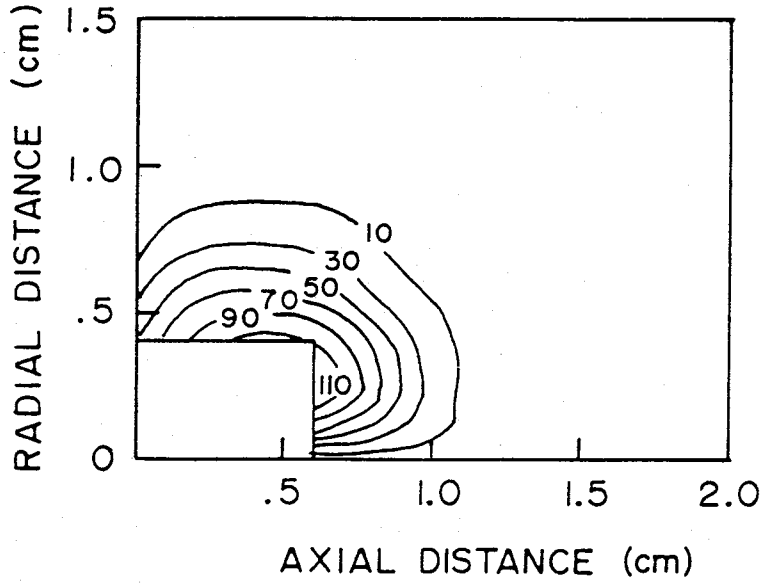

Figure 27b: Experimental Magnetic Field Contours at 40 nsec in 250 mtorr N_2 background.[Ref.1]

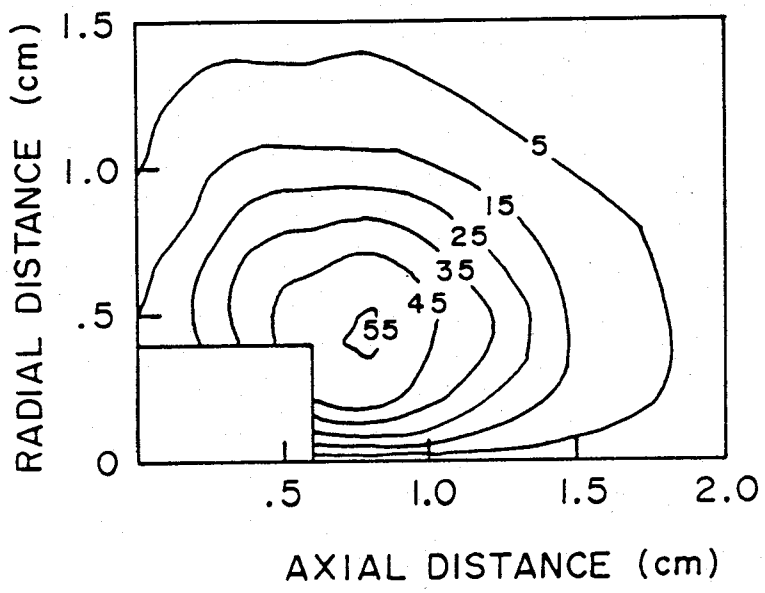

Figure 27c: Experimental Magnetic Field Contours at 120 nsec in 250 mtorr N_2 background.[Ref.1]

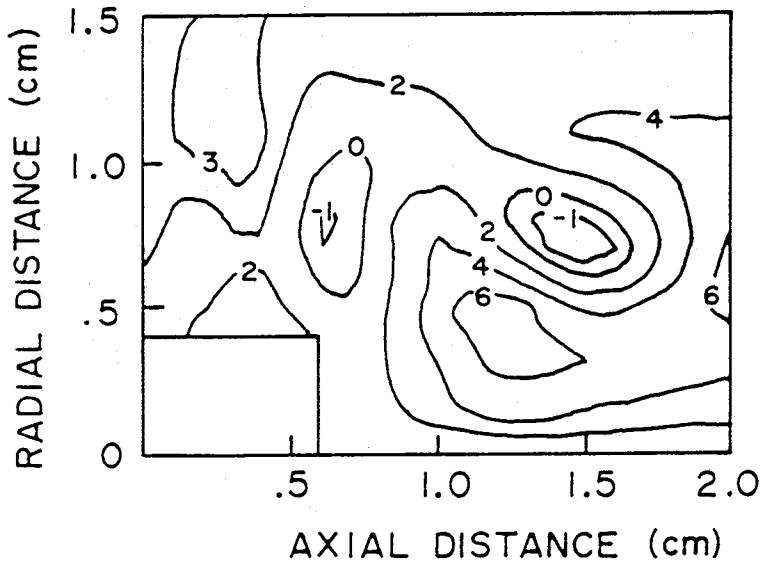

Figure 27d: Experimental Magnetic Field Contours at 300 nsec in 250 mtorr N_2 background.[Ref.1]

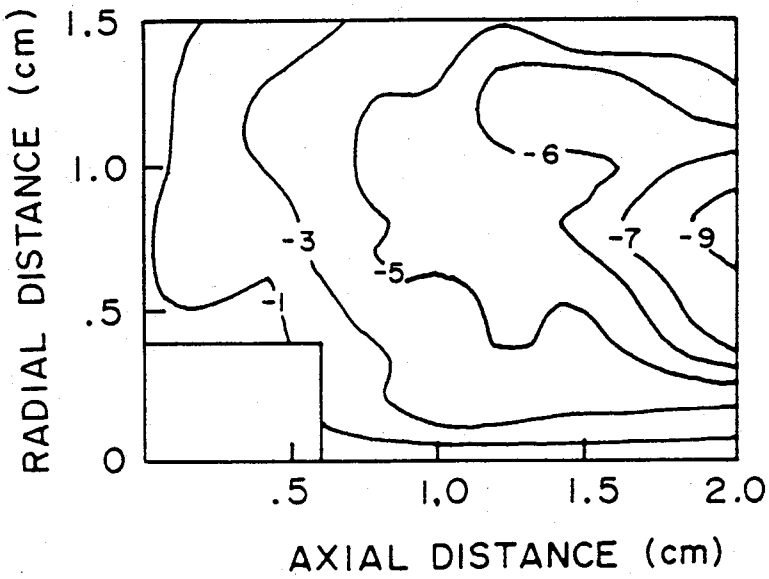

Figure 27e: Experimental Magnetic Field Contours at 700 nsec in 250 mtorr N_2 background.[Ref.1]

Comparing Figures 26 with Figures 27 shows general agreement in field geometry, however, a disparity exists in field strength because of differences in background pressure and the omission of decay mechanisms in the simulations.

F. ELECTRON PRE-HEATING (δ_{zT}/δ_{zn})

Electron pre-heating occurs in front of the shock due to electron heat conduction in the axial direction. As the magnitude of electron pre-heating increases, the ratio δ_{zT}/δ_{zn} of course also increases. This change affects the magnitude of the shock fields generated and the size of the field itself. Figure 28 shows that as the degree of electron pre-heating increases, the generated magnetic field decreases. This figure did not provide any insight into the actual magnitude of δ_{zT}/δ_{zn} due to uncertainties in the efficiency of shock heating. However, if δ_{zT}/δ_{zn} is plotted versus the field size (as in Figure 29) it is evident that because experiment showed axial field width was about 0.5 cm, the ratio δ_{zT}/δ_{zn} must be less than about 1.05. Therefore, δ_{zT}/δ_{zn}=1.013 was used in the simulations. Assuming that the degree of electron pre-heating is small (based on field width estimates) and that δ_{zT}/δ_{zn} is constant, how does the magnitude of the generated field vary with the shock front thickness (δ_{rn})? This is shown in Figure 30. As the shock thickness increases by 50%, the generated field decreases by about 30%. Experiment shows that the shock thickness is about 0.25 cm to 0.3 cm. Therefore, despite the unknown magnitude of plasma heating losses, this analysis still showed that the magnitude of electron pre-heating is small.

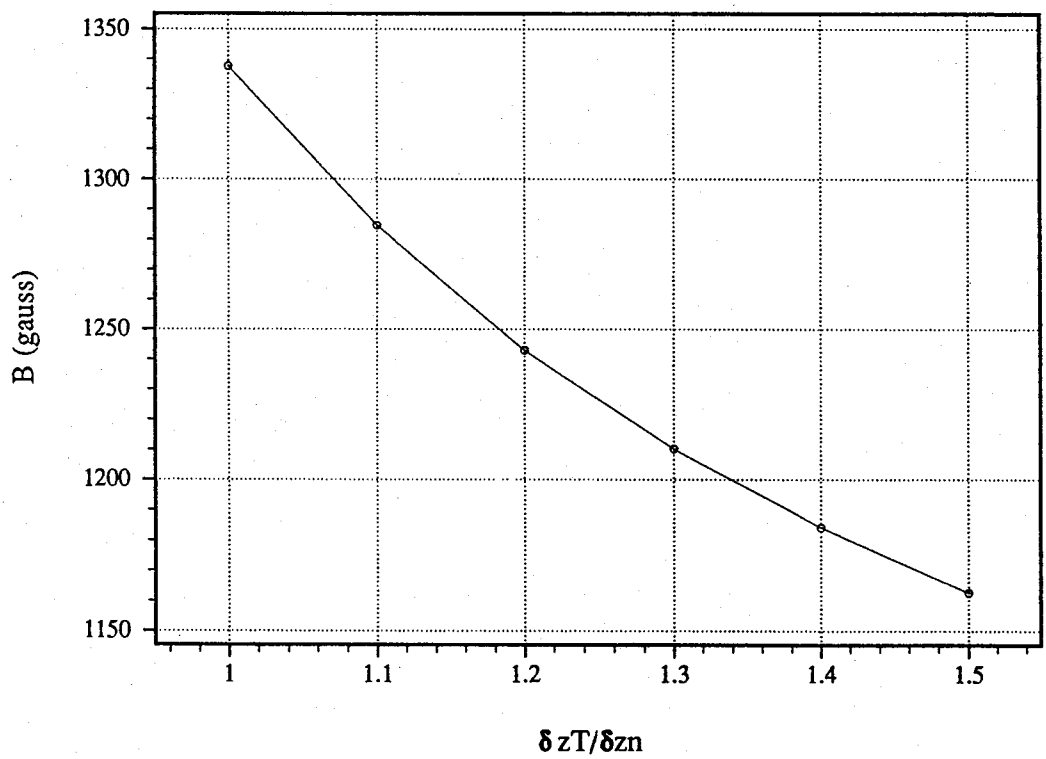

Figure 28: Shock-Generated Magnetic Field versus the Magnitude of Electron Pre-Heating (δ_{zT}/δ_{zn}). For δ_{rT}/δ_{rn}=1.1, T_{max}=43.6 eV, T_{bg}=1.0 eV, n_{max}=15 r.u., n_{bg}=0.1 r.u..

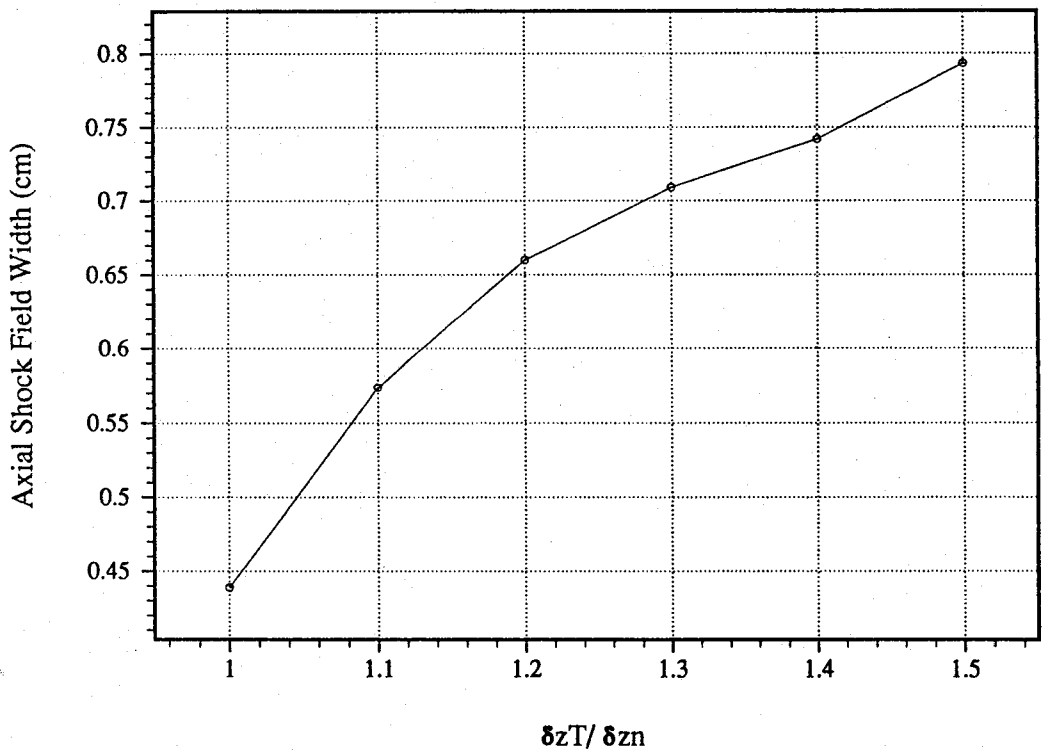

Figure 29: Axial Reversed Field Thickness versus the Magnitude of Electron Pre-Heating (δ_{zT}/δ_{zn}). For δ_{rT}/δ_{rn}=1.1, T_{max}=43.6 eV, T_{bg}=1.0 eV, n_{max}=15 r.u., n_{bg}=0.1 r.u..

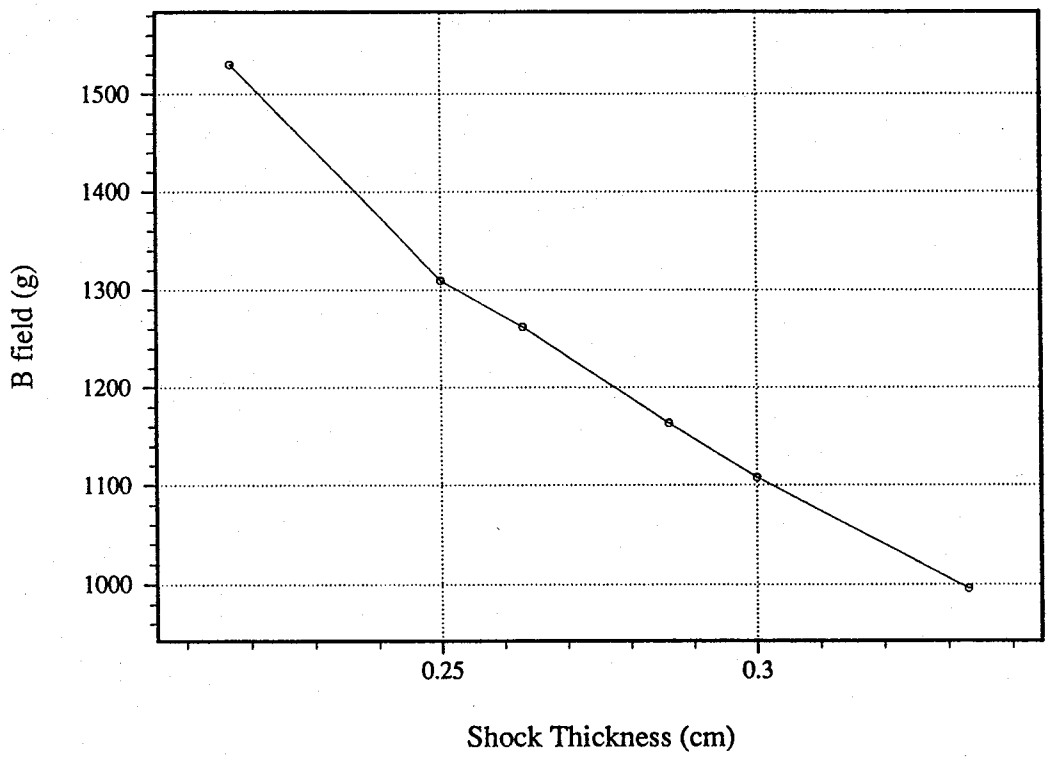

Figure 30: Shock-Generated Field versus Shock Front Thickness (δ_{zn}) for a constant ratio δ_{zT}/δ_{zn}. For δ_{zT}/δ_{zn}=1.01266, δ_{zn}=0.25 cm, δ_{rT}/δ_{rn}=1.1, δ_{rn}=0.5477 cm, $T_{\max}$=43.6 eV, T_{bg}=1.0 eV, $n_{\max}$=15 r.u., n_{bg}=0.1 r.u..

VI. APPLICATIONS

A. INTERPLANETARY SHOCKS

The purpose of this chapter is to provide an example of shock generated magnetic fields which may be observed outside the laboratory. The example chosen in this section is an interplanetary shock. The goal will be to provide an estimate of the steady state magnetic fields present due to shock heating. Because the specific geometry of a given interplanetary shock will vary greatly and collisionless heat conduction mechanisms are involved, many assumptions will have to be made. Detailed analysis of the shock generating mechanism in a collisionless background will not be attempted here; however, this would provide a good starting point for further research and study. The analysis performed here assumes that shock generated fields can be produced in a collisionless environment since the existence of collisionless shocks and more importantly shock heating have been observed. Using equation (10) and neglecting the convective term, the rate of change of the magnetic field will be assumed to be zero. This will be the case when production and decay mechanisms achieve an equilibrium. Therefore, it becomes possible to estimate the steady state magnetic field present if the gradients and conductivity of the plasma are known. First order estimates of these quantities will have to be made.

Large fluctuations in the activity of the sun induce shock conditions in the outward propagating solar wind. These shock waves travel outward with the solar wind at velocities approaching 800-1000 km/sec when they leave the sun's corona. The particles present in the solar wind are mainly protons

and He^{++}. As these shocks approach the earth, satellites measure the discontinuity in the plasma density, temperature, and velocity.

Figure 31 shows data taken by Pioneer 11 in May of 1978 [Ref.13]. This data will be used to estimate the steady state value of the expected shock generated magnetic field. Notice that the temperature shows signs of particle "pre-heating" prior to the arrival of the main shock. This provides pivotal clues for values of the ratios δ_{rT}/δ_{rn} and δ_{zT}/δ_{zn}. It will be assumed that this "slight" temperature increase can be attributed to axial pre-heating, as discussed in the previous chapter. The first objective is to determine the velocity of the shock so that times can be related to distances. The shocked plasma undergoes a velocity increase of about 190 km/sec. Since the plasma density increased by a factor of 3.5, this implies a shock Mach number of 4.5 (assuming γ=1.66). Now the velocity of ion sound in the background is given by:

$$c_1 = \frac{(\gamma + 1)M_1}{2(M_1^2 - 1)} u_p \ ,$$

where u_p is the "blast wind" velocity behind the shock which was determined to be 190 km/sec. Therefore, c_1=59.4 km/sec and hence the shock velocity is 266 km/sec. When referring to Figure 31, one hour represents about 9.576×10^5 km. Various gradient widths can be now be calculated: $\delta_{zT} = 1.2\times10^6$ km, $\delta_{zn} = 5.7\times10^5$ km. This implies δ_{zT}/δ_{zn}=2.09. Since no data exists for the radial behavior, it will also be assumed that δ_{rT}/δ_{rn}=2.09. Letting $\delta_{rn} = 1.0\times10^6$ km, it is now possible to estimate the expected magnetic field. The equation to be solved is:

$$\frac{1}{\mu_o \sigma} \nabla^2 B + \frac{k}{n_p e} \left[\frac{\partial T}{\partial z} \frac{\partial n}{\partial r} - \frac{\partial T}{\partial r} \frac{\partial n}{\partial z} \right] = 0 \ ,$$

where n_p is now the proton density. Substituting the partial derivatives

with approximate expressions involving the characteristic gradient widths gives:

$$\frac{B}{\mu_o \sigma \delta_{rT}^2} + \frac{k}{n_p e}(\delta T_p \ \delta n_p)\left[\frac{1}{\delta_{rT}}\frac{1}{\delta_{zn}} - \frac{1}{\delta_{rn}}\frac{1}{\delta_{zT}}\right] = 0.$$

Let $\delta T_p = 1.6\times10^6$ K and $\delta n_p = 1\ \mathrm{cm}^{-3} = 10^{-6}\ \mathrm{m}^{-3}$; then solve for B yields:

$$B(\sigma) = (\mu_o \sigma \delta_{rT}^2)\left[\frac{k}{n_p e}\right](\delta T_p \ \delta n_p)\left[\frac{1}{\delta_{rT}}\frac{1}{\delta_{zn}} - \frac{1}{\delta_{rn}}\frac{1}{\delta_{zT}}\right] = 4.64\times10^{-2}\ \mathrm{G}\ \Omega\ \mathrm{m}\ \sigma\ ,$$

where $B(\sigma)$ is in Gauss and σ is in mhos-m^{-1}. The effective conductivity of the plasma (σ) is still unknown and is difficult to calculate for the collisionless interplanetary example. Figure 32 shows a plot of the above relationship. The plasma Spitzer conductivity runs from 0 to 1000 mhos-m^{-1}. Therefore, for a relatively conductive background, a steady state magnetic field on the order of several Gauss is expected. If the background is non-conductive, then the magnetic field can be arbitrarily small.

In conclusion, although the specific mechanisms which cause the existing gradients in a collisionless plasma have not been discussed, it is evident that the general phenomenon which occurs in the laboratory case is also applicable in the interplanetary case. Therefore, shock generated magnetic fields in astrophysical phenomena can be measured if the background is sufficiently "conductive".

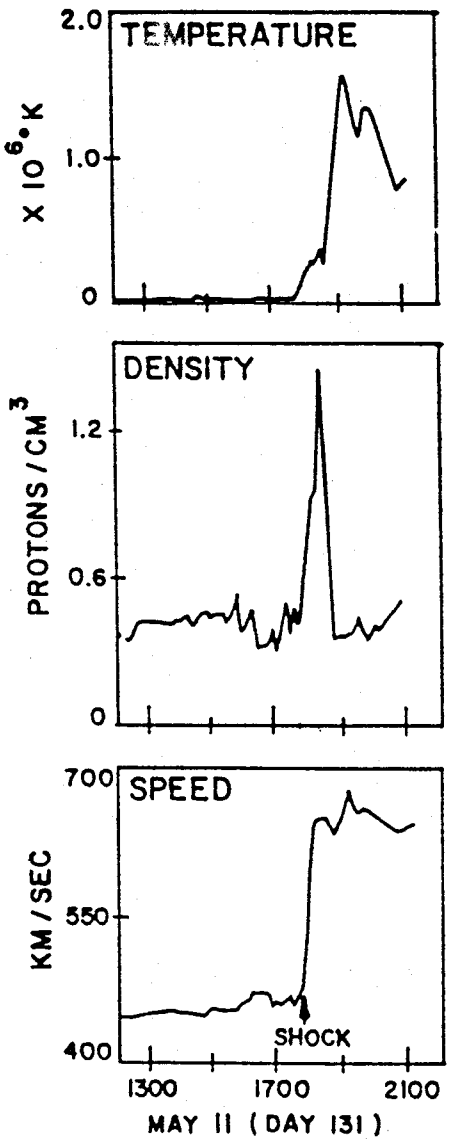

Figure 31: Interplanetary Shock data taken from Pioneer 11 on 11 May 1978 [Ref.12].

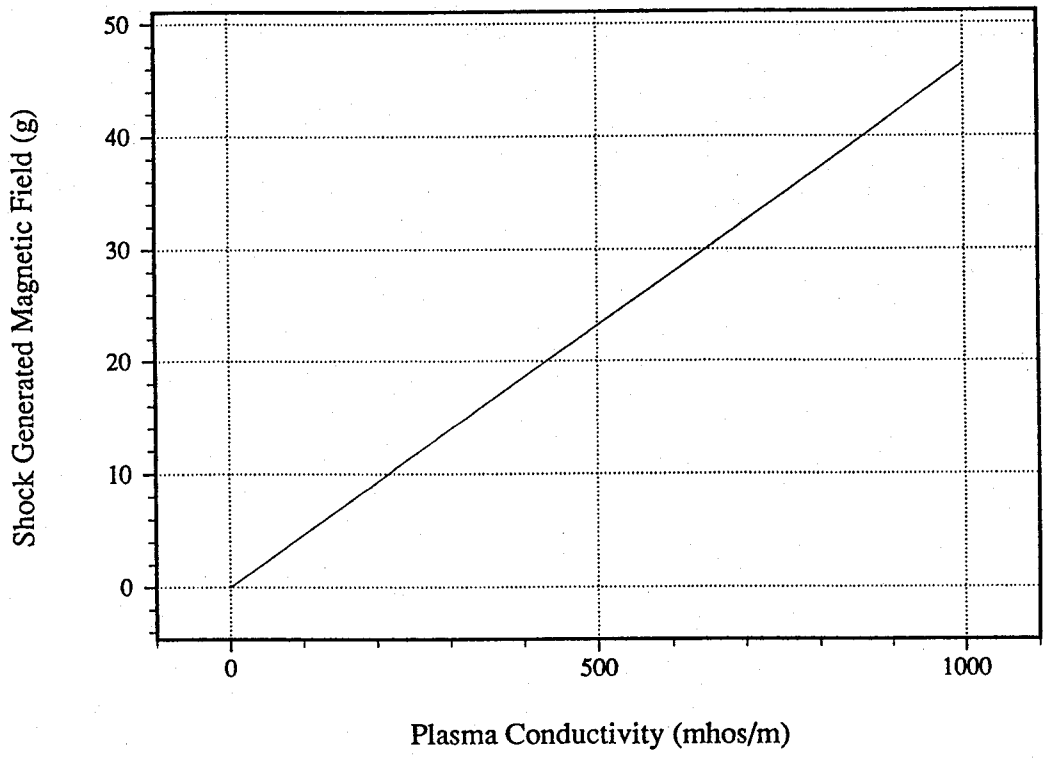

Figure 32: Shock Generated Magnetic Field versus Background Plasma Conductivity for an Interplanetary Shock.

B. NUCLEAR EMP EFFECTS IN THE MHD DOMAIN

High altitude (>100,000 ft) explosions of nuclear weapons produce electromagnetic signals. One such signal is called the electromagnetic pulse (EMP). A typical EMP waveform of a high altitude nuclear burst is shown in Figure 33. Although actual EMP waveforms are classified, Figure 33 provides accurate order of magnitude data. There are basically two regions, the prompt-gamma signal and MHD signal. For times less than 1 second, prompt gamma and neutron scattering produce a large well defined pulse.

After 1 second, late-time EMP is evident which is produced by MHD phenomena. Since the discovery of EMP in the early 1950's during nuclear tests, much theoretical and experimental work has been completed on understanding the prompt-gamma signal. This early signal can cause significant damage to electronic equipment and therefore is of extreme military interest. The late-time MHD (Magnetohydrodynamic) signal, however, has not been so widely studied and is still not fully understood. Although immediate equipment damage by this signal may not occur, certain systems such as long cable or wiring systems (submarine ELF antenna, telephone, etc...) may shutdown due to overload protection devices. Large potentials on the order of several kilovolts per 100 km may result. The focus of this section will be to show that the electromagnetic signature associated with a nuclear EMP in the MHD domain can be explained in terms of shock generated fields! The success of the following analysis is a testament to the fundamental nature of the shock field mechanism and to its great wide ranging application. The late-time generation of an appreciable electric field is the direct focus of this section.

It is assumed that a 250 kiloton nuclear warhead is detonated at an altitude of 100,000 ft (30,500 m). At this altitude only about 60% to 90%, depending on atmospheric conditions, of the yield is transferred to shock energy. The remaining energy is coupled into the initial release of thermal radiation and soft x-rays. As the altitude increases, coupling of the energy yield into shock energy decreases because the atmospheric density decreases with increasing altitude. Within tens of microseconds after detonation, a intense flux of x-rays and gamma rays fully ionizes the surrounding atmosphere out to several kilometers. Based on atmospheric densities at this altitude, the electron particle density is 4.7×10^{23} m^{-3} [Ref.14]. Compton and photocurrents generate the short-time EMP effects mentioned earlier.

The electrons and surrounding ions have sufficient time to achieve thermal equilibrium before the dynamic shock wave arrives. It will be assumed that the surrounding atmosphere is isotropically heated by the initial thermal radiation and that the surrounding temperature is increased by T_c. Therefore, after several milliseconds the atmosphere assumes a temperature of $T_c + T_{amb}$, where T_{amb} is the local ambient temperature. T_{amb} (r,θ) is a function of position. That is, it depends on the height above the earth's surface.

In order to perform calculations, spherical coordinates will be used. The coordinate system is centered about the burst location. r indicates the range from the burst point, θ measures the polar angle from the zenith, and ϕ measures the azimuthal angle around the horizontal plane. It is immediately apparent that the problem indicates azimuthal symmetry and that the electron temperature and density will not be dependent on ϕ. Figure 34 shows the geometry used and the gradients which exist in this problem.

According to reference 14, the shock wave of a 250 KT burst achieves a 1 to 2 mile radius in approximately 5 seconds. It will be assumed that the expanding spherical shock obtains a radius of 1.5 miles (2414 m) in 5 seconds. Therefore, the average shock velocity, v_{sh}, is 1584 ft/s (482.8 m/s). At 5 seconds the shock has a diameter of 3 miles (4828 m). Due to the exponential thinning of the earth's atmosphere as a function of height, the temperature and density at a height of 2414 m above the burst point are different than at a height of 2414 m below the burst point. Accepted values of ambient temperature and density 2414 m above the burst point are; 231 K and 0.0153 Kg/m^3, respectively. At 2414 m below the burst point the ambient temperature and density are; 226 K and 0.0244 Kg/m^3, respectively. It should be noted that the vertical density and temperature gradients are

oppositely oriented and that the density gradient is greater than the temperature gradient. After radiation heating has occurred, the upper and lower temperatures become, (T_c + 231 K) and (T_c + 226 K), respectively. Since sound speed is a function of temperature, the shock Mach number will also be a function of temperature. The Mach number above the burst point (2414 m) will be:

$$M_T = \frac{v_{sh}}{c_{s,T}} \left[\frac{231\ \mathrm{K}}{T_c + 231\ \mathrm{K}} \right]^{1/2} = 1.583 \left[\frac{231\ \mathrm{K}}{T_c + 231\ \mathrm{K}} \right]^{1/2},$$

and the Mach number below the burst point will be:

$$M_B = \frac{v_{sh}}{c_{s,B}} \left[\frac{226\ \mathrm{K}}{T_c + 226\ \mathrm{K}} \right]^{1/2} = 1.601 \left[\frac{226\ \mathrm{K}}{T_c + 226\ \mathrm{K}} \right]^{1/2},$$

where $c_{s,T}$ (=304.9 m/s) and $c_{s,B}$ (=301.6 m/s) are the ambient sound speeds for the temperatures 231 K and 226 K above and below the burst point, respectively. The Mach number below the burst point is larger than the Mach number above the burst point simply because the ambient sound speeds are different. The shock velocity, however, is assumed to be isotropic. The vertical temperature gradient in the atmosphere implies asymmetric shock heating. It should be noted that in order to maintain $M>1$, the maximum increase in temperature produced by radiative heating is about 347 K. This implies that the unshocked background can have a maximum temperature of 578 K. Using equation 20 to now calculate the shock heated temperatures (using $\gamma = c_p/c_v = 1.4$) gives:

$$T_{2,T} = -2.4\times10^{-4}\ \mathrm{K}^{-1}\ T_c^2 + 0.875T_c + 318.1\ \mathrm{K}$$

and

$$T_{2,B} = -2.4\times10^{-4}\ \mathrm{K}^{-1}\ T_c^2 + 0.836T_c + 313.3\ \mathrm{K}$$

where $T_{2,T}$ and $T_{2,B}$ are the shock heated temperatures above and below the

burst point, respectively. See Figure 34. Furthermore, the temperature difference between the two pole locations is:

$$\Delta T = T_{2,T} - T_{2,B} = 4.8\ \mathrm{K} - 0.001T_c\ .$$

The difference between the shocked and unshocked temperature (δT_e) is then:

$$\delta T_e = T_{2,T} - T_{1,T} = -2.4\times10^{-4}\ \mathrm{K}^{-1}\ T_c^2 - 0.165T_c + 87.1\ \mathrm{K}\ ,$$

where $T_{1,T}=T_c + 231$ K. It will be assumed that δT_e is isotropic, although in reality it may vary slightly as a function of altitude.

Similarly, using the relation between the shocked and unshocked density given by equation 18, the shocked density above the burst becomes (assuming the unshocked density ($n_{1,T}$) is $3.6\times10^{23}\ \mathrm{m}^{-3}$ [Ref.14]):

$$n_{2,T} = \frac{5\times10^{26}\ \mathrm{K/m}^{-3}}{2T_c + 693.5\ \mathrm{K}}\ ,$$

where $n_{2,T}$ is in m^{-3} and T_c is in Kelvin. Furthermore, letting the unshocked density below the burst ($n_{1,B}$) be $5.7\times10^{23}\ \mathrm{m}^{-3}$ the shocked density becomes:

$$n_{2,B} = \frac{7.98\times10^{26}\ \mathrm{K/m}^{-3}}{2T_c + 683.6\ \mathrm{K}}\ ,$$

Finally, the vertical density gradient due to atmospheric thinning is:

$$\Delta n = n_{2,T} - n_{2,B} = -5\times10^{26}\ \mathrm{K/m}^{-3}\left[\frac{1.192T_c + 423.2\ \mathrm{K}}{(2T_c + 693.5\ \mathrm{K})(2T_c + 683.6\ \mathrm{K})}\right],$$

and the difference in shocked and unshocked density (δn_e) is:

$$\delta n_e = n_{2,T} - n_{1,T} = \frac{3.6\times10^{23}\ \mathrm{m}^{-3}}{2T_c + 693.5\ \mathrm{K}}(695.4\ \mathrm{K} - 2T_c)\ .$$

One additional term remains to be calculated in order to estimate the magnetic field generated. This is the conductivity of the atmospheric plasma

(σ). Using the Spitzer resistivity, η, gives [Ref.15]:

$$\sigma = \frac{1}{\eta} = \frac{T^{3/2}}{1.03\times10^{-4}\ \Omega\ \mathrm{m}\ \mathrm{eV}^{3/2}\ Z\ \ln\Lambda},$$

where T is in eV, Z is the ionization state, and $\ln\Lambda$ is the coulomb logarithm. Converting eV to Kelvin and letting $Z=1$ and $\ln\Lambda=10$ in the above equation gives:

$$\sigma = 7.77\times10^{-4}\ \mathrm{mhos\ m^{-1}\ eV^{-3/2}}\ T^{3/2},$$

where σ is in mhos/m. In this specific case, $T = T_c + 228$ K, where 228 K is the ambient temperature at the burst height.

The magnetic field is now calculated by a method similar to that used in the previous section. The convection term in the magnetic field generation equation (eq.10) is assumed to be negligible. It is desired to solve for the magnetic field when its time rate of change is zero, i.e. the maximum field. Therefore, using spherical coordinates, the field equation becomes:

$$\frac{\partial\vec{B}}{\partial t} = 0 = \frac{1}{\mu_o\sigma}\nabla^2 B + \frac{k}{en_e}\frac{1}{r}\left[\frac{\partial T}{\partial r}\frac{\partial n}{\partial\theta} - \frac{\partial T}{\partial\theta}\frac{\partial n}{\partial r}\right].$$

It is difficult to work in terms of the coordinate θ at this point in the calculation. Therefore, a change to the altitude variable, h, will be made. The variable, h, represents the vertical height above or below the burst point. The relation between h and θ is:

$$h = r\cos\theta,$$

where r=1.5 miles (2414 m) in this case. Now the partial derivative with respect to θ can be written:

$$\frac{\partial}{\partial\theta} = -r\sin\theta\ \frac{\partial}{\partial h},$$

Inserting this back into the field equation gives:

$$0 = \frac{1}{\mu_o \sigma} \nabla^2 B - \frac{k}{en_e} \sin\theta \left[\frac{\partial T}{\partial r} \frac{\partial n}{\partial h} - \frac{\partial T}{\partial h} \frac{\partial n}{\partial r} \right] .$$

Now approximating the partial derivatives as gradient ratios (as done in the previous section) gives:

$$0 = \frac{1}{\mu_o \sigma} \frac{B}{\delta_B^2} - \frac{k \sin\theta}{en_e} \left[\frac{\delta T_e}{\delta_{rT}} \frac{\Delta n}{\Delta h} - \frac{\Delta T}{\Delta h} \frac{\delta n_e}{\delta_{rn}} \right] ,$$

where δ_B is the characteristic size of the magnetic field ($\delta_B \approx \Delta h/2$), Δh is the characteristic width of the vertical density and temperature gradient of the atmosphere (4828 m), δT_e is the shock-unshocked temperature difference calculated earlier, Δn and ΔT are the vertical density and temperature change experienced in a height change Δh about the burst point after it has been shock heated, and finally δn_e is the change in density across the shock front. Note that the factor of $\sin\theta$ ensures that magnetic flux is only generated where the temperature and density gradients are perpendicular. At θ=0 and $\theta=\pi$, the atmospheric and shock gradients are parallel and hence do not contribute to the field production. However, around the "equator" of the expanding shock, the gradients are perpendicular and result in maximum field generation. The magnetic fields are azimuthal (-$\hat{\phi}$ direction), due to the symmetry in that direction.

Solving for the magnetic field in the above equation and assuming $\theta = \pi/2$ gives:

$$B = \frac{k \mu_o \sigma}{4en_e} \frac{\Delta h}{\delta_{rT}} \left[\left(\frac{\delta_{rT}}{\delta_{rn}} \right) \delta n_e \, \Delta T - \delta T_e \, \Delta n \right] . \tag{34}$$

If T_c=340 K, then all over parameters are: $n_e = 4.8\times10^{23}$ m^{-3}, Δh=4828 m, $\delta_{rT} = 1$ m, $\delta n_e = -4\times10^{21}$ m^{-3}, $\Delta n = -2.2\times10^{23}$ m^{-3}, ΔT=4.5 K, σ=10.5 mhos/m, and δT_e=-3.3 K. This all yields:

$$B = -2.08\times10^{-2} \left[1 - 0.025 \frac{\delta_{rT}}{\delta_{rn}} \right] \text{Gauss} .$$

B is in Gauss. Notice that the behavior of this equation differs significantly from the behavior displayed by any previous analysis of shock generated fields. Shock generated fields are produced even when $\delta_{rT}/\delta_{rn}=1$. This was not the case for laser produced plasma jets. This can be explained by the fact that, in the case of the nuclear burst, the vertical atmospheric gradients are independent of the radial shock gradients generated by the explosion. Non-parallel gradients exist regardless of whether the electron temperature propagates outward faster than the electron density. Although the "bi-diffusive" phenomenon may still operate in this regime, it is not vital to generating the magnetic field.

Figure 34 shows a plot of EMP generated field versus initial background heating by the thermal radiation (T_c). It has already been shown that radiative heating can not exceed about 340 K. This implies that the pre-shock heated atmospheric temperature can not be more than about 570 K. Experimental observation shows that the shock wave does not dissipate until long after 5 seconds have passed. Figure 35 is the graph of equation 34 when all terms and factors involving T_c are used. The full equation is lengthy. Writing it down would not add anything constructive to this analysis. This graph shows that the maximum generated field will be about 0.22 Gauss when T_c=150 K (T_{amb}=380 K). This graph also assumes that the ratio $\delta_{rT}/\delta_{rn}=1$.

The maximum generated field is about 0.22 Gauss. Since this field is time varying and is generated in a period of about 5 seconds, an electric field also exists. Using Maxwell's equation, the electric field may be calculated. The equation of interest is:

$$\nabla\times\vec{E} = -\frac{\partial\vec{B}}{\partial t}.$$

Approximating this equation gives:

$$E \approx \frac{\Delta B}{\Delta t}\delta_E \ ,$$

where δ_E is the characteristic width of the electric field ($\delta_E \approx \delta_B \approx \Delta h/2$). Using ΔB=0.22 Gauss, Δt=5 seconds, and δ_E=2414 m, yields E=10^{-2} V/m. Furthermore, because the magnetic field is in the $-\hat{\phi}$ direction, the cross product implies the electric field is in the $\hat{r}$ and $\hat{\theta}$ directions. These are the proper field directions observed in tests. Comparison of this result to actual field values measured during tests shows that they are in agreement. Although this analysis has been rather "crude" in that many assumptions were made, none of them have been unreasonable. The exact degree of radiative heating is not known; however, simple estimates do indicate that appreciable fields can be generated by the gradients described.

This chapter shows that interplanetary shocks and nuclear EMP effects generate magnetic fields using a similar process. This conclusion is quite remarkable. Further study, and research into additional applications, is warranted. A few additional applications are given in the concluding chapter of this thesis.

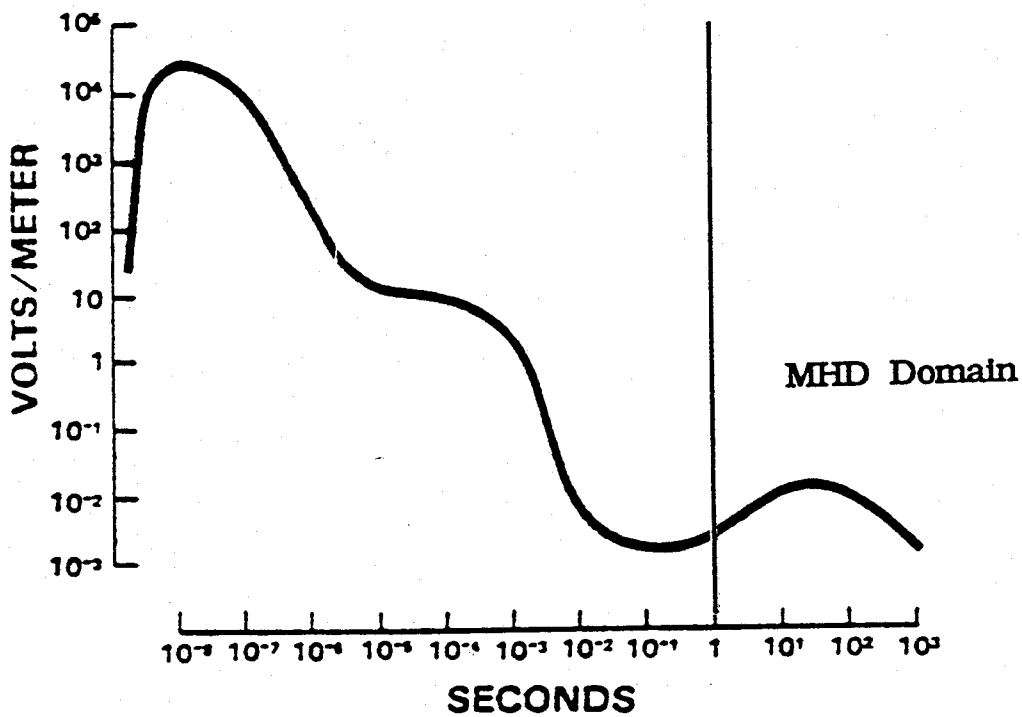

Figure 33: A typical High Altitude EMP Waveform. The Electric Field in V/m versus Time after burst in seconds. Notice scale is log-log. The maximum Electric field in the MHD domain is about 0.01 V/m.

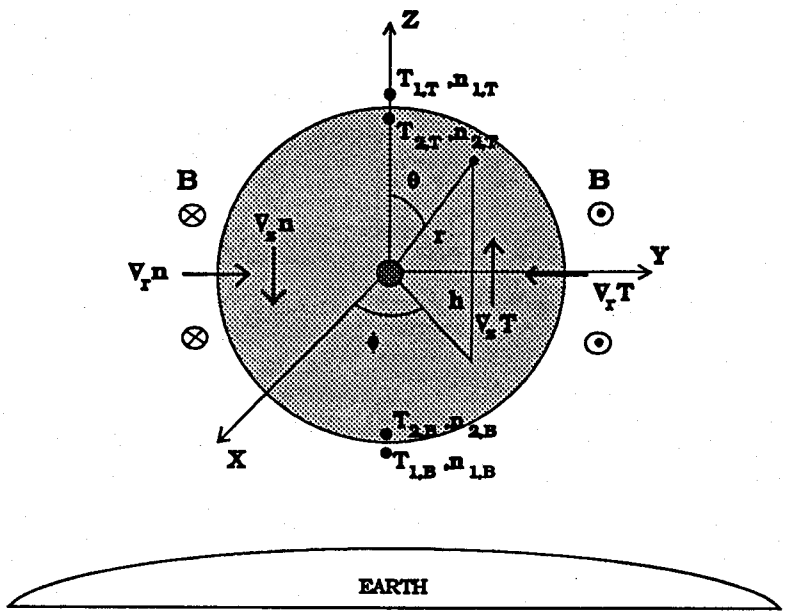

Figure 34: Geometry of a High Altitude EMP Burst. Dominant gradients are depicted in the figure. The shock radius is 1.5 miles (4824 m) at 5 seconds. [Ref.14]

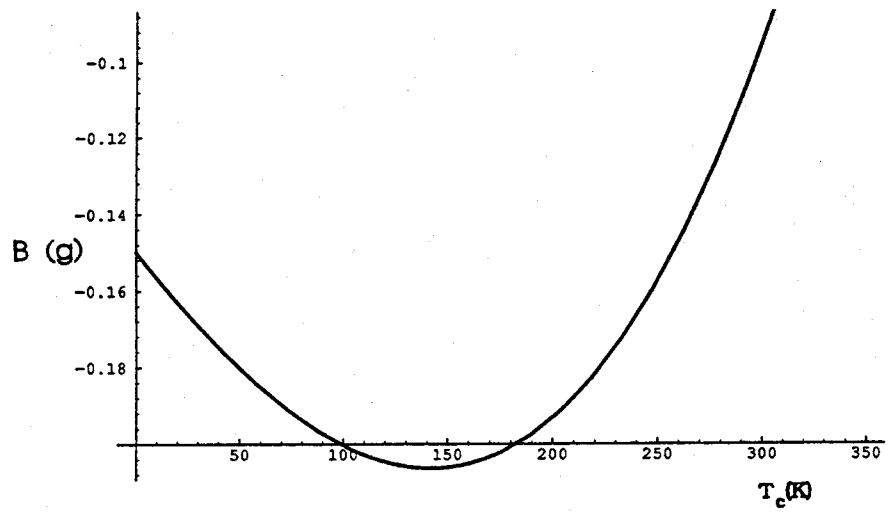

Figure 35: Shock Generated EMP Field as a function of Atmospheric Radiative Pre-heating. ($B(g)$ vs T_c) The magnetic field is an extrema at about T_c=150 K. This implies unshocked atmospheric temperatures are about 380 K.

VII. CONCLUSION

Shock-generated magnetic fields produced by a plasma jet propagating in an ionized background have been simulated using temperature and density profiles derived from experimental data. Simulation results lead to several conclusions. First, shock heating occurs at the jet front at appreciable background pressures (>200 mtorr). The jet has a velocity of about Mach 11.75 in a background pressure of 700 mtorr. At these high Mach numbers, the relative temperature rise across the shock front exceeds the density increase (see Figure 2). Simulations show that the shock mechanism can create magnetic fields at the plasma jet front even at low Mach numbers ($M_1 < 2.4$). In fact, it seems that there are two criteria for creation of shock magnetic fields: (1) Supersonic plasma flow, i.e. ($M_1 > 1.0$), and (2) a difference between radial temperature and density diffusion. Prior to these investigations, electron temperatures were largely unknown. Assuming a background of 1 eV implies maximum electron temperatures are on the order of 43 eV. Simulations confirm that magnetic fields generated by shock heating are azimuthal with respect to the jet. At larger background pressures (> 200 mtorr), field reversal occurs at the jet front when radial electron heat conduction occurs faster than radial ion density diffusion. Density diffusion is dictated by ion motion due to the larger ion mass and the requirement of quasi-neutrality. The directed motion of the ions in the axial direction is much larger than their radial thermal motion. Even though the electrons are magnetized, the electron-electron interactions provide that radial thermal transport occurs more rapidly than ion transport. This bi-diffusivity of the electron density and temperature radial

gradients causes field generation in the reverse direction at the tip of the jet. In addition to radial heat conduction, axial heat conduction also occurs which pre-heats electrons in front of the shock. This pre-heating is shown to be small where $\delta_{zT}/\delta_{zn} \leq 1.05$. Approximating the axial and radial gradients by:

$$\nabla_z T_e \approx \frac{T_e}{\delta_{zT}} \quad , \quad \nabla_z n_e \approx \frac{n_e}{\delta_{zn}} \quad , \quad \nabla_r T_e \approx \frac{T_e}{\delta_{rT}} \quad , \quad \nabla_r n_e \approx \frac{n_e}{\delta_{rn}} \, ,$$

shows how the reverse magnetic field production due to shock heating is accomplished. The requirement to produce shock generated magnetic fields is:

$$\frac{|\nabla_z T_e| \, |\nabla_r n_e|}{|\nabla_r T_e| \, |\nabla_z n_e|} = \frac{(\delta_{zn})(\delta_{rT})}{(\delta_{zT})(\delta_{rn})} > 1 \, .$$

The δs are the gradient scale lengths. Shock heating at the jet front implies:

$$\delta_{zT} \approx \delta_{zn} \qquad \text{and} \qquad \delta_{zT} < \delta_{rT} \, .$$

Therefore electron heat conduction implies:

$$\delta_{rT} > \delta_{rn} \, .$$

Simulations confirm this result. Simulations predict that axial dimension of the shock generated magnetic field is only a function of δ_{zT} and δ_{zn}. That is, if $\delta_{rT} / \delta_{rn} > 1.0$, then as δ_{zT}/δ_{zn} increases the field width also increases. This relationship is shown in Figure 29. Experimentally, axial reversal thickness was about 0.5 cm which corresponds to the condition:

$$\delta_{rT} > \delta_{rn} \quad \text{and} \quad \delta_{zT} \leq 1.05 \, \delta_{zn} \, .$$

Maximum electron temperature and, hence, jet Mach number do not affect the shock field width (reversal thickness). Experimentally, shock heating occurs within 100 nsec after the cessation of the laser pulse. Once shock heating occurs, the growth of the shock generated magnetic field

occurs. For background pressures less than 200 mtorr, shock formation does not occur (or occurs too late) and free expansion of the jet prevails (see Figure 12). The simulation program (pl2.c) neglects the convection and diffusion terms in equation (10), as well as the ionizations, excitations, and dissociations which occur. Therefore, with the exception of the temporal dependence and magnitude of the magnetic field, pl2.c provides good agreement with experiment.

In this instance, numerical simulations (guided by experimental data) provided useful verification and insight into the shock heating mechanism in plasmas. pl2.c also provided an increased basic understanding as to which jet and background parameters were relevant and how each affected the mechanism of shock generated magnetic fields. Applicability of this basic study is wide ranging; some areas might include: (1) explaining late-time electromagnetic pulse (EMP) effects after a nuclear detonation, (2) magnetic field phenomena associated with jets created by Rayleigh-Taylor instabilities (inertial confinement fusion), (3) streaming jets found in astrophysical phenomena, (4) magnetic fields associated with interplanetary shocks formed by the solar winds, (5) the earth's bow shock, (6) the dynamics of comet tail formation and, (7) electromagnetic signature of an orbital re-entry vehicle. Further study in these fields in relation to the shock mechanism seems warranted.

Two specific applications were analyzed in this thesis; interplanetary shocks and late-time nuclear EMP fields. The shock fields generated by the interplanetary shock vary depending on the conductivity of the interplanetary plasma. Although the second application seems completely unrelated to the first, the same field production mechanism fundamentally links both phenomena. Late-time EMP fields are also generated by non-parallel gradients. Calculations show that vertical atmospheric gradients

crossed with the radial shock gradients produce magnetic and electric fields which agree well with those measured during tests. The fact that such widely varying phenomena are described by a single mechanism is a testament to the predictive power and fundamental nature of this physical process.

Magnetic field generation by the dynamo mechanism has been studied extensively in the terrestrial and astrophysical domain; however, a second mechanism is also prevalent in the universe. The shock generation mechanism described in this thesis may help to explain many examples of dynamic magnetic field production in the universe. In particular, those situations where gas or plasma jets stream supersonically, so that shock heating produces non-parallel temperature and density gradients. An example of this has been thoroughly studied in the laboratory. Nature displays extravagant phenomena of this sort as well.

APPENDIX

A. PL2.C

```
/*************************************************
    ====  Self Generated Magnetic Fields  ====
                    PL2.c
*************************************************/
#include  <stdio.h>
#include  <cmath.h>
#include  <greeks.c>

ARRAY2d  B, T, n;

float    t,z,r,z0,a,nmax,dz,dr,b,dt,rl,tmax,c[40],Bgrmx,Bgrmn,
         Bgrx,dtdr,dtdz,dndr,dndz,tl,bmn,bmx,DZt,DZn,Tmx,Tbg,
         aT,an;

int      zck,nc,i,nz,nr,j,Bint,nrl,it;

main() {

/*================== read in parameters ===================*/
printf("\n*** B-field intensities ***\n");
printf("  r, tmax, nc, DZt, DZn, Tmx, Tbg, aT, an\n  ");
scanf("%f%f%d%f%f%f%f%f%f",&rl,&tmax,&nc,&DZt,&DZn,&Tmx,&Tbg,&aT,&an);
tl=0.0062*tmax;dz=tl/250.0;dr=3.0/250.0;dt=0.02;z0=0.0031*tmax;
DZn=1/DZn;DZt=1/DZt;

/*==================== Initialize Arrays ==================*/
for (nz=0;nz<250;++nz) { for (nr=0;nr<250;++nr) {
B[nz][nr]=T[nz][nr]=n[nz][nr]=0.0;}}

/*=================== Time loop ===========================*/
for (t=0.0;t<tmax;t=t+dt) {
zck=(int)((250.0/tl)*((-0.0031*t)+z0));
nmax=0.0012315*t*t*exp(-t/150.0);

/*=========== Initialize T and n arrays for time t ========*/
for (nz=0;nz<250;++nz) {z=(tl/250.0)*(float)nz;
for (nr=0;nr<250;++nr) {
r=(1.5/125.0)*(float)nr-1.5;
if (z>=z0){ T[nz][nr]=Tbg;n[nz][nr]=0.2;}
if (z<z0)
{T[nz][nr]=((Tmx-Tbg)*(1.0-exp(aT*(z-z0)))*exp(-r*r*DZt*DZt))+Tbg;
n[nz][nr]=(nmax*(1.0-exp(an*(z-z0)))*exp(-r*r*DZn*DZn))+0.2;}}}
```

```
/*============== find derivatives wrt z and r ==============*/
for (nz=1;nz<249;++nz) {
if (nz>=zck) {
for (nr=1;nr<249;++nr) {
dtdz=(T[nz+1][nr]-T[nz-1][nr])/(2.0*dz);
dndz=(n[nz+1][nr]-n[nz-1][nr])/(2.0*dz);
dtdr=(T[nz][nr+1]-T[nz][nr-1])/(2.0*dr);
dndr=(n[nz][nr+1]-n[nz][nr-1])/(2.0*dr);

/*================ Calculate updated B-field ================*/
b=1/n[nz][nr];
B[nz][nr]=B[nz][nr]+(b*(dtdz*dndr-dtdr*dndz))*dt;}}}}


/*================= Find Bgr max/min =======================*/
Bgrmx=Bgrmn=0.0;
for (i=1;i<249;++i) { for (j=1;j<249;++j) {
if (Bgrmx<=B[i][j]) Bgrmx=B[i][j];
if (Bgrmn>B[i][j]) Bgrmn=B[i][j];}}
if (Bgrmx>=-Bgrmn) Bgrx=Bgrmx;
if (Bgrmx<-Bgrmn) Bgrx=-Bgrmn;

/*======================== labels ==========================*/
init(); color_scale("bluered"); grey_scale("greyscale1"); window0();
bgcol(7); erase(); color(0); mode("F1");
rect(237,80,841,195); color(2);
rect(230,75,834,190); mode("F0"); color(0); rect(230,75,834,190);
  move(310,80); color(4);
  printf("** Magnetic field Intensity **"); color(0);
  move(280,115); printf("Time=%g nsec",tmax);
  move(280,150); printf("P");sub('a');printf("=700 mtorr");
  move(110,200); printf("1.5"); move(85,325); printf("r(cm)");
  move(95,463); printf("-1.5");
  move(170,720); printf("0"); move(395,720); printf("z(cm)");
  move(635,720); printf("%2.1f",t1); window0();

/*=========== B-z graphics, B-field intensity ===============*/
if (nc!=0) {for (i=0;i<nc;++i) c[i]=Bgrx*(i+0.5)/(float)nc;
for (i=0;i<250;++i) for (j=0;j<250;++j) if (B[i][j]<0.0)
B[i][j]=-B[i][j];}
window(170,200,650,480); intensity(B,250,250); contour(B,250,250,c,nc);
window0(); color(7); move(175,205); printf("Max(%4.2f)",0.1*Bgrx);

/*============ B-z graphics, graph at r=r1 ==================*/
window0();window(170,485,650,715);scale(0,500,1000,-500);color(0);
rect(0,500,1000,-500);boldvec(0,0,1000,0);color(4);
boldcatvec(4*i,Bint);nr1=(int)(125.0*(r1+1.5)/1.5);
for (i=0;i<250;++i) {Bint=(int)((500.0/(1.1*Bgrx))*B[i][nr1]);
printf("%d,%d,\n",4*i,Bint);}
printf(";");window0();color(0);move(85,485);
printf("%4.0f",1.1*0.1*Bgrx);
move(145,590);printf("0");move(70,590);printf("B(g)");
move(75,700);printf("%4.0f",-1.1*0.1*Bgrx);
```

```
/*=================== final ==================================*/
window0(); color(0);
bmn=bmx=0.0; for (i=0;i<250;++i) {if (bmn>=B[i][nr1]) bmn=B[i][nr1];
if (bmx<B[i][nr1]) bmx=B[i][nr1];}
move(675,310); printf("an= %2.2f",an);
move(675,340); printf("aT= %2.2f",aT);
move(675,370); printf("T bg= %g eV",Tbg);
move(675,400); printf("max T");sub('e');printf("= %g eV",Tmx);
move(675,440); greek(Delta);printf("rn= %g cm",1/DZn);
move(675,470); greek(Delta);printf("rT= %g cm",1/DZt);
move(675,500); printf("Bmax= %3.3f gauss",0.1*bmx);
move(675,530); printf("Bmin= %3.3f gauss",0.1*bmn);
move(675,560); printf("r= %g cm",r1);
move(675,590); printf("dt= %g nsec",dt);
move(675,620); printf("Z");sub('o');printf("= %3.3f cm",z0);
mode("F1");
for (i=0;i<55;++i) { color(8+i); rect(680+(int)(4.2*i),200,910,225); }
color(7); if (nc!=0) for (i=0;i<nc;++i)
  { it=680+(int)(230.0*(i+0.5)/(float)nc); vector(it,200,it,225); }
mode("F0"); color(0); rect(680,200,910,225);
move(665,228); printf("-max");
move(790,228); printf("B"); move(870,228); printf("max"); }
```

Computer Simulation Program pl2.c.

B. PL7.C

```
/*************************************************
    ====  Self Generated Magnetic Fields 7 ====
Simulates cross field density and temperature diffusion
assuming fully ionized gas using Bohm diffusion.
                    PL7.c
*************************************************/
#include  <stdio.h>
#include  <cmath.h>
#include  <greeks.c>

ARRAY2d  no, nn, T;

float    t,r,nmax,dz,dr,dt,tmax,ngrmx,ngrmn,
         dn,Bf,A,a1,a2,a3,a4,Drn,Tmx,DrT,r1,r2,pi,pf,Dth,dT
         ,Tgrmx,Tgrmn,Ti,Tf,Tbg,nbg,rTe,rne;

int      i,nz,nr,j,nnt,k,l;

main() {

/*==================== read in parameters ====================*/
printf("\n*** Radial Plasma diffusion ***\n");
printf("  tmax, B, Drn, DrT, Tmx, Tbg, nbg, nmax\n  ");
scanf("%f%f%f%f%f%f%f%f",&tmax,&Bf,&Drn,&DrT,&Tmx,&Tbg,&nbg,&nmax);
dr=5.0/250.0;dt=0.001;
A=6.25e-3/Bf;Drn=1/Drn;DrT=1/DrT;

/*==================== Initialize Arrays ==================*/
for (nr=0;nr<250;++nr) {
r=(2.5/125.0)*(float)nr;
T[5][nr]=T[5][nr]=((Tmx-Tbg)*exp(-r*r*DrT*DrT))+Tbg;
no[5][nr]=nn[5][nr]=((nmax-nbg)*exp(-r*r*Drn*Drn))+nbg;}

/*=========== calc initial number of particles ============*/
pi=pf=0.0;
for (nr=0;nr<250;++nr) {
r=fabs((2.5/125.0)*(float)nr);
pi=pi+(6.28318*r*no[5][nr]*dr);}

/*================ calc initial energy ====================*/
Ti=Tf=0.0;
for (nr=0;nr<250;++nr) {
r=fabs((2.5/125.0)*(float)nr);
Ti=Ti+(6.28318*r*T[5][nr]*dr);}
```

```
/*=================== Time loop ============================*/
nz=5;
k=(int)((0.832/DrT)*(125.0/2.5));
l=(int)((0.832/Drn)*(125.0/2.5));
for (t=0.0;t<tmax;t=t+dt) {

/*========== Calculate updated T and n gradients ==========*/
for (nr=k;nr<248;++nr) {
r=(2.5/125.0)*(float)nr;r1=(2.5/125.0)*(float)(nr+1);
r2=(2.5/125.0)*(float)(nr-1);
a1=T[nz][nr+1]*T[nz][nr+2];
a2=T[nz][nr+1]*T[nz][nr];
a3=T[nz][nr-1]*T[nz][nr];
a4=T[nz][nr-1]*T[nz][nr-2];

/*================== Calculate updated n-field =============*/
dT=(r1*(a1-a2)+r2*(a4-a3))/(4.0*r*dr*dr);
T[nz][nr]=T[nz][nr]+(A*dT*dt);
}

/*============ Calculate updated temperature gradient ======*/
for (nr=1;nr<248;++nr) {
r=(2.5/125.0)*(float)nr;r1=(2.5/125.0)*(float)(nr+1);
r2=(2.5/125.0)*(float)(nr-1);
a1=r1*no[nz][nr+2];
a2=r1*no[nz][nr];
a3=r2*no[nz][nr];
a4=r2*no[nz][nr-2];

/*===== Calculate updated T-field and end time loop ========*/
dn=((a1-a2)+(a4-a3))/(4.0*r*dr*dr);
Dth=4.253e-5*pow(T[nz][nr],2.5)/no[nz][nr];
nn[nz][nr]=nn[nz][nr]+(Dth*dn*dt);
}
for (nr=0;nr<250;++nr) no[nz][nr]=nn[nz][nr];
}

/*======== calc final number of particles ===================*/
for (nr=0;nr<250;++nr) {
r=fabs((2.5/125.0)*(float)nr);
pf=pf+(6.28318*r*no[5][nr]*dr);}

/*========== calc final energy ==============================*/
for (nr=0;nr<250;++nr) {
r=fabs((2.5/125.0)*(float)nr);
Tf=Tf+(6.28318*r*T[5][nr]*dr);}

/*============== Find ngr and Tgr max/min ===================*/
ngrmx=ngrmn=Tgrmx=Tgrmn=0.0;i=5;
for (j=0;j<249;++j) {
if (ngrmx<=no[i][j]) ngrmx=no[i][j];
if (Tgrmx<=T[i][j]) Tgrmx=T[i][j];
if (ngrmn>no[i][j]) ngrmn=no[i][j];
if (Tgrmn>T[i][j]) Tgrmn=T[i][j];}
```

```
/*======================== labels ============================*/
init(); window0();color_scale("bluered");grey_scale("greyscale1");
bgcol(7); erase(); color(0); mode("F1"); rect(237,80,841,195); color(2);
rect(230,75,834,190); mode("F0"); color(0); rect(230,75,834,190);
  move(270,80); color(4); printf("** Radial Cross Field Diffusion **");
  color(0);
  move(250,115); printf("Time=%g nsec",tmax);
  move(250,140); printf("max T");sub('e');printf(" = %g eV",Tmx);
  move(530,115); printf("max n");sub('o');printf(" = %g r.u.",nmax);
  move(85,300); printf("T(eV)");
  move(110,403); printf("0.0");
  move(167,655); printf("0"); move(380,655); printf("r(cm)");
  move(605,655); printf("5.0"); window0();

/*=================== T-r graphics ==========================*/
window0();window(170,200,650,420);scale(0,1000,1000,0);color(0);
rect(0,1000,1000,0);color(4);i=nnt=0;
boldcatvec(4*i,nnt);
for (i=0;i<250;++i) {nnt=(int)((1000.0/(1.1*Tgrmx))*T[5][i]);
printf("%d,%d,\n",4*i,nnt);}
printf(";");
mode("F1");
color(1);vector(4*k,1000,4*k,0);mode("F0");
window0();color(0);move(100,200);
printf("%3.1f",1.1*Tgrmx);

/*=================== n-r graphics ==========================*/
window0();window(170,425,650,645);scale(0,1000,1000,0);color(0);
rect(0,1000,1000,0);color(4);i=nnt=0;
boldcatvec(4*i,nnt);
for (i=0;i<250;++i) {nnt=(int)((1000.0/(1.1*ngrmx))*no[5][i]);
printf("%d,%d,\n",4*i,nnt);}
printf(";");
mode("F1");
color(1);vector(4*l,1000,4*l,0);mode("F0");
window0();color(0);move(100,425);
printf("%3.1f",1.1*ngrmx);
move(108,628);printf("0.0");move(55,520);printf("n(r.u.)");


/*=================== final ==================================*/
window0(); color(0);
move(675,440); printf("T");sub('e');printf("(0) = %2.2f eV",Tgrmx);
move(675,350); printf("nbg = %2.2f r.u.",nbg);
move(675,380); printf("Tbg = %2.2f eV",Tbg);
move(675,410); printf("n(0) = %2.2f r.u.",ngrmx);
move(675,515); greek(Delta);printf("rT");sub('o');
printf(" = %3.2f cm",1/DrT);
move(675,480); greek(Delta);printf("rn");sub('o');
printf(" = %3.2f cm",1/Drn);
```

```
move(675,555); printf("B = %g gauss",Bf);
move(675,585); printf("dt = %g nsec",dt);
move(675,615); greek(Epsilon);sub('n');printf(" = %3.3f",(pf-pi)/pi);
move(675,655); greek(Epsilon);sub('T');printf(" = %3.3f",(Tf-Ti)/Ti);
mode("F1");

/*============== calc Drt/Drn ratio ==========================*/
for (i=0;i<250;++i) if (no[nz][i]<=0.368*(nmax+nbg)) {
rne=(2.5/125.0)*(float)i;i=250;}
for (i=0;i<250;++i) if (T[nz][i]<=0.368*(Tmx+Tbg)) {
rTe=(2.5/125.0)*(float)i;i=250;}
move(675,320); printf("T(4cm) = %2.2f eV",T[nz][247]);
move(675,290); printf("n(4cm) = %2.2f r.u.",no[nz][247]);
move(675,260); greek(Delta);printf("rT/");
greek(Delta);printf("rn = %1.4f",rTe/rne);
}
```

Computer Simulation Program pl7.c.

REFERENCES

1. McKee L.L., *An Investigation of the Self-Generated Magnetic Fields Associated with a Laser-Produced Plasma*, Ph.D. Dissertation, Naval Postgraduate School, 1972.
2. Bird R.S., *The Pressure Dependence of Spontaneous Magnetic Fields in Laser Produced Plasmas*, Ph.D. Dissertation, Naval Postgraduate School, 1973.
3. Allen C.W., *Astrophysical Quantities*, 3rd Edition, pg. 35-48, The Athlone Press, University of London, 1976.
4. Chen F.F., *Introduction to Plasma Physics and Controlled Fusion, Vol.I: Plasma Physics*, 2nd Edition, ch.5, Plenum Press, New York, 1974.
5. Trivelpiece A.W., *Principles of Plasma Physics*, pg.83, McGraw-Hill Book Company, Inc., New York, 1973.
6. Schmidt G., *Physics of High Temperature Plasmas*, 2nd Edition, Academic Press, New York, 1979.
7. Stamper J.A. and others, *Spontaneous Magnetic Fields in Laser-Produced Plasmas*, Phys. Rev. Letters, v.**26**, no.17, pg. 1012-1015, 1971.
8. Dean S.O., McLean E.A., Stamper J.A., and Grien H.R., Phys. Rev. Letters, v.**27**, no.487, 1971.
9. Brooks K.M., *An Investigation of Early Disturbances Found in Association with Laser-Produced Plasmas*, M.S. Thesis, Naval Postgraduate School, 1973.

10. Schwirzke F., Bird R.S., McKee L.L., Cooper A.W., *Pressure Dependence of Self-Generated Magnetic Fields in Laser-Produced Plasmas*, Phys. Rev. A, v.**7**, no. 4, 1973.

11. Schwirzke, F., *Measurements of Spontaneous Magnetic Fields in Laser-Produced Plasmas*, Laser Interactions and Related Plasma Phenomena, Vol.3, Plenum Press, 1974.

12. Birdsall C.K., Longdon A.B., *Plasma Physics via Computer Simulation*, ch.4, Adam Hilger Press, Bristol, 1991.

13. Intrilligator D.S., Miller W.D., Journal of Geophysical Research, v.**87**, pg. 4354, 1982.

14. Glasstone Samuel, Dolan P.J., *The Effects of Nuclear Weapons*, 3rd Edition, ch.3&11, US Government Printing Office, Washington D.C., 1977.

15. Book David L., *NRL Plasma Formulary*, pg.28-32, Naval Research Laboratory, Washington D.C., 1980.

INITIAL DISTRIBUTION LIST

1.	Defense Technical Information Center Cameron Station Alexandria, Virginia 22304-6145	2
2.	Library, Code 52 Naval Postgraduate School Monterey, California 93943-5101	2
3.	Professor Fred Schwirzke, Code PH/SW Department of Physics Naval Postgraduate School Monterey, California 93943-5000	3
4.	Professor William Colson, Code PH/CW Chairman, Department of Physics Naval Postgraduate School Monterey, California 93943-5000	1
5.	Professor A.W. Cooper, Code PH/CR Department of Physics Naval Postgraduate School Monterey, California 93943-5000	1
6.	LT John P. Carter 613 Colonial Manor Road N. Huntingdon, Pennsylvania 15642	3